The Dissertation Committee for Won Jin Cho
certifies that this is the approved version of the following dissertation:

Mitigation of Harmonic and Inter-harmonic Effects in Nonlinear Power Converters

Committee:

_____
Surya Santoso, Supervisor

_____
Aristotle Arapostathis

_____
W. Mack Grady

_____
Edward J. Powers, Jr.

_____
Ronald O. Stearman

Mitigation of Harmonic and Inter-harmonic Effects in Nonlinear Power Converters

by

Won Jin Cho, B.S.; M.S.E.

DISSERTATION

Presented to the Faculty of the Graduate School of

The University of Texas at Austin

in Partial Fulfillment

of the Requirements

for the Degree of

DOCTOR OF PHILOSOPHY

THE UNIVERSITY OF TEXAS AT AUSTIN

December 2010

Dedicated to my parents for their encouragement, support, and love.

Acknowledgments

First of all, I am greatly thankful to my supervisors, Professor Edward J. Powers and Professor Surya Santoso, for their favorable and valuable advice, encouragement, and kindness. Whenever I was struggling against academic difficulties, they led me in step-by-step procedures and gave me absolutely correct solutions. Especially, I would like to give special thanks to Professor Powers for having shown me the best role model of a gentlemen.

Also, I would like to thank to my committee professors, Professor Aristotle Arapostathis, Professor W. Mack Grady and Professor Ronald Stearman for their academic guidance with warm attitudes and smiles.

I am very grateful to my former and present classmates and friends, Byungchul Jang, Hoojin Lee, Hyeonsu Park, Taekhyun Kim, Yongjune Shin, Jin Hur, Kyeon Hur, Seunghoon Choung, Seunghyun Chun, Cheolhee Cho, Seongwan Kim, Heejung Park, Sungwoo Bae, Juyoung Jung, Jihoon Yoon, Duehee Lee, Junseok Song, Joonhyun Kim, Han Kang, Mohit Singh, Alicia J. Allen, Saurabh Kulkarni, Neeraj A Karnik, Swagata Das, Jules Campbell, for cheering me up, sharing my concerns and worries, and giving great helps.

Needless to say, I would like to thank to my parents, Chabong Cho and Okhee Chang, for their love, numerous prayers for me, and unlimited trust.

I greatly appreciate to my fiancée, Dohee Kim, for taking care of me 24/7 with love over a long distance. Also, I am very thankful to my Texas mom, Betty Shaw, for her encouragements in US life and favorable invitations to her house and taking care of my fiancée, Dohee Kim.

Won Jin Cho

The University of Texas at Austin

September 2010

Mitigation of Harmonic and Inter-harmonic Effects in Nonlinear Power Converters

Publication No. _____

Won Jin Cho, Ph.D.
The University of Texas at Austin, 2010

Supervisor: Surya Santoso

Harmonic distortions are inevitably caused by a rectifier and an inverter due to their inherent nonlinearities. An AC-DC-AC converter, configured by the series connection of a rectifier, DC link, and an inverter, induces harmonic distortions at both AC sides and at the DC link. These harmonics can nonlinearly interact or modulate the fundamental frequencies at the AC sides to cause interharmonic distortions. Harmonic and interharmonic distortions can seriously hamper the normal operation of the power system by means of side effects such as excitation of undesirable electrical and/or mechanical resonances, misoperation of control devices, and so forth.

This dissertation presents effective methodologies to mitigate harmonic and interharmonic distortions by applying dithered pulse-width modulated (PWM) signals to a voltage-sourced inverter (VSI) type adjustable speed drive (ASD). The proposed methods are also efficient because the dithering applications are performed on control signals without the need for additional devices. By the help of dithering, the rejection bandwidth of a harmonic filter can be relaxed, which enables a lower-order configuration of harmonic filters.

First, this dissertation provides a dithering application on gating signals of a sinusoidal PWM (SPWM) inverter in the simulated VSI-ASD model. The dithering is implemented by adding intentional noise into the SPWM process to randomize rising and falling edges of each pulse in a PWM waveform. As a result of the randomized edges, the periodicity of each pulse is varied, which result in mitigated harmonic tones. This mitigation of PWM harmonics also reduces associated interharmonic distortions at the source side of the ASD. The spectral densities at harmonic and interharmonic frequencies are quantified by Fourier analysis. It demonstrates approximately up to 10 dB mitigation of harmonic and interharmonic distortions. The nonlinear relationship between the mitigated interharmonics and harmonics is confirmed by cross bicoherence analysis of source- and DC-side current signals.

Second, this dissertation proposes a dithered sigma-delta modulation ($\Sigma\Delta$M) technique as an alternative to the PWM method. The dithering method spreads harmonic tones of the $\Sigma\Delta$M bitstream into the noise level. The noise-shaping property of $\Sigma\Delta$M induces lower noise density near the fundamental frequency. The $\Sigma\Delta$M bitstream is then converted into $\Sigma\Delta$M waveform after zero-order interpolation by which the noise-shaping property repeats at every sampling frequency of the bitstream. The advantages of $\Sigma\Delta$M are assessed by comparing harmonic densities and the number of switching events with those of SPWMs. The dithered $\Sigma\Delta$M waveform bounds harmonic and noise densities below approximately -30 dB with respect to the fundamental spectral density without increasing the number of switching events.

Third, this dissertation provides additional validity of the proposed method via hardware experiments. For harmonic assessment, a commercial three-phase inverter module is supplied by a DC voltage source. Simulated

PWM signals are converted into voltage waveforms to control the inverter. To evaluate interharmonic distortions, the experimental configuration is extended to a VSI-ASD model by connecting a three-phase rectifier to the inverter module via a DC link. The measured voltage and current waveforms are analyzed to demonstrate coincident properties with the simulation results in mitigating harmonics and interharmonics. The experimental results also provide the efficacy of the proposed methods; the dithered SPWM method effectively mitigates the fundamental frequency harmonics and associated interharmonics, and the dithered $\Sigma\Delta$M reduces harmonics with the desired noise-shaping property.

Table of Contents

List of Tables

List of Figures

xvi

Chapter 1

Introduction

This chapter briefly describes harmonic and interharmonic distortions and their effects on power systems. The achieved contributions and the organization of this dissertation are summarized in the latter part of this chapter.

1.1 Harmonic and interharmonic distortions in power converters

According to an IEEE standard [4], power quality disturbances are generally classified into seven categories based on the principal spectral content, duration, and magnitude of the disturbance: transients, short-duration variations, long-duration variations, voltage unbalance, waveform distortion, voltage fluctuations, and power frequency variations. Among these categories, the voltage unbalance and the waveform distortion are steady-state phenomena, while others range within limited durations. These steady-state disturbances last as long as the sources of the disturbances are not removed, negatively affecting all end-users on the same supply system.

A voltage waveform in a conventional power system is expected to be pure sinusoidal with a fundamental frequency and a rated amplitude. When the supply voltage is excited to nonlinear devices or loads, the voltage frequency nonlinearly interacts with them. Mathematically, the nonlinear interaction can be represented as linear combinations of polynomial terms. Each

polynomial term produces a harmonic frequency which has the same order as its exponent. In the case that multiple frequencies are connected via nonlinear devices, these frequencies can modulate each others to result in interharmonic distortions.

1.1.1 Harmonic distortions

Harmonics are defined as sinusoidal voltages or currents whose frequencies are integer multiples of the fundamental frequency [4]. Combined with the fundamental voltage or current, harmonics appear as a distorted waveform. Harmonic distortions originate in the nonlinear properties of devices and loads on the power system. Even if the magnitudes of the harmonic components are approximately 20 % of the fundamental magnitude, harmonic distortion can excite resonance when one of the harmonic components coincides with the natural resonant frequency of the power system.

Harmonic distortions have been reported since the beginning of electric utility service in North America [5]. Due to the concentrated winding coils of synchronous generators, significant fifth and seventh harmonics altered their terminal voltages. These harmonics induced transmission line resonance and caused overheating problems to induction motors. Another harmonic source was also resulted by the generator configuration and arrangement; neutral currents induced by solidly grounded generators which operated in parallel. The neutral currents produced the third order harmonic similar to the zero-sequence third order harmonic caused by wye-connected machines. In 1910s, transformers were reported as other harmonic sources, which interfered with telephone systems. On the process to propose a new waveform standard to reflect telephone interference factor (TIF), the significance of high frequency

harmonics was taken into account by the standard committees. Nowadays, electric power converters are mainly concerned as harmonic sources. In modern industrial applications such as variable speed AC drives and grid connections for renewable energy sources, the use of frequency converters - rectifiers and inverters - are essentially required to match variable frequencies into the desired frequency. Because the rectifiers and the inverters perform switching operations during the process of frequency conversion, harmonics associated with the fundamental frequency are inevitably produced.

1.1.2 Interharmonic distortions

According to an IEC standard 61000-4-7 [6], interharmonic frequencies are defined as any frequencies which are not integer multiples of the fundamental frequency. Interharmonics are generated by two basic mechanisms [7]. The first is nonlinear interaction between two different frequencies. The nonlinear interaction is mainly caused by switching operations of power electronic devices [8] or rapid changes of current in equipment and installation. Due to the nonlinear interaction, the fundamental frequency and its harmonics modulate with the propagated waveforms from the other frequency source. Hence, the interharmonic components locate in the sidebands of the fundamental and harmonic frequencies. The second mechanism is the asynchronous switching in power converters, which indicates that the output frequency of the power converter is not synchronized with the fundamental frequency of the power system. In this case, interharmonic components can be located at anywhere in the spectrum with respect to the power supply voltage harmonics. Practical applications which cause interharmonic distortions are arcing loads, variable-load electric drives, static converters, ripple controls. Regarding interharmonic

3

distortions, a large volume of interharmonic research have been done on various subjects including identification of interharmonic sources, their possible effects, and methodologies of measurements. [8–11].

1.2 Motivation of this research

Harmonics and interharmonics have various effects on power systems. Harmonics can induce problems such as overloading of neutrals, nuisance tripping of circuit breakers, over-stressing of power factor correction capacitors, skin effect, voltage distortion, and zero-crossing noise [12]. Transformer overheating and losses [13] and communication line interference [14] are also side effects of harmonic distortion. In addition, harmonics can cause additional zero crossings of a voltage waveform which confuse control timings of electric circuits [15].

In principle, interharmonics may also cause the same effects on power system as harmonics can do. However, the common effects are less significantly induced by interharmonics because magnitudes of interharmonics are generally smaller than those of harmonics. Interharmonics produce harmful effects because of their frequencies which can exist in each side band of the fundamental and harmonic frequencies. Thus, they can cause their own unique effects including light flicker [16] and sideband torques on the motor/generator shaft [17, 18]. Recent studies have shown that even very small amplitude interharmonics (under 1 % of the fundamental) can have significant adverse effects on important components such as transformers [19] and motors [20]. Interference with control and protection signals in power supply lines is also one of the harmful effects of interharmonics [7].

To prevent harmonic and interharmonic emission to the power grid or

4
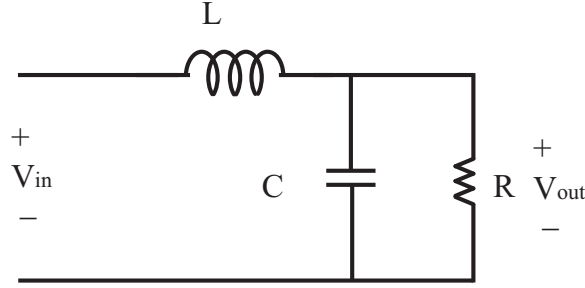
Figure 1.1: L-C harmonic filter configuration
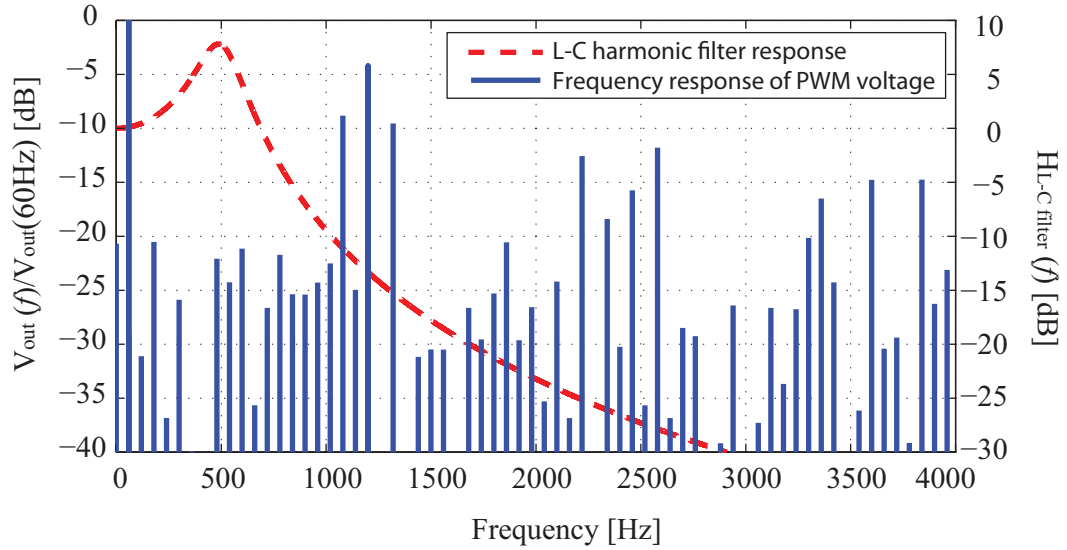
Figure 1.2: Frequency response of PWM voltage and transfer function of L-C harmonic filter

loads, L-C resonance filters, shown in Fig. 1.1, are generally used.

The transfer function of the L-C filter depends on the number of passive elements, L and C, and their values. For the filter to have shaper transition band, more elements of L and C are required. For lower cut-off frequency of the filter, the values of L and C have to be increased, which also increases physical size of the elements. Fig. 1.2 illustrates the transfer function of L-

5

C resonance filter and the frequency response of a pulse width modulated (PWM) voltage. In this example, the fundamental and carrier frequency of the PWM voltage are 60 Hz and 1200 Hz, respectively. The harmonic filter whose cut-off frequency is 510 Hz is designed to mitigate the carrier frequency and its harmonics. Corresponding values of L and C in the harmonic filter are 650 μH and 150 μF, respectively. As shown in Fig. 1.2, a conventional L-C harmonic filter has limitations in mitigating harmonic and interharmonic distortion as follows:

- The cutoff frequency of the filter should be much less than the desired rejection band. In Fig. 1.2, the cut-off frequency of the filter is less than the actual rejection band by 700 Hz.

- Due to the moderate transition band of a harmonic filter, it is difficult to mitigate harmonics and interharmonics located close to the fundamental frequency.

- L-C resonance of a harmonic filter increases harmonic tones around the resonance frequency.

- Nonlinear power converters such as a rectifier and an inverter produce harmonic distortions on both sides of their inputs and outputs. Thus, harmonic filters are required on both sides of the converters.

1.3   Objective of this research

This dissertation aims to provide mitigation methodologies of harmonics and interharmonics associated with a PWM inverter, the commonest topology of power inverters. The principle of mitigation is based on randomly vary-

ing periodicity of harmonic waveforms without alteration of the fundamental period. The randomly varied periodicity results in reduced harmonic tones in the frequency domain. Applying dithering methods to the gating signals, we perform the periodicity randomization of harmonic waveforms without any additional devices such as harmonic filters. The dithering method purposes to mitigate harmonic generation not to prevent harmonic propagation. Thus, it can also mitigate interharmonics associated with the PWM harmonics. Specific objectives in this dissertation are described as follows:

- Evaluating the relationship between the mitigated PWM harmonics and associated interharmonics in a voltage-sourced inverter (VSI) type adjustable speed drive (ASD) system.

- Proposing an alternative PWM topology, dithered sigma-delta modulation ($\Sigma\Delta$M), and evaluating the efficacy in mitigating harmonic distortions.

- Validating the dithered PWM methodologies in mitigating harmonics and interharmonics by performing a hardware experiment.

1.4   Contibutions

The main contributions to this research in mitigating harmonics and interharmonics in power converters are summarized as follows.

- We proposed the dithering method to mitigate both harmonics and interharmonics in a VSI-ASD system. Applying various intensity of the dither to the SPWM process in the simulated VSI-ASD model, we empirically demonstrated the effects of dithering in mitigating both load-

7

side harmonics and source-side interharmonics associated with PWM. Performing cross bicoherence analysis on the mitigated harmonic and interharmonic waveforms, we also confirmed the nonlinear relationship between the mitigated harmonics and interharmonics.

- Based on the approved relationship between load-side harmonics and the source-side interharmonics in the VSI-ASD model, we proposed the dithered $\Sigma\Delta$M as an alternative PWM topology to effectively mitigate the harmonic distortions at the output side of the inverter. By comparing the performance of dithered $\Sigma\Delta$M with those of conventional SPWM, dithered PWM, and carrier frequency randomized SPWM, we demonstrated the efficacy of the dithered $\Sigma\Delta$M in mitigating harmonic distortions. The dithered $\Sigma\Delta$M resulted in less harmonic emissions than conventional SPWM over all frequency ranges, less switching loss and carrier frequency harmonics than the dithered SPWM, and less fundamental frequency harmonics than carrier frequency randomized SPWM. In addition, the dithered $\Sigma\Delta$M demonstrated the advantageous noise-shaping property in that the noise spectral density decreases around the fundamental frequency and the reduced density repeats at every sampling frequency of $\Sigma\Delta$M.

- We validated the effects of dithered SPWM and $\Sigma\Delta$M methods on a VSI-ASD system with hardware experiments. In the experiments, we utilized commercial three-phase inverter module, manufactured by Fairchild Semiconductor, and its application board to configure the input and output interface. We implemented the dithered SPWM, carrier frequency randomized SPWM, and $\Sigma\Delta$M signals using Labview program. The simulated signals were converted into voltage waveforms and exported

8

to the hardware platform. The experimental results demonstrated the same properties of dithered PWMs described in the simulation results. The dithered SPWM effectively reduced fundamental-frequency harmonics and associated interharmonics. The dithered $\Sigma\Delta$M method mitigated both low and high frequency harmonics due to the noise-shaping property. Interharmonics around the fundamental frequency were also decreased by the dithered $\Sigma\Delta$M.

1.5 Organization of the dissertation

The remainder of the dissertation is organized as follows. In Chapter 2, the principles of harmonic and interharmonic frequencies associated with six-pulse rectifier/inverter and PWM inverter are described. These principles on harmonic and interharmonic frequencies are referred in remaining chapters. In Chapter 3, the dithered SPWM method is proposed to mitigate both harmonics and interharmonics of an ASD. The effectiveness of the dithering is empirically evaluated for various intensities of the dither. Nonlinear relationships between the mitigated harmonics and interharmonics are also investigated in cross bicoherence analysis. In Chapter 4, the harmonic-mitigating property of the dithered $\Sigma\Delta$M is represented. The harmonic characteristic of $\Sigma\Delta$M is compared with other randomized SPWM methods. In Chapter 5, the hardware experiments are performed to validate PWM randomization methods described in earlier chapters. Chapter 6 concludes this dissertation. In Appendix A, we demonstrate time-localized harmonics in variable speed wind turbines (VSWTs) using the joint time-frequency distribution as another example of harmonics caused by the AC-DC-AC configuration of power converters.

Chapter 2

Harmonics and interharmonics in AC-DC-AC converters

In this chapter, we describe harmonic and interharmonic principles in a three-phase converter composed of a rectifier, a DC-link, and an inverter. First, the harmonic frequencies for a common rectifier and an inverter are analyzed separately. Then, interharmonic frequencies are derived for the popular types of AC-DC-AC converter, a load commutated inverter (LCI) type and a voltage source inverter (VSI) type. The derived principles are referred as fundamental theories in Chapters 3, 4, 5, and Appendix A.

2.1   Introduction

AC-DC-AC converters illustrated in Fig. 2.1 perform frequency conversions to supply proper frequency of power to the load. The AC fundamental frequency, f_S, is changed into DC frequency through the rectifier and the DC frequency is consecutively converted into desired load frequency, f_L, by the inverter. Since the rectifier and the inverter convert the fundamental frequency by switching operations, they are inevitably produce harmonics associated with the fundamental frequency. The harmonics associated with both fundamental frequencies, f_s and f_L, can reflect from and propagate through those devices as shown in Fig. 2.1. Each harmonic produced by the rectifier and the inverter is also modulated by other harmonic or fundamental frequencies,
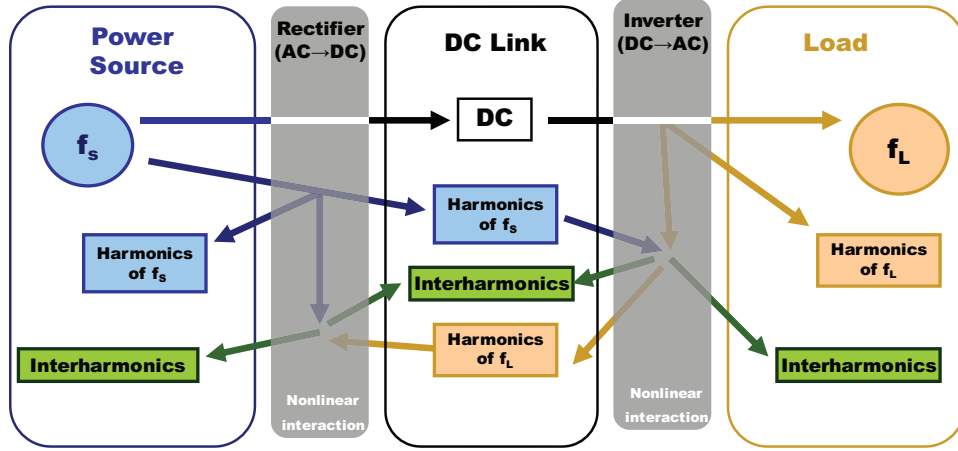
Figure 2.1: Harmonic and interharmonic configuration in AC-DC-AC converter

which eventually cause interharmonic distortion.

Harmonic and interharmonic frequencies are characterized by the configuration of the device. A six-pulse converter is commonly used as a three-phase rectifier and a load commutated inverter (LCI). PWM is the most popular modulation technique for voltage source inverters (VSI). Hence, harmonic and interharmonic components associated with a six-pulse converter and a PWM inverter are analyzed in the following sections.

2.2 Harmonic analysis

2.2.1 Six-pulse converter

A six-pulse rectifier is the most common configuration in three-phase rectifier circuits. The structure of a six-pulse rectifier is same as three-phase H-bridge. The H-bridge is composed of six diodes or six switching devices such as thyristors and silicon-controlled rectifiers (SCRs) to be used as a rectifier. If

the load connected to the rectifier does not affect the DC voltage level, only six diodes can compose the H-bridge. Otherwise, the diodes have to be replaced by switching devices for the rectifier to operate properly. A configuration of a diode-based six-pulse rectifier is illustrated in Fig. 2.2(a). Assuming the rectifier is supplied by an infinite bus and is equipped with a reactor on the DC link, the DC-side voltage has six ripples per period of the AC fundamental frequency as shown in Fig. 2.2(b). The phase current, i_{ar}, is composed of periodic rectangular pulses whose period is same as the fundamental period of the AC power. Applying Fourier analysis, we can represent the line current at the AC side as follows:

$$
\begin{aligned}
i_{ar} &= \frac{2\sqrt{3}}{\pi} I_{dcr} \left(\cos 2\pi f_s t - \frac{1}{5} \cos 2\pi (5f_s)t + \frac{1}{7} \cos 2\pi (7f_s)t - \frac{1}{11} \cos 2\pi (11f_s)t + ... \right) \\
&= \frac{2\sqrt{3}}{\pi} I_{dcr} \left(\cos 2\pi f_s t \pm \sum_{k'=1}^{\infty} \frac{1}{6k' \pm 1} \cos[(6k' \pm 1)(2\pi f_s)t] \right)
\end{aligned}
$$

$$(2.1)$$

where I_{dcr} denotes the DC current and f_s indicates the fundamental frequency at the AC source side. Because we assumed large reactor at the DC side, I_{dcr} can be considered as a constant. However, the DC-side current has same order of harmonics as the DC-side voltage in a practical rectifier. Thus, I_{dcr} can be replaced with $I_{dcr}(t)$ which has every 6th harmonic frequency of the AC-side fundamental frequency as follows [8]:

$$f_{DC,s}^h = 6m \cdot f_s \tag{2.2}$$

where $f_{DC,s}^h$ represents DC-side harmonic frequencies associated with the source-side fundamental frequency and $m = 1,2,3,\cdots$. In the last term of (2.1), $(6k' \pm 1)$ describes the order of harmonics of the phase current. In a practical
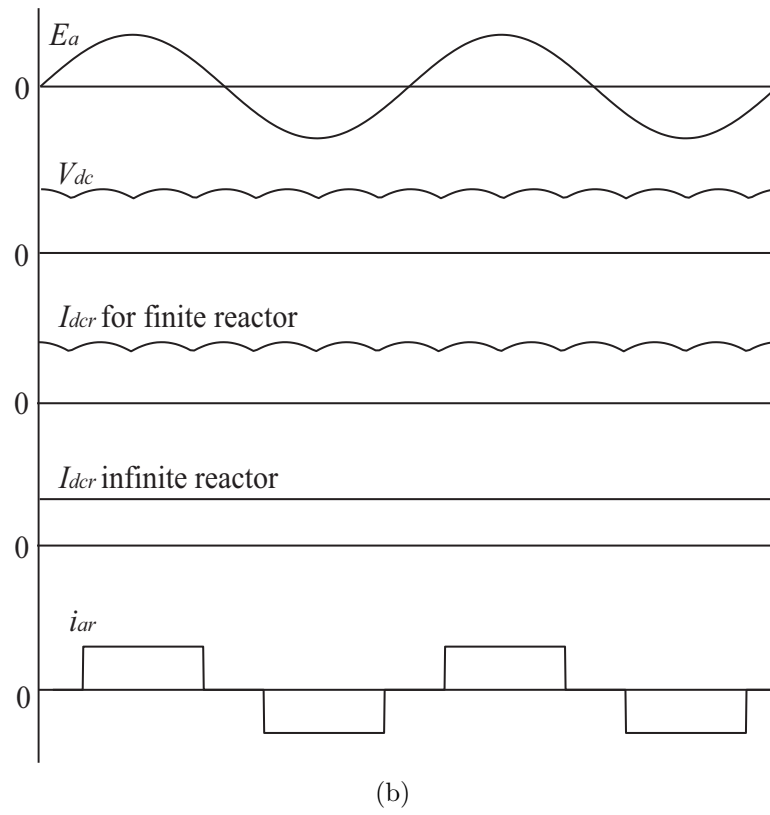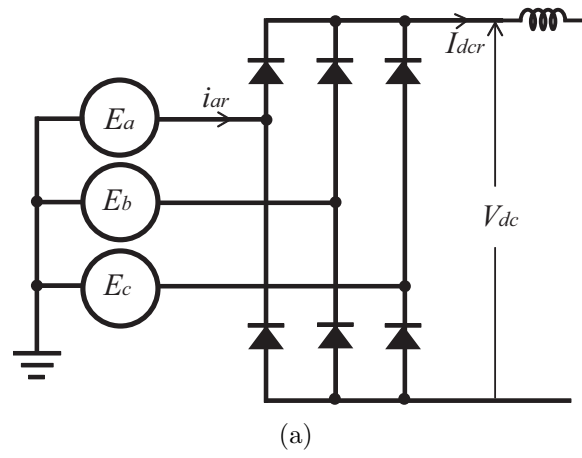
Figure 2.2: Three-phase diode bridge rectifier (a) configuration and (b) voltage and current waveforms

13

rectifier, the harmonic frequency of $(6k' \pm 1)f_s$ is modulated by $I_{dcr}(t)$ whose frequency is described in (2.2). The frequency modulation can be explained by the trigonometric identity in (2.3).

$$\sin \alpha \sin \beta = \frac{1}{2}[\cos(\alpha - \beta) - \cos(\alpha + \beta)] \tag{2.3}$$

Applying (2.3) to (2.1), the harmonic frequency at the source-side can be represented as follows:

$$\begin{aligned} f_s^h &= (6(k' \pm m) \pm 1) \cdot f_s \\ &= (6k \pm 1) \cdot f_s \end{aligned} \tag{2.4}$$

where f_s^h indicates source-side harmonic frequencies and $k = k' + m = 1,2,3,$ $\cdots$.

A six-pulse inverter, shown in Fig. 2.3, is generally used as a high power inverter due to less switching losses than PWM inverters. Operational principle of the six-pulse inverter can be considered as the reverse process of the six-pulse rectifier. For the DC current to be converted into AC current, switching devices have to be used instead of diodes. The switching devices are controlled by the switching function which characterizes output current waveform. Likewise the AC current representation in (2.1), the output phase current, i_{ai} in Fig. 2.3, can be derived in a Fourier series form as follows:

$$i_{ai} = \frac{2\sqrt{3}}{\pi} I_{dci} \left(\cos 2\pi f_l t \pm \sum_{k=0}^{\infty} \frac{1}{6k \pm 1} \cos[(6k \pm 1)(2\pi f_l)t] \right) \tag{2.5}$$

where I_{dci} denotes the line current at the DC side and f_l indicates the fundamental frequency at the inverter output side. For a practical reactor on the DC link, I_{dci} is not constant and can be replaced as a waveform, $I_{dci}(t)$. $I_{dci}(t)$ also has every 6th harmonic frequency which can be represented as follows:

14
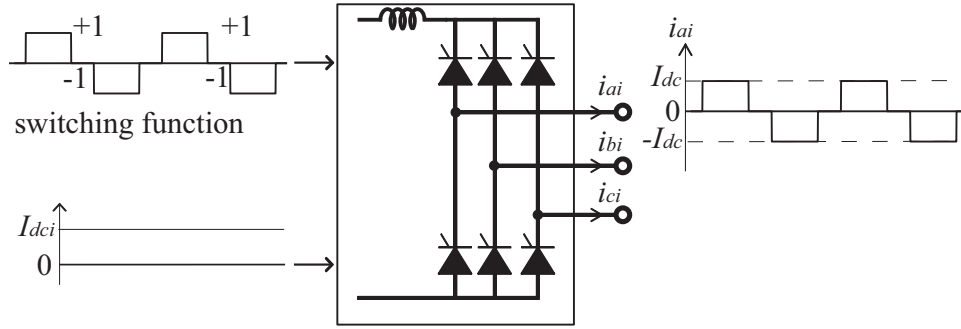
Figure 2.3: Configuration of six-pulse inverter

$$f_{DC,l}^h = (6m) \cdot f_l \tag{2.6}$$

where $f_{DC,l}^h$ denotes DC-side harmonic frequency associated with the load-side fundamental frequency and $m = 1,2,3,\cdots$. Substitute $I_{dci}(t)$ for I_{dci} in (2.5), harmonic frequencies in $I_{dci}(t)$ modulate i_{ai}. Then, the corresponding harmonic frequency of i_{ai} can be derived at the same method applied to (2.4) and expressed as follows:

$$f_l^h = (6k \pm 1) \cdot f_l \tag{2.7}$$

where f_l^h indicates load-side harmonic frequency and $k = 1,2,3,\cdots$.

2.2.2 Pulse width modulated inverter

A PWM inverter is widely used as a voltage source inverter from low to medium-high power applications, which can convert up to few MVA power ratings. General configuration of the PWM inverter is based on the three-phase H-bridge structure where the switching devices are controlled by PWM signals. Among the various PWM techniques, synchronous sinusoidal PWM is the most widely used application due to its simple structure and controllability. Thus, harmonic and interharmonic analyses are conducted for the synchronous

15
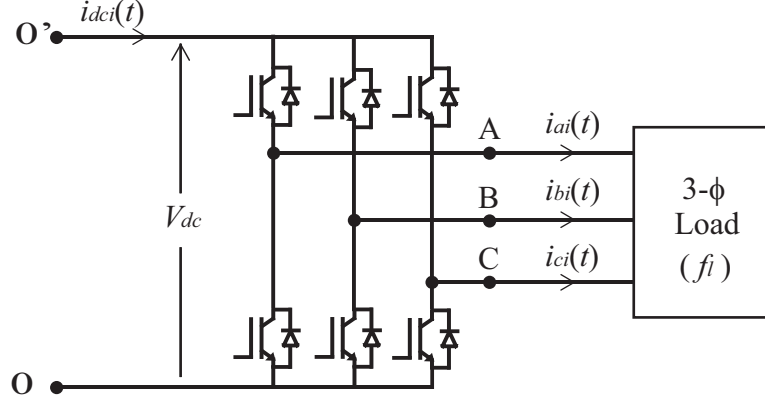
Figure 2.4: Configuration of three-phase H-bridge for SPWM inverter

sinusoidal PMW, where each switching devices is composed of an IGBT-diode pair as shown in Fig. 2.4. The carrier signal, $\Delta(t)$, and the sinusoidal reference signal, $c_A(t)$ are illustrated in Fig. 2.5(a). The PWM phase-voltage, $v_{AO}(t)$, is generated by comparing $c_A(t)$ and $\Delta(t)$, as shown in in Fig. 2.5(b), where nodes 'A' and 'O' are indicated in Fig. 2.4. Similarly, output voltages, $v_{BO}(t)$ and $v_{CO}(t)$, can be obtained by comparing $\Delta(t)$ to reference signals for phase-b and phase-c which are phase-shifted signal of $c_A(t)$ by -120° and +120°, respectively. A general expression for the PWM phase voltage can be expressed as follows:

$$v_{XO}(t) = V^0 + v_{XO}^1(t) + \tilde{v}_{XO}(t) \tag{2.8}$$

where X represents the nodes A, B, and C, expressed in Fig. 2.4. V^0, $v_{XO}^1(t)$, and $\tilde{v}_{XO}(t)$ indicate the DC, the fundamental, and the harmonic components, respectively. The harmonic component, $\tilde{v}_{XO}(t)$ can be expressed as follows:

$$\tilde{v}_{XO}(t) = \sum_{n=2}^{+\infty} A_n \sin(2\pi n f_l t) \tag{2.9}$$

16
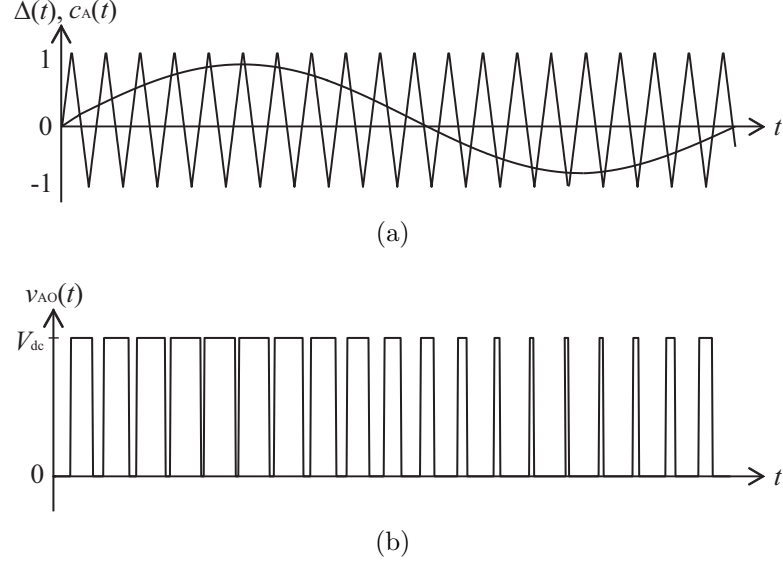
Figure 2.5: SPWM signals: (a) $c_A(t)$ is the sinusoidal reference signal for phase-a and $\Delta(t)$ is the triangular-carrier signal (b) $v_{AO}(t)$ is the output voltage between node A and O in Fig. 2.4.

where A_n and f_l are Fourier coefficient and the fundamental frequency of $\tilde{v}_{XO}(t)$. According to [21], the Fourier coefficient, A_n, can be expressed as follows:

$$
\begin{aligned}
A_n &= \frac{m_a V_{dc}}{2} \sum_{l=1}^{+\infty} \left\{ \left[1 - (-1)^{n + l \cdot (m_f - 1)} \right] \cdot R(n, l, m_f, m_a, \phi_X) \right\} \\
&= \frac{m_a V_{dc}}{2} \sum_{l=1}^{+\infty} \left\{ Q(\cdot) R(n, l, m_f, m_a, \phi_X) \right\}.
\end{aligned}
\tag{2.10}
$$

where

ϕ_X: phase angle of $c_X(t)$ in radian

m_f: modulation index defined by the ratio between the carrier and the fundamental frequencies

17

m_a: modulation ratio defined by the ratio of amplitudes between the reference and the carrier signals

$$Q(\cdot) = 1 - (-1)^{n+l\cdot(m_f-1)}$$

$$R(n, l, m_f, m_a, \phi_X) = \frac{J_{lm_f+n}(l\varepsilon) \cdot e^{jlm_f\phi_X} - J_{lm_f-n}(l\varepsilon) \cdot e^{-jlm_f\phi_X}}{l\varepsilon} \quad (2.11)$$

with $\varepsilon = \frac{m_a\pi}{2}$. $J_a(x)$ indicates a-th order Bessel function of the first kind for an integer a.

Substituting (2.10) and (2.11) into (2.9), $\tilde{v}_{XO}(t)$ can be expanded as follows:

$$
\begin{aligned}
\tilde{v}_{XO}(t) =& \frac{m_a V_{dc}}{2} \sum_{n=2}^{+\infty}\sum_{l=1}^{+\infty}\left\{Q(\cdot)\frac{J_{lm_f+n}(l\varepsilon)}{l\varepsilon}\sin[2\pi n f_l t + (lm_f+n)\phi_X]\right\} \\
& - \frac{m_a V_{dc}}{2}\sum_{n=2}^{\infty}\sum_{l=1}^{+\infty}\left\{Q(\cdot)\frac{J_{lm_f-n}(l\varepsilon)}{l\varepsilon}\sin[2\pi n f_l t + (-lm_f+n)\phi_X]\right\} \\
=& \frac{m_a V_{dc}}{2}\sum_{\substack{n=-\infty,\\ n\neq\{0,\pm1\}}}^{+\infty}\sum_{l=1}^{+\infty}\left\{Q(\cdot)\frac{J_{lm_f+n}(l\varepsilon)}{l\varepsilon}\sin[2\pi n f_l t + (lm_f+n)\phi_X]\right\} \\
=& \frac{V_{dc}}{\pi}\sum_{\substack{n=-\infty,\\ n\neq\{0,\pm1\}}}^{+\infty}\sum_{l=1}^{+\infty}\left\{Q(\cdot)J_{lm_f+n}\left(\frac{lm_a\pi}{2}\right)\frac{1}{l}\sin[2\pi n f_l t + (lm_f+n)\phi_X]\right\}.
\end{aligned}
$$

$$(2.12)$$

In (2.8), $v_{XO}(t)$ can be characterized by m_f. For a synchronous operation in which each pulse in PWM waveform has same phase in each fundamental cycle, m_f must be an integer so that $v_{XO}(t)$ has only DC, fundamental, and harmonic components [21]. If m_f is an odd integer, $v_{XO}(t)$ contains only odd harmonics and V^0 in (2.8) is exactly $V_{dc}/2$. Meanwhile, if m_f is an even integer, both even and odd harmonics can appear in v_{XO}. Moreover, the DC component, V^0, is not exactly $V_{dc}/2$.

18

The feasible set of harmonics associated with the parity of m_f can be verified by investigating (2.12). Recalling $Q(\cdot) = 1 - (-1)^{n+l\cdot(m_f-1)}$, $Q(\cdot)$ can be either 0 or 2. If m_f is an odd integer, $Q(\cdot)$ can be expressed as follows:

$$Q(\cdot) = 1 - (-1)^{n+l(m_f-1)} = 1 - (-1)^n \tag{2.13}$$

where the value of $Q(\cdot)$ is only dependent on n. Representing an odd integer n as $(-l \cdot m_f + k)$, $\tilde{v}_{XO}(t)$ in (2.12) can be rewritten as follows:

$$\tilde{v}_{XO}(t) = \frac{2V_{dc}}{\pi} \sum_{l=1}^{+\infty} \frac{1}{l} \sum_{k=-\infty}^{+\infty} \left\{ J_k \left(\frac{lm_a\pi}{2} \right) \sin\left[2\pi(-lm_f+k)f_l t + k\phi_X \right] \right\} \tag{2.14}$$

where $l+k$ is odd.

Meanwhile, if m_f is even, $Q(\cdot)$ dependents on both n and l. Thus, there exist feasible sets of (n, l) which enable $Q(\cdot)$ to be 2. Representing n as $(l' \cdot m_f + k)$ where l' and k are integers, l' and k can be assumed as all integer values.

For even and odd integers of m_f, the harmonic frequencies at the load side of a PWM inverter can be represented as follows:

$$f_l^h = |l \cdot m_f \pm k| f_l \tag{2.15}$$

where f_l^h and f_l denote harmonic and fundamental frequencies at the output of a PWM inverter, respectively. Feasible parameters l and k with respect to m_f are summarized in Table 2.1.

Table 2.1: Parameters l and k for even and odd m_f

Odd m_f		Even m_f	
l	k	l	k
even	odd	integers	integers
odd	even	integers	integers

2.3   Interharmonic analysis

2.3.1   LCI-type AC-DC-AC converter

Line-comutated inverter (LCI) drives are mainly used in high power applications. In LCI-type AC-DC-AC converters, a switch-controlled six-pulse rectifier and an inverter are connected to the DC-link through a large inductor as shown in Fig. 2.6. If the inductor on DC link is infinitely large, the current following through the DC link is constant. However, in practical LCI-type AC-DC-AC converter, the six-pulse rectifier and inverter can cause every 6th-order harmonic current associated with the fundamental frequencies f_s and f_l on the DC link. Furthermore, the harmonic currents from source and the load sides can be modulated by each other due to the switching operation of 6-pulse converters. Thus, interharmonic frequencies which appear on DC link can be expressed as linear combinations of (2.2) and (2.6) as follows:

$$f_{dc}^{ih} = |6mf_s \pm 6nf_l| \tag{2.16}$$

with m=1,2,$\cdots$, and n=1,2,$\cdots$.

Harmonic currents at the DC link can also affect the source- and load-side current in the form of interharmonics; harmonics associated with f_s can cause interharmonics at the load-side and f_l at the source-side. Recalling Fig. 2.3 and (2.16), the switching function and the DC-side current can be
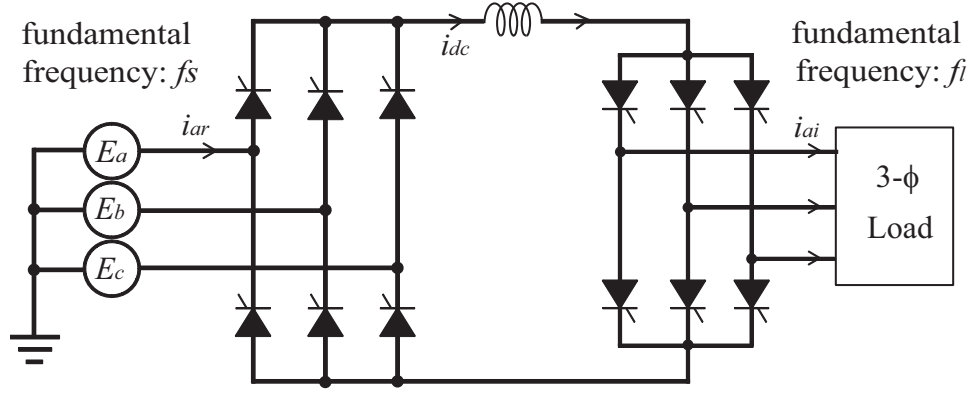
Figure 2.6: Configuration of LCI-type AC-DC-AC converter

expressed as follows:

$$S(t) = \left|\overline{S}^0\right| \cdot \cos(2\pi f_{ac}t) + \sum_{k=1}^{+\infty} \left|\overline{S}^k\right| \cdot \cos\left[2\pi(6k \pm 1)f_{ac}t\right] \qquad (2.17)$$

$$i_{dc}(t) = I_{DC} + \sum_{h=1}^{+\infty} \left|\overline{I}_{dc}^h\right| \cos(2\pi h f_{dc}t) \qquad (2.18)$$

where $|\overline{S}^k|$ and $|\overline{I}_{dc}^h|$ denote the amplitudes corresponding the sinusoidal terms in the summations. Corresponding AC current, $i_{ac}(t)$, at either the source or the load side can be derived as follows:

$$\begin{aligned}
i_{ac}(t) = {} & \left|\overline{S}^0\right| I_{DC} \cdot \cos(2\pi f_{ac}t) + \sum_{k=1}^{+\infty} \left|\overline{S}^k\right| I_{DC} \cdot \cos[2\pi(6k \pm 1)f_{ac}t] \\
& + \frac{1}{2}\sum_{h=1}^{+\infty} \left|\overline{S}^0\right| \left|\overline{I}_{dc}^h\right| \cdot \cos[2\pi(f_{ac} + h f_{dc})t] \\
& + \frac{1}{2}\sum_{k=1}^{+\infty}\sum_{h=1}^{+\infty} \left|\overline{S}^k\right| \left|\overline{I}_{dc}^h\right| \cdot \cos(2\pi[(6k \pm 1)f_{ac} \pm h f_{dc}]t)
\end{aligned} \qquad (2.19)$$

21

where f_{ac} corresponds to the frequency either at the source or the load side and f_{dc} indicates harmonic frequency at the DC link.

From (2.19), feasible interharmonic frequencies at either the source or load side can be derived. For $(f_{ac}, f_{dc})=(f_s, f_l)$, the interharmonic frequency at the source side is represented as follows:

$$f_s^{ih} = |(6m \pm 1)f_s \pm 6nf_l| \tag{2.20}$$

where $m=0,1,\cdots$, and $n=1,2,\cdots$. For $(f_{ac}, f_{dc})=(f_l, f_s)$, the interharmonic frequency at the load side can also expressed as follows:

$$f_l^{ih} = |6mf_s \pm (6n \pm 1)f_l| \tag{2.21}$$

where $m=1,2,\cdots$, and $n=0,1,\cdots$.

Feasible interharmonic frequencies at the load and source side, described in (2.20) and (2.21), are illustrated in Fig. 2.7(a) and (b). In both figures, the interharmonic frequencies are plotted with respect to variable load frequency, f_l, from 0 Hz to 60 Hz. The source frequency, f_s is fixed at 60 Hz. Feasible interharmonic frequencies are plotted in solid line in both figures.

2.3.2　VSI-type AC-DC-AC converter

From low and medium-high power application, VSI configuration is widely used for a AC-DC-AC converter in which a six-pulse diode rectifier and a three-phase PWM inverter are connected to the DC-link through a large capacitor as shown in Fig. 2.8. Likewise LCI-type converters, harmonics generated by the rectifier and inverter can produce interharmonics at the supply system, the DC-link, and the load in VSI-type converters.
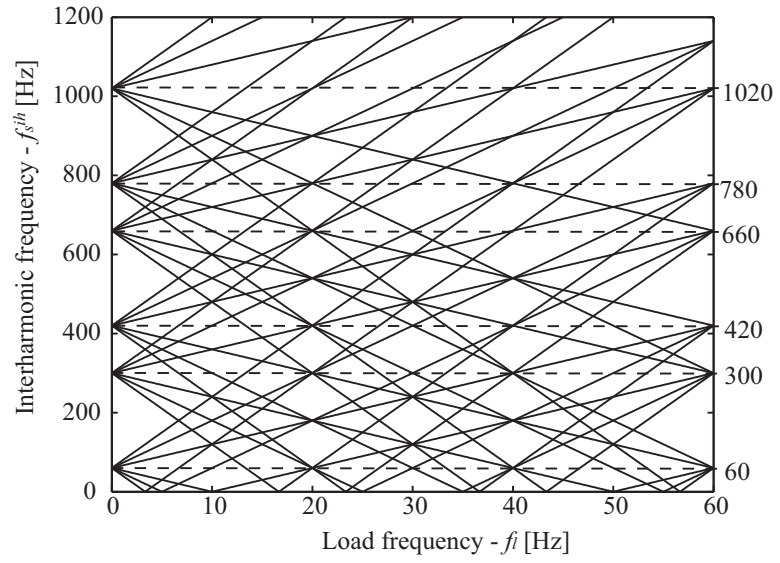
(a)
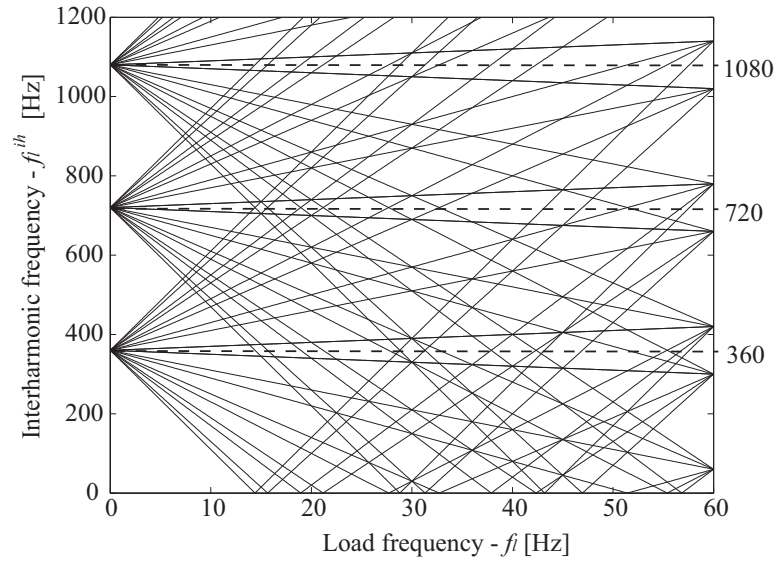
(b)

Figure 2.7: Interharmonic frequency at (a) the source and (b) the load side in LCI-type AC-DC-AC converter

23
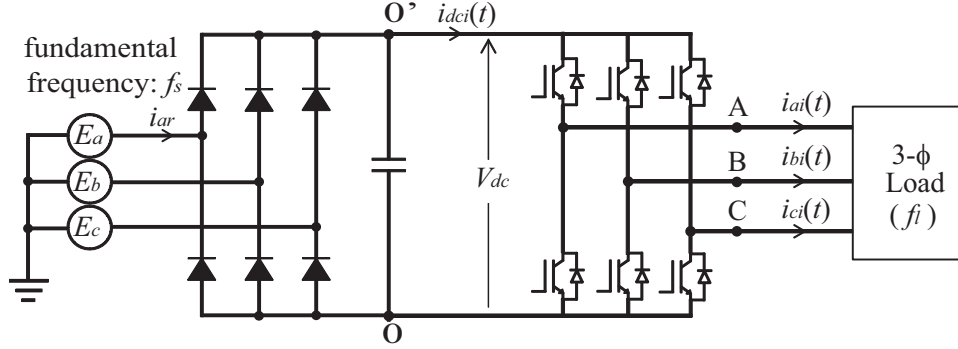
Figure 2.8: Configuration of VSI-type AC-DC-AC converter

Harmonics generated by the six-pulse rectifier in VSI-type converter have the same set of frequencies as those in LCI-type converters. However, harmonics from the PWM inverter show more complex characteristics as shown in Section 2.2.2, which differently produce interharmonic frequencies from LCI-type converters. To evaluate harmonic frequency caused by the PWM inverter on the DC-link, we assume that (i) the inverter does not dissipate nor generate power and (ii) the the three-phase load is balanced and composed of only passive components. Then, the current, $i_{dci}(t)$, indicated in Fig. 2.8, can be represented as follows:

$$i_{dci}(t) = \frac{v_{AO}(t)}{V_{dc}} \cdot i_{ai}(t) + \frac{v_{BO}(t)}{V_{dc}} \cdot i_{bi}(t) + \frac{v_{CO}(t)}{V_{dc}} \cdot i_{ci}(t) \qquad (2.22)$$

where v_{AO}, v_{BO}, and v_{CO} are explained in (2.8) and i_{ai}, i_{bi}, and i_{ci} are indicated in Fig. 2.8. $v_{XO}(t)$, where $X{=}A$, B, or C, indicates a PWM voltage waveform which swings between 0 and V_{dc}. Recalling (2.15), harmonic frequency in $v_{XO}(t)$ can be expressed as a form of $|lm_f{\pm}k|$ with corresponding integers l and k. Because a balanced passive load is assumed above, harmonic components of i_{xi}, where $x{=}a$, b, or c, have the same frequency as those of v_{XO}. By the same

24

Table 2.2: Parameters l and r for different m_f

m_f	Odd		Even	
	l	r	l	r
non- triple	even	even	even	integers
	odd	odd	odd	integers
	l	r	l	r
triple	even	even triple	even	triple integers
	odd	odd triple	odd	triple integers

principle shown in (2.19), the harmonic frequencies of $i_{dci}(t)$ can be deduced by the modulation between i_{xi} and v_{XO} and represented as follows:

$$f^h_{dc,l} = |lm_f \pm (k \pm 1)| \cdot f_l = |lm_f \pm r| \cdot f_l \qquad (2.23)$$

where $f^h_{dc,l}$ is harmonic frequency in $i_{dci}(t)$ associated with PWM operation, l, k are corresponding integers described in Table 2.1, and $r = k \pm 1$. According to [21], for the triple integer of m_f, only triple harmonics associated with PWM inverter are present on the DC link. Thus, feasible combinations of l and r with respect to m_f can be summarized as shown in Table 2.2. The PWM-associated harmonics on the DC-link are coupled with the source-side harmonics, which produce interharmonics at the source side. On the DC-link, harmonic currents described in (2.1) are also present due to the six-pulse rectifier as well. The six-pulse related harmonics are modulated with the harmonics at the output of inverter PWM, which causes load-side interharmonics. Feasible interharmonic frequencies at the source- and the load-side can be evaluate by the same method described in (2.19). Replacing the last term, '$6n \cdot f_l$', in (2.20) with (2.23), the interharmonic frequency at the source side is described as follows:

$$f_s^{ih} = |(6m \pm 1) \cdot f_s \pm (lm_f \pm r) \cdot f_l| \qquad (2.24)$$

where m=0, 1, $\cdots$, l and r as in Table 2.2.

Substituting (2.21) for $(6n\pm1)\cdot f_l$ in (2.15), the interharmonic frequency at the load side can be represented as follows:

$$f_l^{ih} = |6m \cdot f_s \pm (lm_f \pm k) \cdot f_l| \qquad (2.25)$$

where m=1, 2, $\cdots$, l and k as in Table 2.1. Interharmonic frequencies, (2.24) and (2.25), are illustrated in Fig. 2.9(a) and (b) with respect to the load frequency. The source and the carrier frequencies are fixed at 60 Hz and 1200 Hz, respectively. The horizontal axis indicates load frequency, f_l, of the PWM inverter, and the vertical axis denotes feasible interharmonic frequency associated with f_l and the source-side fundamental frequency, 60 Hz. The output frequency varies within the values which enable m_f to be integer, where corresponding (m_f, f_l) are (1200,1), (600,2), (400,3), (300,4), (240,5), (200,6),(150,8), (120,10), (100,12), (80,15), (60,20), (48,25), (40,30), (30,40), (25,48), (24,50), (20,60). In each figure, feasible interharmonic frequencies are plotted in dots.

2.4   Summary

This chapter has described the feasible harmonic and interharmonic frequencies caused by a three-phase rectifier and an inverter. In Section 2.2, feasible harmonic frequencies produced by a six-pulse rectifier/inverter and a PWM inverter were mathematically derived. Based on the derived feasible harmonic frequencies, feasible interharmonic frequencies in LCI- and VSI-type

AC-DC-AC converters were described in Section 2.3, which are caused by the frequency coupling between two different fundamental frequencies and those harmonics. Based on the feasible harmonic and interharmonic frequencies described in this chapter, voltage and current spectra in the simulation and experimental results are evaluated in remaining chapters.
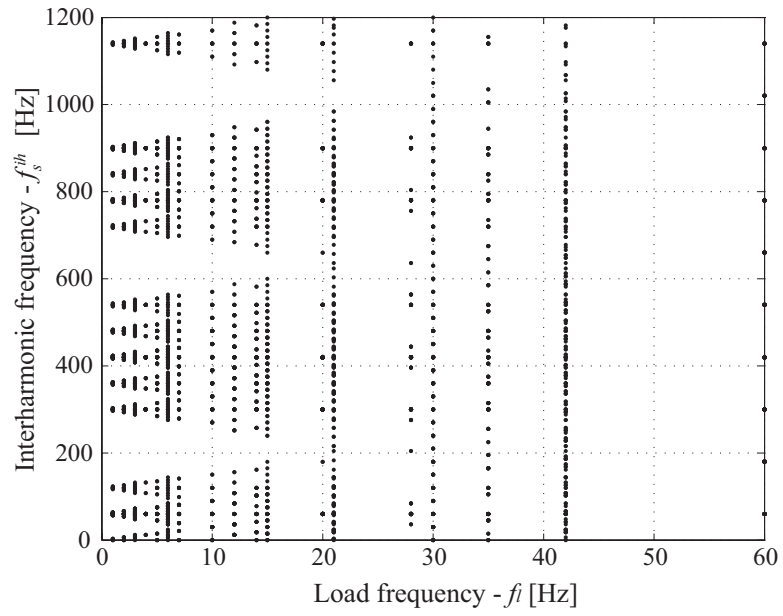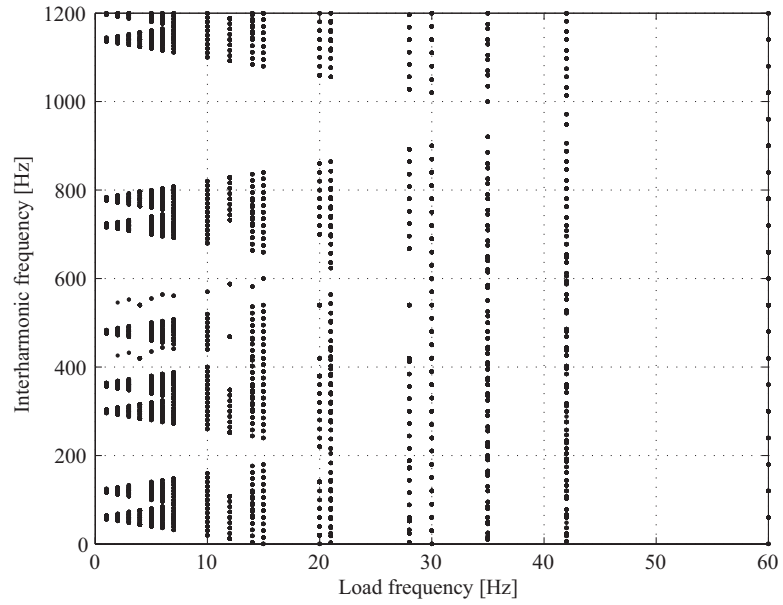
Figure 2.9: Interharmonic frequency at (a) the source and (b) the load side in VSI-type AC-DC-AC converter

Chapter 3

Mitigation of harmonic and interharmonic distortions in a PWM-type ASD system using dithering method

This chapter presents the effect of dithering on both harmonics and interharmonics in a voltage-sourced inverter (VSI) type adjustable speed drives (ASDs). The VSI-ASD model simulated using PSCAD/EMTDC program is composed of a six-pulse rectifier and a sinusoidal pulse width modulated (SPWM) inverter. The PWM signal for the inverter is modified by means of the additive noise, dither. The dither randomizes the timing of rising and falling edges of PWM signals, which eventually reduces periodic harmonics of the inverter output voltage. The reduced harmonics also mitigate the interharmonic distortions at the source side. The empirical excitation of various intensities of dithering results in mitigation of harmonic and interharmonic distortions by approximately up to 10 dB.

3.1 Introduction

Adjustable speed drives (ASDs), which consist of a rectifier, a DC link, and an inverter, have been employed in commercial and industrial loads. According to the characteristics of the DC link and the inverter, ASDs are classified in numerous ways [22]. Among the inverter classifications, voltage-sourced

PWM inverters are commonly used for ASDs because of good power factor, controllability, and their ability to produce nearly sinusoidal current to the output [23]. Furthermore, PWM inverters obtain their DC input from the uncontrolled rectifier which can be implemented using simple diode bridges.

Meanwhile, due to nonlinearities in the power electronic devices, i.e., a rectifier and an inverter, VSI-ASDs emit harmonics to the power source, DC link, and the load. As described in Chapter 2, a PWM inverter causes harmonic distortions to the output load, which can significantly impact motors [24]. PWM harmonics can also be reflected from the inverter to the DC link and coupled with the source-side current through the rectifier. The coupled PWM harmonics appear as interharmonics at the source side which can cause side effects to the other loads connected to the same power source, as described in Chapter 1.

Researches on interharmonics in power systems have been focused on effective detection methods. Signal processing methods such as harmonic filtering [25], adaptive window width [26], and support vector machine [27] provide clear information of interharmonic frequencies and magnitudes. A cross bicoherence method [28] quantifies the intensity of nonlinear coupling between two different frequency sources, which can prove the dominant sources of interharmonic distortion.

This chapter focuses on the mitigation of harmonic and interharmonics as well by applying a dithering method to PWM inverter. The fundamental concept of PWM dithering is pulse width randomization which mitigates the magnitudes of PWM harmonics. The width of each pulse in PWM signal periodically varies where the periodicity determines the fundamental frequency. Maintaining the fundamental periodicity, the dithering randomizes the width

of each pulse in an period. Thus, harmonics associated with the pulses in each period are mitigated while the fundamental frequency is maintained. The magnitudes of the mitigated interharmonics are illustrated using conventional Fourier transform method and the relationship between harmonics and interharmonics are evaluated using cross bicoherence analysis. In the following sections, the definition of cross bicoherence, simulation result, and conclusion are discussed.

3.2 Cross bicoherence for interharmonic detection in ASDs

A cross bispectrum quantifies quadratic interactions of two individual signals in the bi-frequency plane, and the cross bicoherence is a normalized cross bispectrum. The definition and properties of general cross bispectrum/bicoherence are described in [29]. Depending on the application, the cross bispectrum/bicoherence can be defined in many different ways by switching the sequence of signals. For our specific application of the cross bicoherence to interharmonic detection associated with ASD systems, we use the cross bicoherence definition in [28] for the system configured in Fig. 3.1. The definition of the cross bispectrum, $S_{xyy}(f_1, f_2)$, and the corresponding cross bicoherence, $c^2(f_1, f_2)$, are as follows:

$$S_{xyy}(f_1, f_2) = E[X(f_1)Y(f_2)Y^*(f_3)] \tag{3.1}$$

$$c^2(f_1, f_2) = \frac{|S_{xyy}(f_1, f_2)|^2}{E[|X(f_1)Y(f_2)|^2]E[|Y(f_3)|^2]} \tag{3.2}$$

where $E[\cdot]$ denotes an expectation operator. The frequency index f_3 satisfies the frequency selection rule which can be expressed as $f_3 = f_1 + f_2$. Variables,
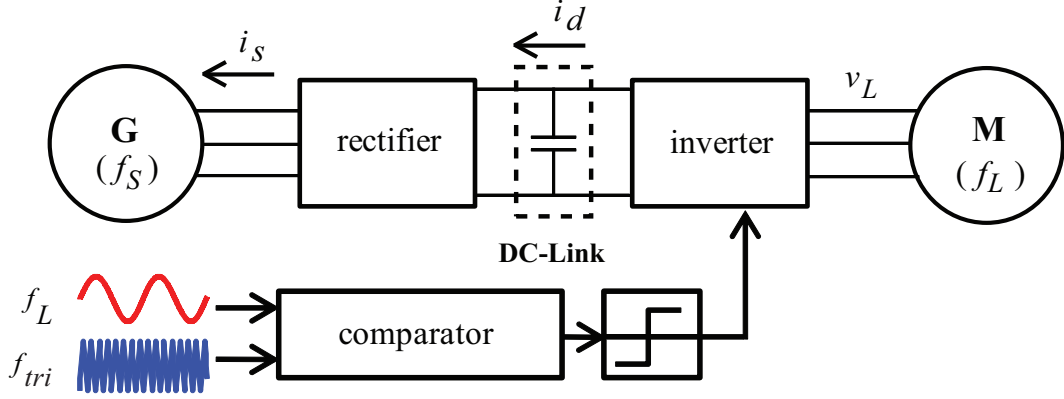
Figure 3.1: PWM-ASD configuration

$X(f)$ and $Y(f)$, correspond to the frequency responses of the currents measured at the DC link side (i_d in Fig. 3.1) and the source side (i_s in Fig. 3.1), respectively. Because interharmonic current at the source-side is caused by interactions between currents at the source side and the DC link as shown in (2.19), the cross bicoherence can quantify the intensity of correlation between i_d and i_s. In more detail, the cross bicoherence, $c^2(f_1, f_2)$, indicates the intensity of nonlinear frequency coupling between $Y(f_3 = f_1 + f_2)$, $X(f_1)$ and $Y(f_2)$, and is bounded between 0 and 1. The closer $c^2(f_1, f_2)$ is to 1, the more likely $Y(f_3 = f_1 + f_2)$ is the result of a nonlinear quadratic interaction between $X(f_1)$ and $Y(f_2)$. Consequently, the value of the cross bicoherence at a certain frequency point in the (f_1, f_2) plane can tell us whether the frequency component under consideration is an interharmonic component or not.

In practical analysis of (3.1) and (3.1), the number of computation is cubically proportional to the number of samples in $X(f)$ or $Y(f)$. Fortunately, symmetry properties of Fourier transform can be extended over the entire two dimensional frequency plane of f_1 and f_2. Based on the symmetry of the Fourier transform, $X(-f) = X^*(f)$, and sampling theory, following symmetry

32

properties can be derived for cross bispectrum.

I. $S_{xyy}(f_1, f_2) = S_{xyy}^*(-f_1, -f_2)$

II. $f_1 \leq f_N$

III. $f_1 + f_2 \leq f_N$

IV. $S_{xyy}(f_1, f_2) = S_{xyy}(f_1, -f_1 - f_2)$

where f_N denotes the Nyquist frequency which guarantee the aliasing-free sampling. The symmetry lines associated with the above symmetry properties and the corresponding region of symmetry are illustrated in Fig. 3.2. 'Σ' indicates a sum frequency interaction region, and 'Δ' indicates a difference frequency interaction region. In Symmetry IV, the second frequency components, f_1 and $-f_1 - f_2$ are symmetric about $f_2 = -f_1/2$. Thus, The 'Δ' region is bounded by the line, $f_2 = -f_1/2$, as shown in Fig. 3.2.

3.3   ASD simulation environment

To evaluate the effects of a dithering on the mitigation of harmonics/interharmonics, we implemented a VSI-ASD system using the PSCAD/ EMTDC program. Fig. 3.3 illustrates the simulated VSI-ASD model, where corresponding rated values are summarized in Table 3.1. As a power source, the three-phase voltage source in PSCAD/EMTDC library is selected. Three pairs of diode consist the six-pulse rectifier, and 3000 μF capacitor configures a voltage source inverter. The PWM inverter is composed of six IGBTs and free wheel diodes. PWM signals turn on and off each gate of IGBTs to convert
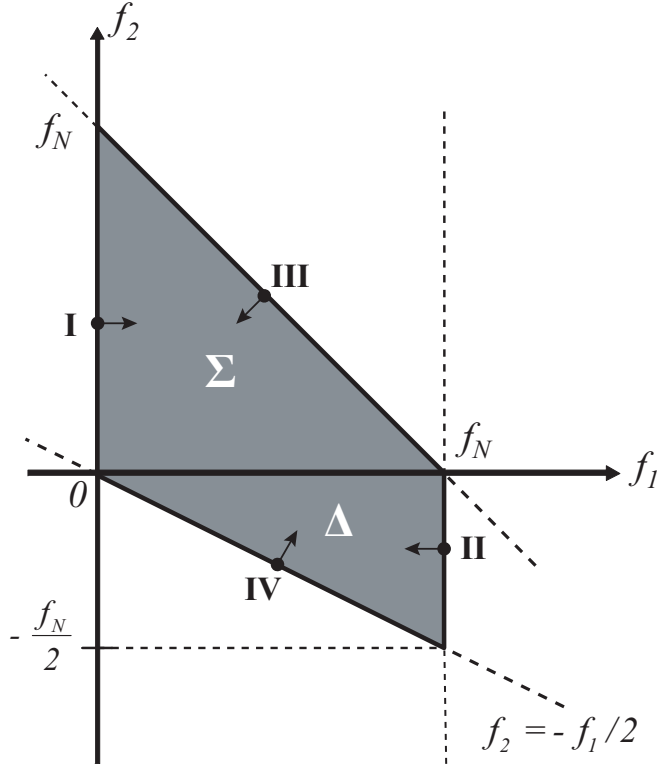
Figure 3.2: Region of symmetry for the definition in (3.1)

DC power into PWM AC power. Gaussian noise data are generated in MAT-LAB simulation and imported as noise waveform. Current and voltage data are measured in PSCAD/EMTDC and exported into MATLAB for further processing.

In PWM operation, modulation ratio, m_a, is defined by the ratio between the peak values of the reference signal and the switching signal. As modulation ratio increases, the associated PWM waveform has wider pulse width as shown in Fig. 3.4. The wider pulse width corresponding to the peak value of the sinusoidal produces more harmonics associated with the fundamental frequency of the PWM signal. If m_a increases to infinity, the PWM
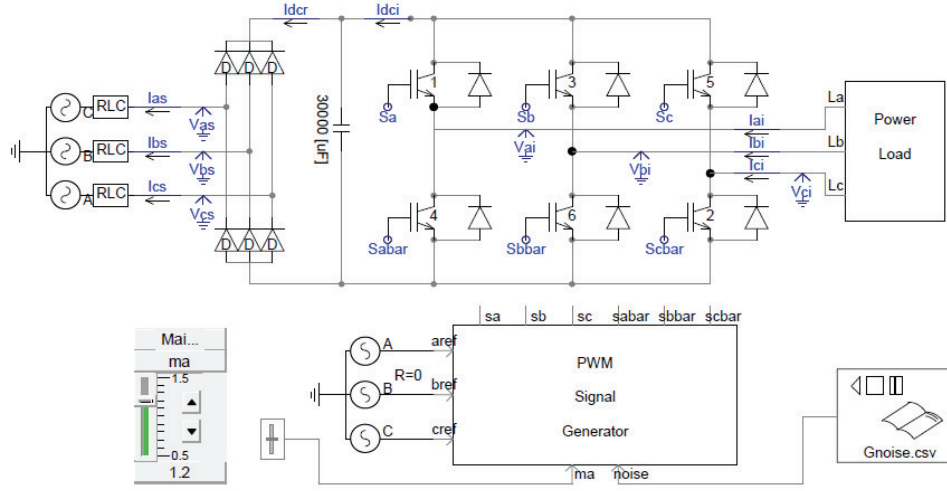
Figure 3.3: PSCAD/EMTDC model for PWM-ASD

Table 3.1: Rated values of PWM-ASD in Fig. 3.3

	Source	DC link	Load
fundamental frequency	60 Hz	0 Hz	13 Hz
rms voltage	530 V	750 V	530 V
rated power	50 kVA	.	37.3 kW 21.1 kVar

waveform becomes square waveform to produce more harmonics of fundamental frequency. In this simulation, m_a of 1.4 is applied to the PWM signal generator, which denotes the PWM inverter operates in the over modulation region.

If the additive dither noise is injected to the sinusoidal reference signal, transition edges of the PWM signal are randomly varied. The variation of transition edges can reduce periodicity of harmonics. Thus, greater magnitude
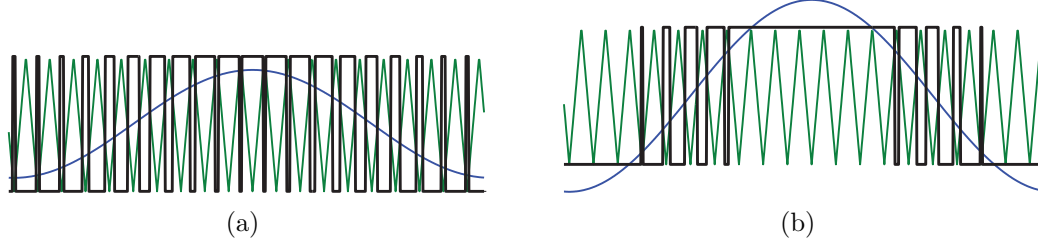
Figure 3.4: Modulation modes of PWM inverters: (a) under modulation mode (b) over modulation mode

of dither more reduces the magnitude of harmonics. However, randomized edges in each pulse appear as increased noise spectral density in the frequency domain. Therefore, we quantify the intensity of dithering by means of dithering ratio (DR) to evaluate the effect of dithering on harmonics and interharmonics in VSI-ASD system. The DR is defined as follows:

$$\text{DR} = \frac{\text{rms value of the dithering noise signal}}{\text{rms value of the reference signal}} \tag{3.3}$$

Switching frequency of the PWM inverter, which is described as f_{tri} in Fig. 3.1, is 2080 Hz, and corresponding modulation index, m_f, is 160 (=2080 Hz/13 Hz). Referring Tables 2.1 and 2.2, the feasible harmonic and interharmonic frequencies, described in (2.15) and (2.24), can be simplified for the non-triple and even integer of m_f as follows:

$$f_l^h = h \cdot f_l \tag{3.4}$$

$$f_s^{ih} = |(6m \pm 1) \cdot f_s \pm l \cdot f_l| \tag{3.5}$$

where f_l^h and f_s^{ih} denote harmonic and interharmonic frequency at the load- and the source-side, and $h = 2, 3, \cdots$, $m = 0, 1, \cdots$, $l = 1, 2, \cdots$.

36

3.4 Analysis of simulation result

In this section, we demonstrate harmonic and interharmonic characteristics at the load and at the source sides when the dithering method is applied to the PWM inverter. First, conventional spectral analysis is demonstrated for load voltage and source current. After investigating the spectral magnitude, we apply the cross bicoherence method to the source and the DC-side current in order to verify whether the affected frequencies at the source-side is associated with the load-side harmonics.

3.4.1 Spectral analysis for harmonics and interharmonics

Fig. 3.5(a), (b), and (c) present frequency responses of v_L (load terminal voltage - see Fig. 3.1) at the load of the VSI-ASD with DR of 0, 0.2, and 0.4, respectively. Each graph is normalized by the fundamental voltage and plotted in dB full scale (dBFS) and detail values of the harmonic magnitudes are enumerated in Table. 3.2. In Fig. 3.5(a), the 5th (65 Hz) and 7th (91 Hz) harmonics are dominant, where each magnitude is -31.2 dB and -38.9 dB of the fundamental voltage, respectively. Besides 5th and 7th harmonics, other harmonics also appear at the integer multiple of the fundamental frequency even if their magnitudes are small. The existence of those harmonics is also consistent with (3.4). The frequency response of load voltage, v_L, for DR of 0.2 is illustrated in Fig. 3.5(b). Compared with Fig. 3.5(a), the magnitude of the 5th and 7th harmonics reduce by 4.1 dB (from -31.2 dB to -35.3 dB) and 14 dB (from -38.9 dB to -52.9 dB), respectively. Meanwhile, the level of noise increases around to -50 dB. When we increase a DR to 0.4, the 5th and 7th harmonics further decrease. Compared with Fig. 3.5(a), the magnitudes of 5th and 7th harmonics reduce by 12.4 dB (from -31.2 dB to -43.6 dB) and 0.3 dB
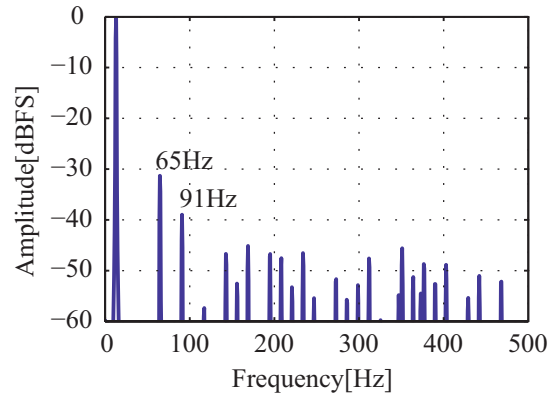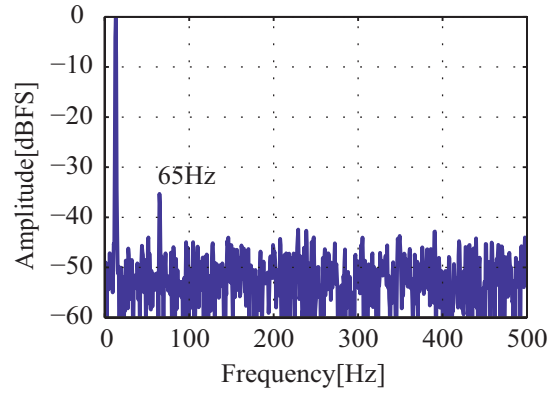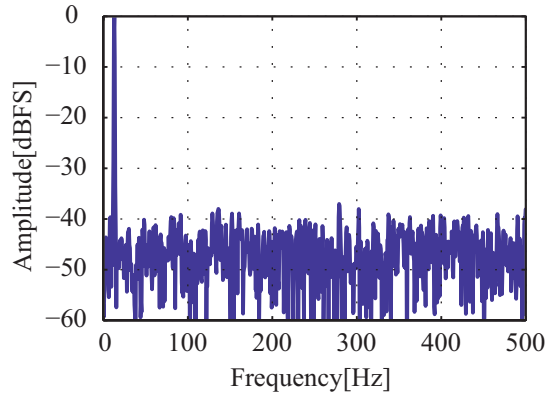
Figure 3.5: Frequency response of the load voltage, v_L, for (a) DR = 0 (b) DR = 0.2 (c) DR = 0.4

Table 3.2: Magnitude of harmonic components in v_L with respect to the fundamental component

Harmonic frequency f_H^{load} [Hz]	Magnitude of harmonics for DR = 0	Magnitude of harmonics for DR = 0.2	Magnitude of harmonics for DR = 0.4
65 (=13×5)	-31.2 dB	-35.3 dB	-43.6 dB
91 (=13×7)	-38.9 dB	-52.9 dB	-39.2 dB

(from -38.9 dB to -39.2 dB), respectively. However, the noise floor increases to approximately -45 dB.

Consequently, the dithering method mitigates harmonics associated with the fundamental frequency and also increases the noise floor. When the harmonic components are greater than the noise floor, the dithering effectively mitigates those harmonics. However, once the harmonic tones are hidden by the noise floor, the effect of dithering cannot be evaluated such as the case for the 7th order harmonic. Thus, the cross point of the noise floor and the magnitude of harmonic tones sets the limitation of the dithering method in a view of harmonic distortions.

Frequency responses of i_S at the source side of the VSI-ASD are illustrated in Fig. 3.6 for DR of 0, 0.2, and 0.4. The current spectra are normalized with respect to the current level at 60 Hz and are plotted in dBFS. Dominant harmonics at 300 Hz and 420 Hz are caused by the six-pulse rectifier, which correspond to $(6m \pm 1) \cdot f_s$ in (3.5). Thus, those harmonics are not affected by the dithering at the PWM inverter. Meanwhile, interharmonic components associated with the PWM inverter can be affected by the dithering. Frequencies of dominant interharmonic components are indicated in Fig. 3.6(a) and exact
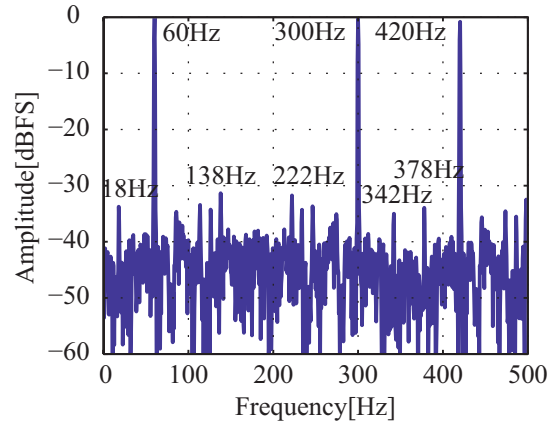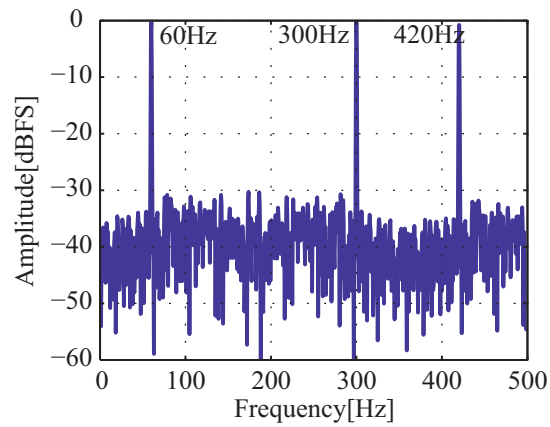
Figure 3.6: Frequency response of the source current, i_S, for (a) DR = 0 (b) DR = 0.2 (c) DR = 0.4

40

Table 3.3: Magnitude of interharmonic components in i_S with respect to the fundamental component

Interharmonic frequency f_{IH}^{source} [Hz]	Magnitude of interharmonics for DR $= 0$	Magnitude of interharmonics for DR $= 0.2$	Magnitude of interharmonics for DR $= 0.4$
18 $= \|60 - 6 \times 13\|$	-29.2 dB	-33.8 dB	-37.4 dB
138 $= \|60 + 6 \times 13\|$	-29.4 dB	-31.4 dB	-40.6 dB
222 $= \|60 \times 5 - 6 \times 13\|$	-29.4 dB	-31.8 dB	-40.9 dB
378 $= \|60 \times 5 + 6 \times 13\|$	-30.0 dB	-33.9 dB	-37.5 dB
342 $= \|60 \times 7 - 6 \times 13\|$	-30.4 dB	-35.0 dB	-39.6 dB

magnitudes of interharmonics with respect to the fundamental component are listed in Table. 3.3. In Fig. 3.6(a), interharmonic tones of approximately -30 dB with respect to the 60 Hz current at 18 Hz, 138 Hz, 222 Hz, 342 Hz, and 378 Hz can be interpreted by (3.5). Corresponding pairs of (m, l) producing the source-side interharmonics in (3.5) are (0, 4) for 18 Hz and 138 Hz, (1, 4) for 222 Hz and 378 Hz, and (2, 4) for 342 Hz. The interharmonics slightly greater than -30 dB of the fundamental current are reduced to below -40 dB by dithering, as shown in Fig. 3.6(b). Harmonics of f_S (=60 Hz) at 300 Hz, and 420 Hz remain at the same level because those harmonics are induced by the rectifier not the PWM inverter. Fig. 3.6(c) indicates that interharmonic tones disappear into the noise when the DR is increased to 0.4. Meanwhile, the noise level exceeds -40 dB from the fundamental current.

The value of harmonic parameter l in (3.5) corresponds to the order of harmonic associated with f_l (=13 Hz) which appears at the DC link. In the

41

measurement, we focus on harmonics whose frequencies are located within 0 Hz to 100 Hz, because those harmonics can cause interharmonics close to the fundamental frequency, 60 Hz, at the source-side. Harmonics/interharmonics close to the fundamental frequency are difficult to be removed by L-C type harmonic filters due to the limitation of filter order.

The dominant harmonics for various DRs appear at 78 Hz (=13 Hz × 6) and 42 Hz (=13Hz × 4) as shown in Fig. 3.7(a), (b), and (c). The exact magnitude of the harmonics at 42 Hz and 78 Hz are also enumerated in Table 3.4. Fig. 3.7(a) shows the frequency response of i_d when the DR is 0. The 6th order harmonic of f_l appear as a dominant harmonic into the DC link and the corresponding magnitude is -29.3 dB with respect to the fundamental value. When the DR increases to 0.2, the 78 Hz tone decreases by 4 dB (from -29.3 dB to -33.3 dB) as shown in Fig. 3.7(b) at the cost of the increased noise floor. When DR of 0.4, the 78 Hz tone disappear into the noise level as shown in Fig. 3.7(c). Meanwhile, the frequency component at 42Hz appears as a dominant harmonic whose magnitude of -34.1 dB with respect to the fundamental value.

Consequently, the harmonic component at 78 Hz reduces as the DR increases. Referring the interharmonic current spectra in Fig. 3.6, the frequency component at 78 Hz can be inferred to cause the source-side interharmonics at 18 Hz, 138 Hz, 222 Hz, 342 Hz, and 378 Hz. The correlation between the 78 Hz-component at the DC link and the source-side interharmonics can be validated using the cross bicoherence analysis.
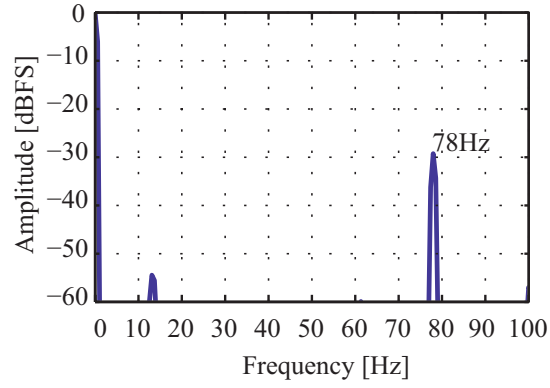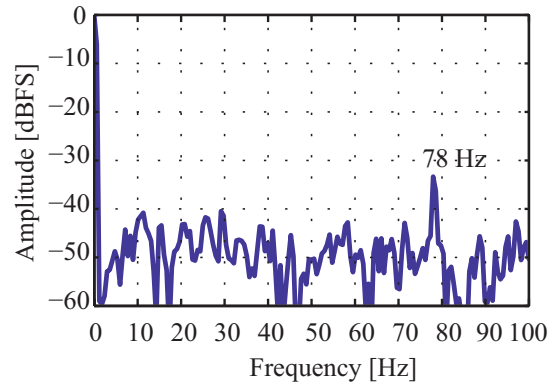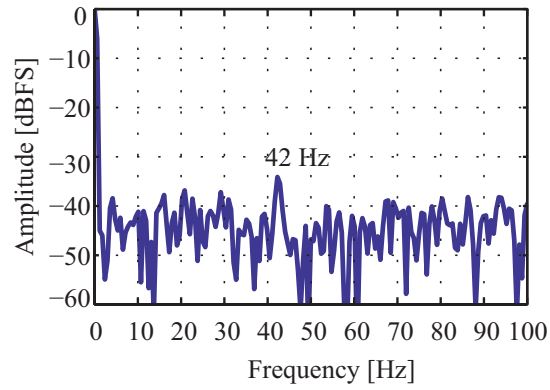
Figure 3.7: Frequency response of the DC-side current, i_d, for (a) DR $= 0$ (b) DR $= 0.2$ (c) DR $= 0.4$
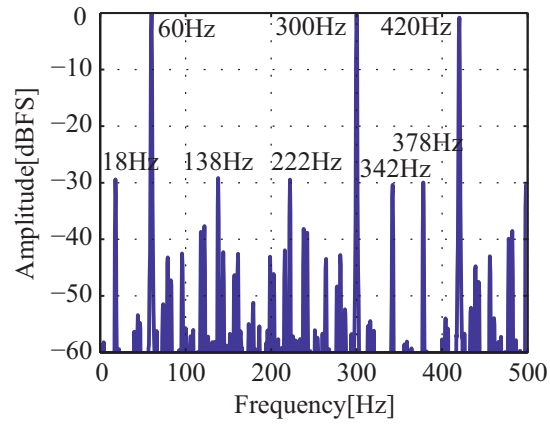
43

Table 3.4: Magnitude of interharmonic components in i_d with respect to the fundamental component

Harmonic frequency f_h^{dc} [Hz]	Magnitude of harmonics for DR = 0	Magnitude of harmonics for DR = 0.2	Magnitude of harmonics for DR = 0.4
42 (=13×4)	-82.1 dB	-61.4 dB	-34.1 dB
78 (=13×6)	-29.3 dB	-33.3 dB	-40.1 dB

3.4.2 Cross bicoherence analysis for interharmonics

Fig. 3.8 illustrates the cross bicoherences between the source current, i_S, and DC-side current, i_d, for a DR of (A) 0, (b) 0.2, and (c) 0.4. One axis of the bi-frequency plane for cross bicoherence corresponds to the source-side frequency and the other axis corresponds to the DC side frequency. The investigated frequency ranges are from -120 Hz to 120 Hz for source-side frequency, indicated as 'Frequency-Is', and from 0 Hz to 100 Hz for DC-side frequency, indicated as 'Frequency -Id', where the frequency interaction between 60 Hz at the source and 78 Hz at DC link can be investigated. Fig. 3.8(a) indicates that both source- and DC-side frequencies are strongly correlated at (60 Hz, 78 Hz), which can cause |60±78| Hz interharmonic frequencies at the source-side. Thus, the frequency tones at 18 Hz and 138 Hz in Fig. 3.6(a) can be regarded as interharmonics caused by (60 Hz, 78 Hz) coupling. Fig. 3.8(c) shows that the intensity of (60 Hz, 78 Hz) coupling reduces when a DR is 0.2. Instead of reduced interaction at (60 Hz, 78 Hz), DC-side noise is coupled with the source frequency. However, the interaction between fundamental source and noise is not concentrated at specific frequency but spreads in wider range of frequency with smaller density. Fig. 3.8(e) illustrates that cross bicoherence between

source and DC-side currents for a DR of 0.4. The cross bicoherence at (60 Hz, 78 Hz) is reduced to noise-coupling level. Meanwhile, source frequencies are coupled more with DC-side noise with increased intensity of interaction. Increased couplings with noise tones also corresponds to the increased noise floor in Fig. 3.6(c).

3.5 Conclusion

We have described the application of dithering in order to mitigate harmonics and interharmonics in a VSI-ASD. The mitigation of the load-side harmonics, associated with load frequency, f_l, enables us to reduce the source-side interharmonics without harmonic filters. The mitigated harmonics and interharmonics were investigated in conventional power spectra. Cross bicoherence method was also applied to verify the source of interharmonics. Frequency interactions in the bi-frequency plane provided straightforward information regarding the interharmonic frequencies, which is also coincident with (3.5). As the intensity of dithering increased, harmonics and interharmonics were reduced but the noise level increased. Thus, optimized level of dithering can be provided for specific limitations for harmonic/interharmonic and noise level.

The ASD system simulated in this chapter is composed of a single power source and load, thus the cause of interharmonics might be easily found without cross bicoherence analysis. However, power sources are generally connected to multiple loads and other sources, frequency coupling information is very useful to find the cause of interharmonics. Harmonic reduction method by dithering PWM signals not only mitigate harmonics at the load side but interharmonics at the source side. Furthermore, the dithering method has an advantage over hardware implementation because the dithering is implemented

at the "signal" level to manage "power" characteristics.
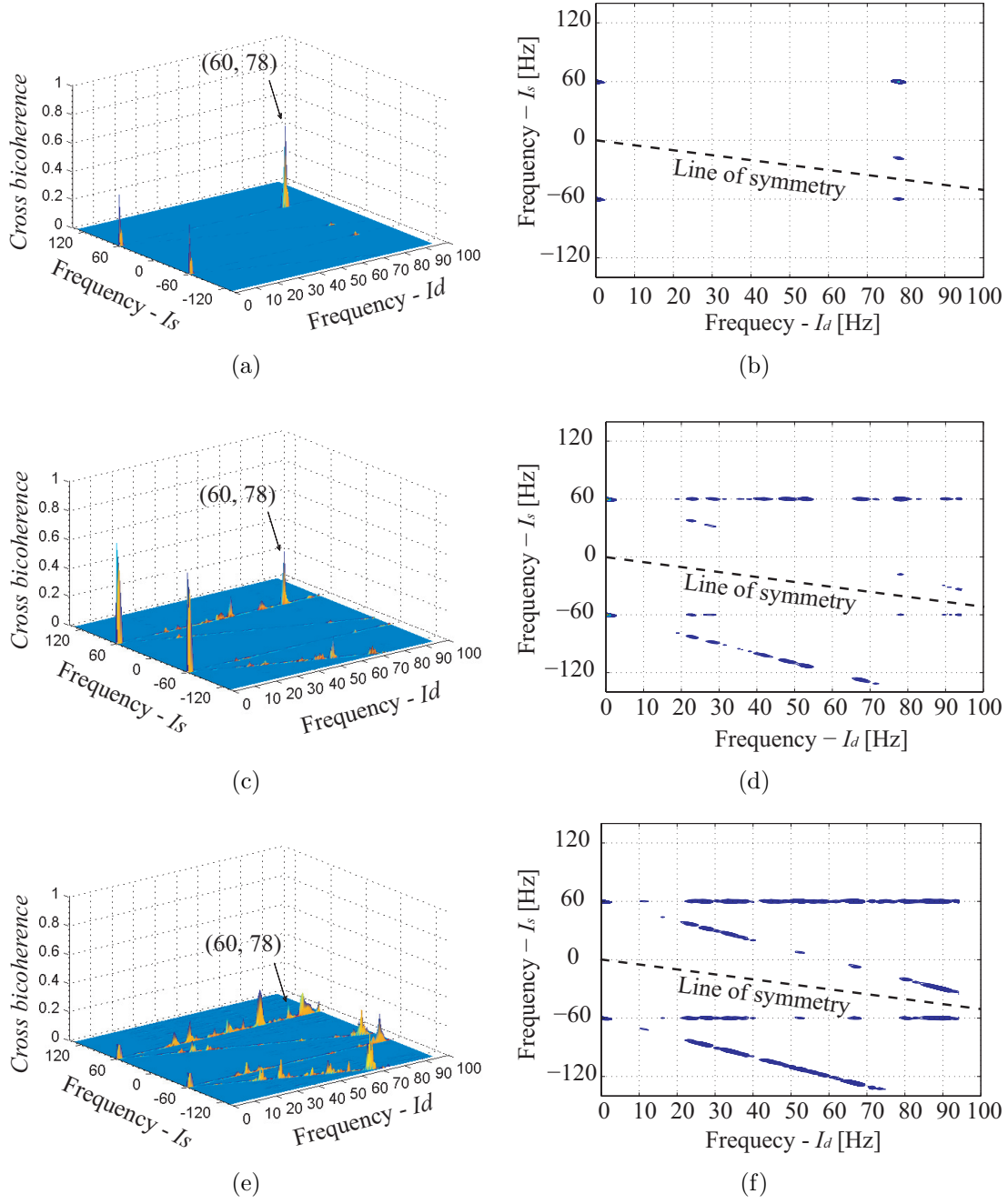
Figure 3.8: Cross bicoherence between source (i_S) and dc-side (i_d) current for (a) DR = 0 (b) DR = 0.2 (c) DR = 0.4

47

Chapter 4

Mitigation of harmonics of PWM inverters using dithered sigma-delta modulation

This chapter presents the application of dithered sigma-delta modulation ($\Sigma\Delta$M) in mitigating low and high frequency harmonics of pulse-width modulated (PWM) inverters without increasing switching losses. A PWM bit stream generated by a one-bit first order discrete $\Sigma\Delta$M is converted into a continuous pulse train which controls the inverter operation. The minimum pulse width of the pulse train is strictly defined by the sampling ratio, which prevents the inverter from missing switching operations. The spectrum of the pulse train demonstrates reduction of low and high frequency harmonics compared with the conventional sinusoidal PWM (SPWM), dithered SPWM, and carrier frequency modified SPWM spectra. The dithered $\Sigma\Delta$M bounds all spectral densities of harmonics and noise below -30 dB with respect to the magnitude of the fundamental component. Furthermore, the dithered $\Sigma\Delta$M does not increase the number of switching events. Meanwhile, comparable SPWMs produce harmonic peaks at a particular frequency or increase the number of switching event.

48
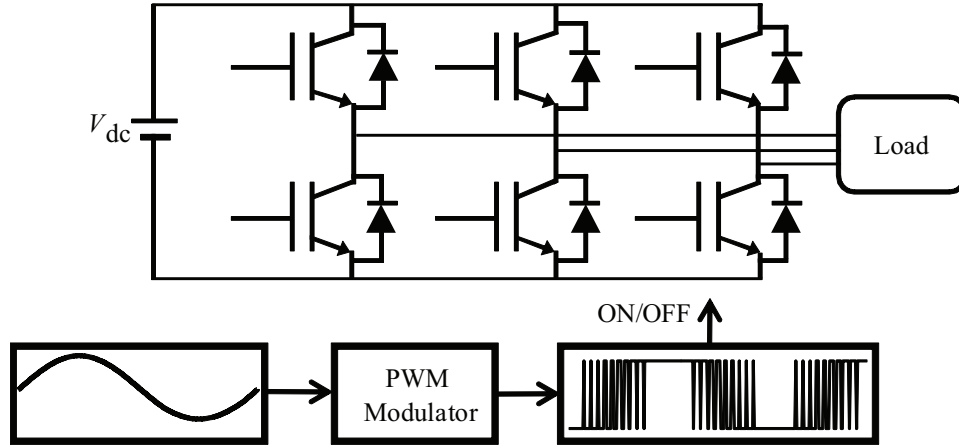
Figure 4.1: PWM inverter configuration

4.1 Introduction

A PWM inverter, configured in Fig. 4.1, is favored as DC/AC power converters owing to their energy efficiency over a wide range of output frequencies. The fundamental principle of a PWM inverter is to generate a DC pulse-train where the pulse width varies with a desired frequency. Due to inherent characteristics of a rectangular pulse, a PWM waveform inevitably produces harmonics. Moreover, it was demonstrated in Chapter 3 that the PWM harmonics can also cause interharmonic distortions at the source side of ASDs. When a dithering method was applied to mitigate PWM harmonic distortions, we observed that the interharmonics associated with PWM harmonics was also decreased. The relationship between PWM harmonics and associated inter-harmonics was also evaluated performing cross bicoherence analysis. Thus, in this chapter, we focus on the methods to mitigate PWM harmonics.

The pulse width of a PWM signal periodically varies where the period corresponds to the inverse of the fundamental frequency. The periodicity

of the pulse width produces harmonics associated with the fundamental frequency. Each period is composed of minimum-width pulses associated with the switching frequency and its harmonics.

Harmonic reduction methods in a low frequency range, associated with the fundamental frequency, have been implemented through switching angle calculations per each cycle. Examples of these methods are described as follows. Harmonic elimination PWM (HEPWM) inverter and equal area PWM (EAPWM) inverter [30] selectively reduce particular orders of harmonics. These methods are based on the pre-calculation of switching angles from the nonlinear equations which characterize the fundamental harmonics with respect to the switching angles. The centroid PWM (CPWM) technique [31] provides improved harmonic characteristics, which generates switching angles from the centroid of a sectionalized sinusoid. In HEPWM, EAPWM, and CPWM techniques, calculated switching angles are stored in a memory and applied to the inverter gates. Although these methods effectively reduce specific low-frequency harmonics, each switching operation appears as discrete tone because the stored angles periodically affect the inverter operation. HEPWM can be extended to the real-time applications by the fast algorithms based on the regular sampling theory [32] and the Walsh function [33]. Unfortunately, the switching frequency related harmonics still exist due to the periodic repetition of the narrow-width pulses. The space vector modulation (SVM) technique defines each state of the inverter switching on the vector domain where the switching state and corresponding voltage locus of HEPWM inverter can be represented [34]. The optimal firing angles can be found from a vector diagram. However, repetition of finite states induces periodicity of narrow pulse-width which appears as high frequency harmonics.

Harmonic reduction methods in the high frequency range have been introduced based on harmonic spreading methods. The hysteresis current regulating method [35] varies the switching frequency, which reduces a large peak at a particular frequency. However, the actual switching depends on the hysteresis band, which produces periodic tones over a wide range of frequencies. Furthermore, the switching frequency can interfere with the fundamental frequency under specific load conditions. The randomly modulated carrier [36], the switching frequency modulation [37], and the frequency hopping [38] methods spread the switching frequency over over a limited band to reduce acoustic noise or EMI emission. These methods commonly modify the carrier signal of a sinusoidal PWM (SPWM) inverter. Since SPWM is most commonly used in the industry due to simple implementation [39], the carrier frequency modification methods are advantageous in practical implementation. However, these methods are focused on reducing high-frequency harmonics without harmonics associated with the fundamental frequency.

In this chapter, we present mitigation of harmonics using dithered sigma-delta modulation ($\Sigma\Delta$M). The application of conventional $\Sigma\Delta$M to inverters, based on continuous-time operation, was proposed in [40, 41]. We introduce fully discrete time $\Sigma\Delta$M with discrete dither to the comparison process. Dithering is a popular method in analog-to-digital conversion (ADC) to improve the resolution of digitized signals. For PWM signals, the improved resolution corresponds to the reduced harmonics because increased resolution indicates that the modulated signal becomes more sinusoidal. Furthermore, the noise floor of the dithered $\Sigma\Delta$M is suppressed in low frequency region and increases with frequency. If inherent $\Sigma\Delta$M samples are interpolated by zero-order holding, the advantageous noise-shaping property is repeated at every
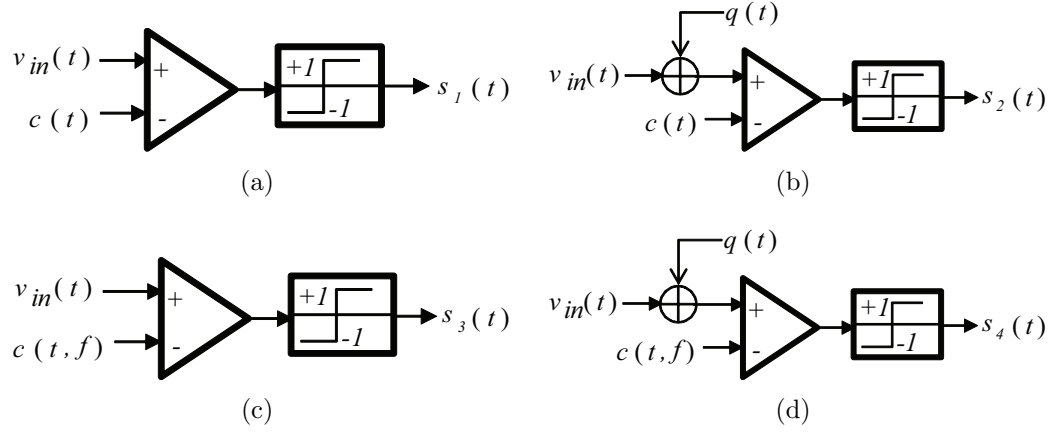
Figure 4.2: Block diagrams of SPWM: (a) conventional SPWM (b) dithered SPWM (c) random carrier SPWM (d) dithered random carrier SWPM

sampling frequency. Thus, the dithered $\Sigma\Delta$M method can mitigate both low and high frequency harmonics.

The harmonic characteristics of the dithered $\Sigma\Delta$M signal are compared with those of conventional, dithered, and randomly modulated carrier SPWM signals. The result shows that the dithered $\Sigma\Delta$M effectively mitigates low and high frequency harmonics without increasing switching loss.

4.2 Simulation evaluation of PWMs

4.2.1 Sinusoidal PWM

A SPWM waveform is basically generated by the comparison between a reference signal and a carrier signal. Fig. 4.2 represents block diagrams of SPWM topologies. Fig. 4.2(a) shows the configuration of a conventional SPWM, which is composed of a comparator and a hard limiter. $v_{in}(t)$ is a sinusoidal reference signal which determines the fundamental frequency of the

modulated signal. In our simulation, $v_{in}(t)$ unitless sinusoidal waveform whose frequency and amplitude is 40 Hz and 1.2, respectively. $c(t)$ in Figs. 4.2(a) and (b) is unitless triangular waveform where its frequency and the peak value is 1.2 kHz and 1, respectively. $q(t)$ in Figs. 4.2(b) and (d) is a zero-mean Gaussian random signal. The standard deviation of $q(t)$ is 0.42, which is 40% of the rms value of the reference signal. $q(t)$ is added to the reference signal, $v_{in}(t)$, as a dither, which randomizes switching timing. The purpose of randomized timing is to spread out harmonic tones associated with the fundamental frequency. $c(t, f)$ in Figs. 4.2(c) and (d) indicates frequency-varying carrier signal, where the frequency is Gaussian random variable. The average and the standard deviation of the frequency are 1.2 kHz and 5 Hz, respectively. The random-frequency carrier, $c(t, f)$, spreads the discrete tones associated with the switching frequency into the frequency band around the average frequency. Fig. 4.2(d) shows an SPWM block diagram where both $q(t)$ and $c(t, f)$ are applied. The effects of both $q(t)$ and $c(t, f)$ will be compared with dithered $\Sigma\Delta$M signal in the next section.

The modulation ratio (m_a), defined by the ratio between the amplitude of the sinusoidal reference and the carrier signal, is 1.2. The modulation index (m_f) is 30, where m_f is defined by the ratio between the reference frequency and the carrier frequency. As described in Chapter 2, if m_f is an even integer, feasible harmonic frequencies of SPWM inverter output, f_l^h are characterized as follows:

$$f_l^h(m_f, j, k) = |m_f l \pm k| \cdot f_l \qquad (4.1)$$

where l and k are integers described in Table 2.1 and f_l denotes the load-side fundamental frequency. The parameters l and k are associated with the

53
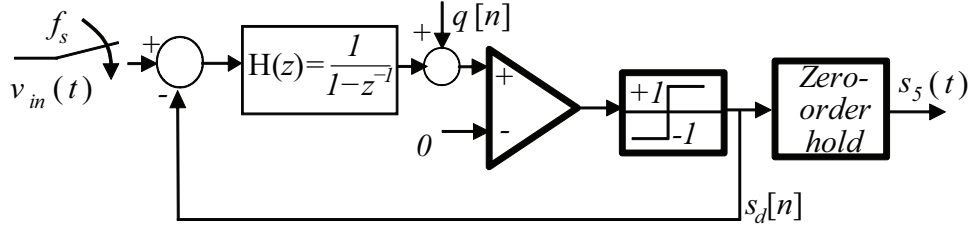
Figure 4.3: Block diagram of discrete-time one-bit first order $\Sigma\Delta$ modulator with dithering

switching frequency harmonics and fundamental frequency harmonics, respectively.

4.2.2 Sigma-delta PWM

The fundamental principle of $\Sigma\Delta$M is to convert an analog signal into a bit stream or a pulse train. In a digital application, the converted bit stream contains amplitude information of the original signal where the greater amplitude is represented as more 'high' bits. In a continuous time application, a converted pulse train with constant amplitude and variable duration describes the original signal where the the duration of the pulse corresponds to the amplitude of the original signal.

In our application, we applied a discrete one-bit first order $\Sigma\Delta$M to the gating signals of a PWM inverter. Because the gating signal requires two levels, 'high' and 'low', to turn on and off the switching device of the inverter, one bit is sufficient to represent the gating signal. Each pulse width of the PWM gating signal is implemented as the number of consecutive 'high' bits. The configuration of the discrete-time one-bit first order $\Sigma\Delta$M is illustrated in Fig. 4.3. Unlike the continuous-time $\Sigma\Delta$M in [40, 41], the discrete model performs sampling first. After the sampling, all processes are performed in

54

the discrete time domain, which can be conveniently implemented by means of DSP modules. The noise signal, $q[n]$, is also generated in discrete time. The modulated pulse train has a minimum pulse width of $1/f_s$, which can guarantee reliable inverter switching unless $1/f_s$ is shorter than the minimal response time of the inverter.

The equivalent carrier frequency and spectral characteristics of $\Sigma\Delta M$ are also described with respect to the sampling frequency, f_s. Because a carrier signal does not exist in the $\Sigma\Delta M$, the equivalent carrier frequency can be derived from the minimal time to produce a pulse. In the $\Sigma\Delta M$ process shown in Fig. 4.3, $s_d[n]$ can have at most one pulse during every twice of sampling time, $2/f_s$. Compared a SPWM process which produce at most one pulse during one period of a carrier signal, $2/f_s$ corresponds to the period of the carrier frequency. Thus, a half of the sampling frequency, $f_s/2$, of the $\Sigma\Delta M$ signal corresponds to the carrier frequency in a SPWM. The equivalent carrier frequency, $f_s/2$, is also coincident with the highest frequency of $s_d[n]$.

According to [42], a $\Sigma\Delta M$ signal has a spectrum-shaping property where the noise spectral density is lower than the average value below the fundamental frequency and increases with frequency. Thus, the lowest noise spectral density of $s_d[n]$ exists at DC frequency and the highest density appears at the $f_s/2$. If the dither fully spreads out all harmonics into the noise level, the highest spectral density except the fundamental tone exists at $f_s/2$. To employ $s_d[n]$ as a PWM signal to drive an inverter, $s_d[n]$ has to be interpolated using a zero-order holding process. The zero-order holder performs convolution of rectangular function and the impulse trains of $s_d(t)$ (time domain version of $s_d[n]$) in the time domain. Thus, the modulated signal, $s_5(t)$, and its frequency response can be expressed as follows:

$$s_5(t) = s_d(t) * rect[(t - \frac{1}{2f_s})f_s] \tag{4.2}$$

$$S_5(f) = S_d(f) \cdot \frac{\sin(\pi f/f_s)}{\pi f} \cdot e^{-\frac{j2\pi f}{2f_s}} \tag{4.3}$$

$$|S_5(f)| = |S_d(f)| \cdot \left| \frac{\sin(\pi f/f_s)}{\pi f} \right| \tag{4.4}$$

Because of the right-hand-side term, $\left| \frac{\sin(\pi f/f_s)}{\pi f} \right|$, in (4.4), the magnitude of $S_5(f)$ has a decaying property as frequency increases with notches at every multiple of f_s. Thus, even-order harmonics of the carrier frequency, $f_s/2$, do not appear in the discrete $\Sigma\Delta$M signal.

In our simulation, a 40 Hz sinusoidal signal is used as a reference signal, $v_{in}(t)$, where its amplitude is 0.75. The sampling frequency, f_s, is 3.6 kHz and the corresponding switching frequency is 1.8 kHz. Since the modulation principle of $\Sigma\Delta$M is different from the SPWM, using the same modulation ratio and switching frequency as SPWM methods produces a much wider pulse-width and less number of switching. Thus, the modulation ratio and sampling frequency are determined by inspecting the number of switching events in conventional SPWM inverter.

4.3   Analysis of simulation results

Frequency responses of randomized SPWM signals, described in Fig. 4.2, are demonstrated in Figs. 4.4 - 4.7. Each figure is plotted in dB full-scale (dBFS) where the magnitude of the fundamental tone is normalized at 0 dB. The horizontal axis indicates a frequency range up to 4 kHz. PWM-associated harmonics are investigated in the regions associated with (i) fundamental harmonics up to the 15th order, 600 Hz, (FH), (ii) the switching frequency (SH),

(iii) the 2nd order switching harmonic (SH2), and (iv) the 3rd order switching harmonic (SH3). Corresponding region for those harmonics are indicated as shaded areas in each figure.

Frequency response of conventional SPWM waveform is illustrated in Fig. 4.4, where distinguished points are marked as 'x'. The frequency and corresponding magnitude at each 'x' are enumerated in Table 4.1. As indicated in (4.1), SPWM harmonic frequencies are every linear combination of fundamental and carrier frequencies. The 3rd, 9th, 13th, and 15th harmonics in the FH region have magnitudes between -30 dB and -20 dB with respect to the fundamental component. The magnitude of the harmonic tone in the SH region is greater than -10 dB of the fundamental density where associated harmonic frequencies are 1120 Hz and 1280 Hz which corresponds to $l = 1$ and $k = 2$ in (4.1). Associated with the 2nd order harmonic of the switching frequency, harmonic tones between -20 dB and -10 dB of the fundamental component appear at 2280 Hz, 2360 Hz, 2440 Hz, and 2520 Hz in the SH2 region. The harmonic frequencies correspond to $l = 2$ and $k = 1, 3$ in (4.1). The 3rd order harmonic of the switching frequency produces harmonics at 3440 Hz and 3760 Hz in the SH3 region, which have magnitudes between -20 dB and -10 dB with respect to the fundamental frequency. Corresponding l and k values in (4.1) are 3 and 4, respectively.

When dithering is applied to the reference signal of SPWM, as shown in Fig. 4.2(b), the frequency response of the the PWM signal is illustrated in Fig. 4.5. The frequencies and magnitudes at the point 'x's are listed in Table 4.1.

Fig. 4.4, harmonic tones in the FH region are significantly reduced so that those magnitudes of harmonics are bounded to -40 dB except the 3rd
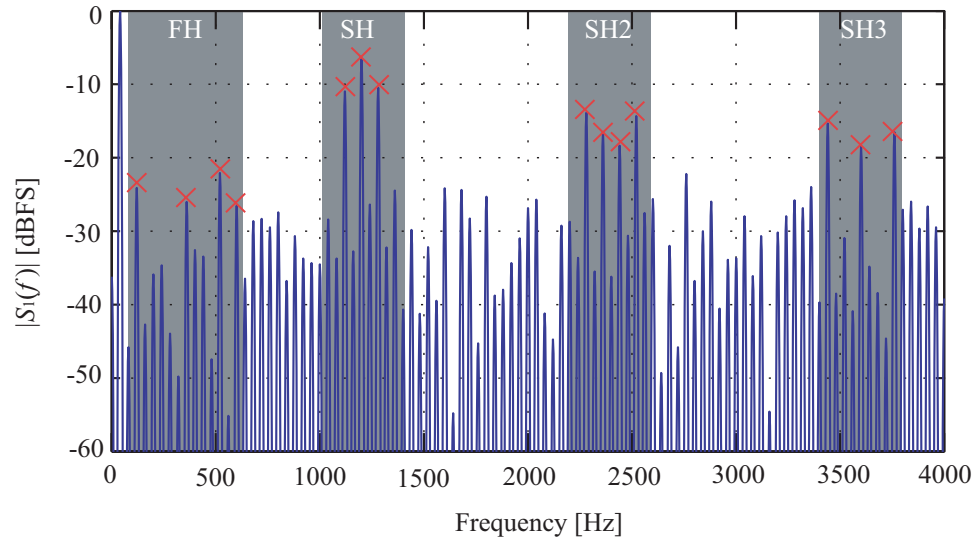
Figure 4.4: Frequency response of conventional SPWM
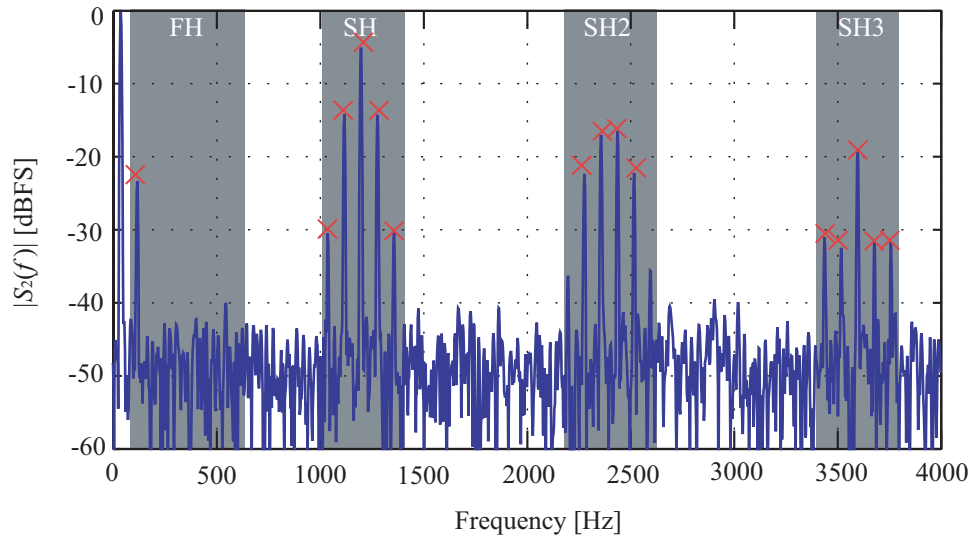
Figure 4.5: Frequency response of dithered SPWM

58

order harmonic. In the SH region, the carrier frequency harmonic at 1200 Hz is slightly increased from -6.55 dB to -4.95 dB. Meanwhile, harmonics associated with both the carrier and the fundamental frequencies are reduced. For example, harmonics are reduced to approximately -15 dB at $(1200 \pm 2 \cdot 40)$ Hz and to approximately -30 dB at $(1200 \pm 4 \cdot 40)$ Hz. In SH2 region, harmonics associated with the 2nd order harmonic of the carrier frequency and the third order harmonics of the fundamental frequency are mitigated to approximately -22 dB with respect to the fundamental magnitude at $(2 \cdot 1200 \pm 3 \cdot 40)$ Hz. In SH3 region, harmonics associated with the 3rd order of the carrier frequency and the 5th order of the fundamental frequency are significantly reduced by approximately 15 dB from those of the conventional SPWM harmonics. In the intermediate frequency regions between FH, SH, SH2, and SH3, harmonics associated with the fundamental frequency are bounded to approximately -40 dB while the noise floor caused by the dithering is formed between -40 dB and -50 dB. Thus, the dithered SPWM effectively mitigates fundamental frequency harmonics at the cost of the increased noise floor.

Fig. 4.6 illustrates the frequency response of the SPWM signal when the carrier frequency of the SPWM inverter is randomly varied with a fixed average frequency of 1.2 kHz. The distinctive harmonics whose frequencies can be described by (4.1) are marked as 'x'. Corresponding frequencies and magnitudes to 'x' are listed in Table 4.1. Meanwhile, harmonic frequency other than (4.1) can also appear owing to the randomness of the carrier frequency, which are marked as 'o'. Detail frequencies and magnitudes for 'o's are enumerated in Table 4.2.

Compared with the conventional SPWM spectrum shown in Fig 4.4, even order harmonics in the FH region are suppressed when the carrier fre-
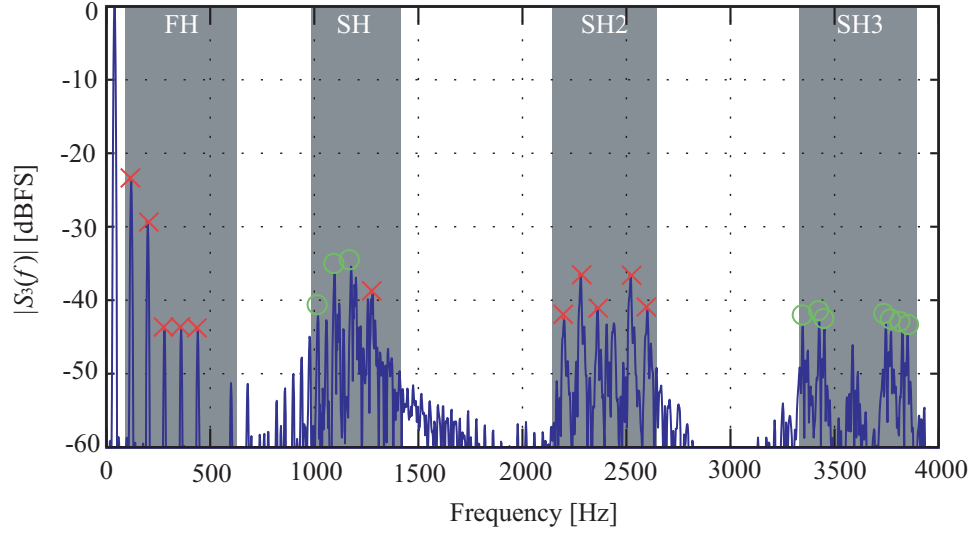
Figure 4.6: Frequency response of the random carrier SPWM

quency is randomized. However, the 3rd, 5th, 7th and 9th harmonics of the fundamental frequency are not reduced. In the case of 5th order harmonic, the magnitude is increased by approximately 6 dB. In the SH region, the maximum component of -35.42 dB appears at 1178 Hz, which is less than the carrier frequency harmonic of the conventional SPWM by approximately 30 dB. In the SH2 and SH3 regions, high frequency components associated with the carrier frequency harmonics are mitigated by more than 20 dB from those of the conventional SPWM where the width of harmonics tones are broader than those of Fig. 4.4.

Fig. 4.7 represents the effect of dithering and carrier randomization on SPWM at the same time. Harmonics at the frequencies of (4.1) are marked as 'x' and other distinctive components are marked as 'o'. Detail frequency and magnitudes are listed for 'x's and 'o's are listed in Table 4.1 and 4.3, respectively. Combined application of the dithering and the carrier frequency

60
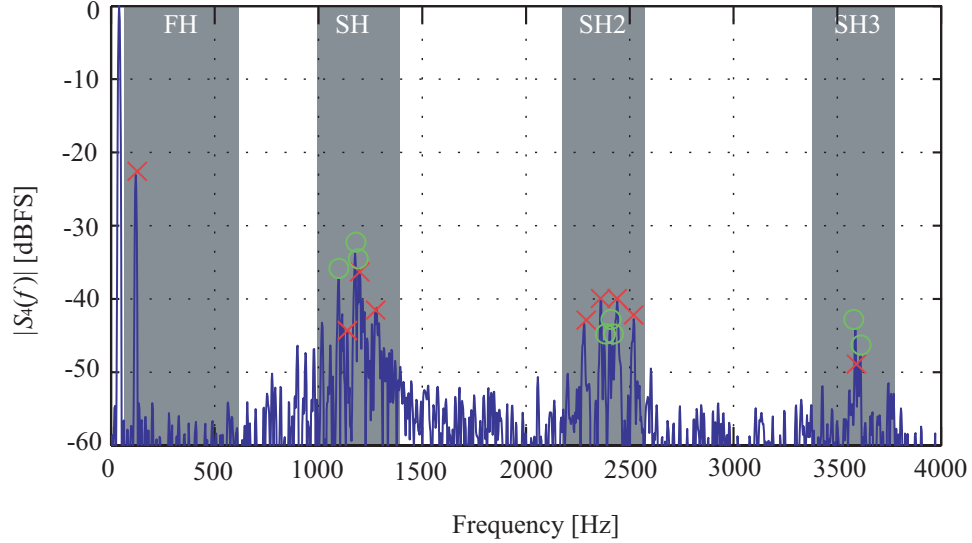
Figure 4.7: Frequency response of the dithered random carrier SPWM

randomization method remarkably reduces harmonic distortions of the mod-
ulated signal. The noise floor, formed by the dithering, is also lowered below
-50 dB at which fundamental frequency related harmonics except the 3rd or-
der harmonic are bounded as shown in the FH region. In the SH region,
the maximum magnitude of the modulated signal appear at 1098 Hz, which
value is -37.22 dB with respect to the fundamental density. Likewise the re-
sult shown in Fig. 4.6, harmonics associated with the carrier frequency in the
SH2 and SH3 regions, are also reduced more than 20 dB compared with the
conventional SPWM spectrum. However, the dithering mitigates harmonics
associated with k in (4.1), the number of dominant harmonics in the SH, SH2,
and SH3 regions are less than those in Fig. 4.6.

Fig. 4.8 shows the spectrum of a dithered sigma-delta modulated sig-
nal where distinctive components are marked as 'x'. Corresponding frequencies
and magnitudes for 'x's are enumerated in Table 4.4. Because (4.1) is devel-

61

Table 4.1: Magnitudes of harmonics of for SPWMs for defined (l,k)

	Frequency [Hz]	Magnitude [dB]				(l,k)
		SPWM	Random Dithered SPWM	Random carrier SPWM	Dithered Random carrier SPWM	
FH	120	-24.1	-23.2	-23.75	-23.08	(0,3)
	200	·	·	-29.6	·	(0,5)
	280	·	·	-43.92	·	(0,7)
	360	-26.01	·	-43.79	·	(0,9)
	440	·	·	-44.32	·	(0,11)
	520	-22.07	·	·	·	(0,13)
	600	-26.56	·	·	·	(0,15)
SH	1040	·	-30.31	·	·	(1,4)
	1120	-10.95	-14.06	-40.44	-44.03	(1,2)
	1200	-6.55	-4.94	-36.93	-36.22	(1,0)
	1280	-6.55	-14.13	-39.13	-41.22	(1,2)
	1360	·	-30.17	·	·	(1,4)
SH2	2200	·	·	-42.6	·	(2,5)
	2280	-13.89	-22.21	-36.7	-43.29	(2,3)
	2360	-16.52	-16.88	-41.23	-39.92	(2,1)
	2440	-18.35	-16.36	·	-40.33	(2,1)
	2520	-14.31	-22.09	-36.77	-42.74	(2,3)
	2600	·	·	-41.32	·	(2,5)
SH3	3440	-15.34	-30.88	·	·	(3,4)
	3520	·	-32.34	·	·	(3,2)
	3600	-18.47	-18.94	·	-48.97	(3,0)
	3680	·	-31.4	·	·	(3,2)
	3760	-16.54	-31.53	·	·	(3,4)

oped from the SPWM process in Chapter 2, integer parameters l and k are not defined for $\Sigma\Delta$M. Thus, the distinctive harmonic tones are explained with respect to the fundamental frequency. The lowest frequency of the distinctive harmonics is 120 Hz which corresponds to the 3rd order harmonic. The

Table 4.2: Magnitudes of harmonics of the carrier frequency randomized SPWM for undefined (l, k)

Frequency [Hz]		Magnitude [dB]	(j,k)	Frequency [Hz]		Magnitude [dB]	(j,k)
SH	1018	-41.89			3453	-43.95	
	1098	-36.35			3748	-43.24	
	1178	-35.42	undefined	SH3	3773	-44.29	undefined
SH3	3348	-43.57			3828	-44.18	
	3428	-42.96			3853	-44.69	

Table 4.3: Magnitudes of harmonics of the dithered random carrier SPWM for undefined (l, k)

Frequency [Hz]		Magnitude [dB]	(j,k)	Frequency [Hz]		Magnitude [dB]	(j,k)
SH	1178	-33.75		SH2	2378	-45.77	
	1098	-37.22			2418	-46.39	
	1193	-35.77	undefined	SH3	3588	-44.24	undefined
SH2	2405	-43.96			3613	-47.79	

Table 4.4: Magnitudes of dithered $\Sigma\Delta$M harmonics

Frequency [Hz]	Magnitude [dB]	Frequency [Hz]	Magnitude [dB]	Frequency [Hz]	Magnitude [dB]
120	-33.36	960	-30.22	1920	-31.85
520	-31.15	1200	-31.54	2000	-35.43
560	-30.58	1345	-31.81	2255	-36.24
600	-29.77	1600	-33.49	2400	-37.49
640	-31.41	1680	-30.71	2800	-36.65
760	-31.78	1760	-30.64	3560	-38.77
800	-25.88	1840	-31.02	3640	-38.95

magnitude of the 3rd order harmonic is -33.86 dB from the fundamental component. Compared with the conventional SPWM spectrum, $\Sigma\Delta$M mitigates the 3rd order harmonic by approximately by 10 dB. Other harmonic tones

63
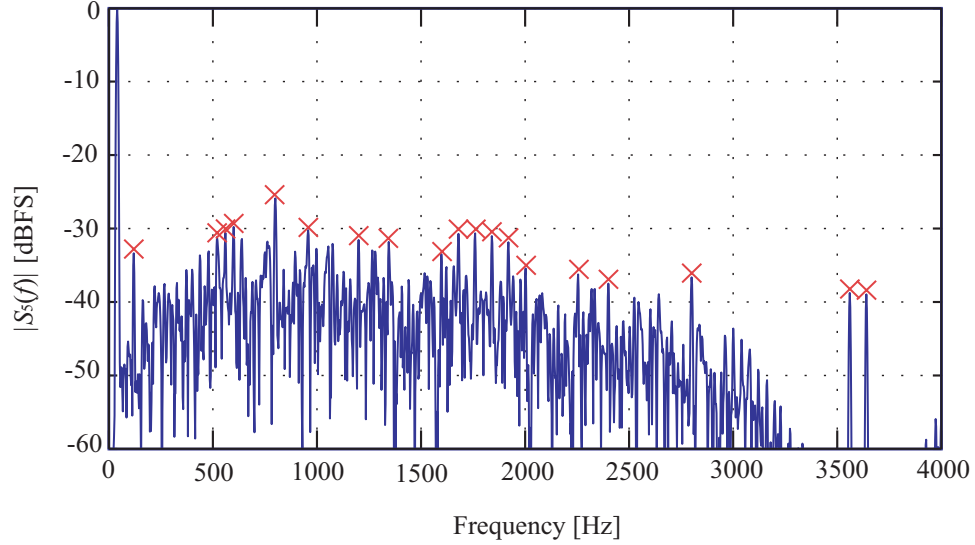
Figure 4.8: Frequency response of the dithered $\Sigma\Delta$M

below 500 Hz are not prominent due to the noise floor. However, the noise floor is not flat over all frequency range but tends to decrease as frequency is close to the fundamental and the sampling frequency, 3.6 kHz because of the noise shaping property of $\Sigma\Delta$M and zero-order holding interpolation. Thus, the dithered $\Sigma\Delta$M provides less noise and harmonics near the fundamental frequency. The maximum harmonic component appears at 800 Hz where the magnitude is -25.88 dB with respect to the fundamental component.

Before the zero-order holder in Fig. 4.3, the spectrum is symmetric about $f_s/2$ and repeats at every f_s where $f_s/2$ corresponds to the carrier frequency in SPWMs. Harmonic tones around $f_s/2$ of 1800 Hz are bounded to -30 dB of the fundamental tone, which is less than in the conventional SPWM by approximately 25 dB. By zero-order holding, the spectrum become asymmetric by the processes described in (4.2)-(4.4). Considering the symmetricity and periodicity before the zero-order holding, we can identify that the fre-
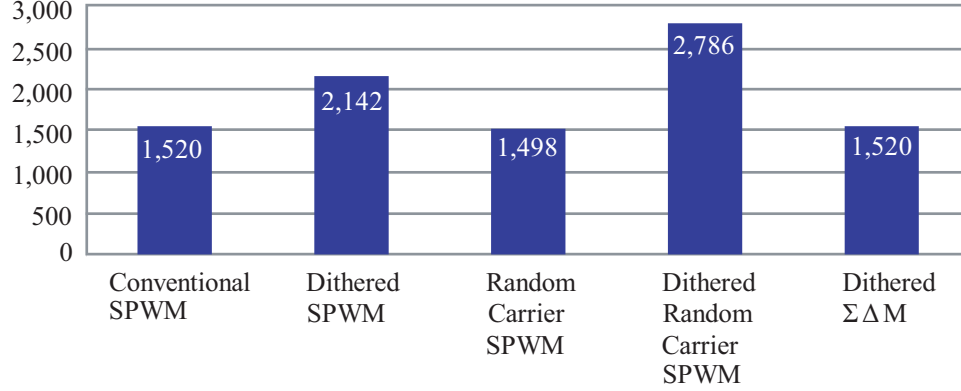
Figure 4.9: The number of switching events per second

quency tones at 3560 Hz and 3640 Hz are mirrored and repeated tones of the fundamental component at 40 Hz, respectively. Compared with the dithered SPWMs shown in Fig. 4.5 and Fig. 4.7, the dithered $\Sigma\Delta$M signal exhibits a higher noise floor level. Although harmonic characteristics of $\Sigma\Delta$M signal are worse in the frequency range from 500 Hz to 1 kHz and from 1.5 kHz to 2 kHz, the advantageous properties of $\Sigma\Delta$M become prominent if the number of switching is investigated.

Fig. 4.9 summarizes the number of switching of each topology. Although direct injection of dither to the switching operation effectively mitigates fundamental harmonics, switching loss might become a serious problem. Meanwhile, dithering the discrete process of the $\Sigma\Delta$M does not severely increase the number of switching because the noise signal is also sampled at the same frequency as the reference signal. The overall characteristics of each PWM topology are summarized in Table 4.5.

Table 4.5: Summary of PWM Characteristics

Topologies	Descriptions
Conventional SPWM	· Harmonic frequencies are linear combinations of the fundamental and carrier frequency
Dithered SPWM	· Fundamental-frequency harmonics decrease · Noise floor increases(-50dB) · Switching-frequency harmonics do not decrease · Switching loss increases
Random Carrier SPWM	· Switching-frequency harmonics decrease · Harmful fundamental-frequency harmonics still exist · Switching loss does not increase
Dithered Random Carrier SPWM	· Both fundamental- and switching-frequency harmonics decrease · Noise floor increases(-60dB) · Switching loss severely increases
$\Sigma\Delta$M	· Harmonics in wide range of frequency decrease · Lower noise floor near the fundamental and sampling frequency · Switch loss does not increase

4.4 Conclusion

Harmonic characteristics of the conventional, dithered, randomized carrier SPWMs, and the dithered $\Sigma\Delta$M signals were compared over the frequency range up to 4 kHz. The dithering method, based on additive noise at the comparator, was effective in reducing the fundamental frequency; however, the increased number of the switching is inevitably disadvantageous. The carrier frequency randomization method was effective in reducing the harmonics associated with the carrier frequency without increasing the number of switching.

Compared with the conventional SPWM and the randomized-carrier SPWM, which operate with similar number of switching per second, the $\Sigma\Delta$M signal demonstrated lower harmonics near the fundamental frequency especially the 3rd order harmonic frequency. For the overall frequency range, the $\Sigma\Delta$M spectrum was bounded below -30 dB with respect to the magnitude at the the fundamental frequency. Due to the noise shaping property of dithered $\Sigma\Delta$, noise floor is reduced near the fundamental frequency. In the high frequency range close to the sampling frequency, the $\Sigma\Delta$M spectrum also exhibited a reduced noise floor because of zero-order holding interpolation. Besides the spectral characteristics, the strictly defined minimum pulse-width and the simple hardware structure are advantageous properties of the $\Sigma\Delta$ modulator.

Chapter 5

Validation of dithered PWMs in mitigating harmonics and interharmonics

This chapter describes the experimental setup for dithered PWM inverters and demonstrates those harmonic and interharmonic characteristics. The experimental setup is described in two parts: the description for a three phase inverter module and its gating signal implementation, and corresponding hardware configurations to investigate harmonics and interharmonics. With the hardware experiment, advantageous properties of dithering methods, described in Chapter 3 and 4, are validated, which demonstrate the following: (i) the effectiveness of dithered SPWM in mitigating fundamental frequency harmonics and associated interharmonics, (ii) mitigation of carrier frequency and its harmonics of carrier frequency randomized SPWM , and (iii) mitigated harmonics and advantageous noise-shaping property of the dithered $\Sigma\Delta$M.

5.1 Introduction

In previous chapters, dithering and carrier frequency randomization techniques were described as mitigation methods of PWM-associated harmonics and interharmonics. The mitigated harmonics at the PWM inverter were evaluated on the simulation platform using PSCAD/EMTDC and MATLAB. In Chapter 3, the mitigation effects of dithered SPWM on harmonics at the

loadside and interharmonics at the source side of VSI-ASD system were described. In Chapter 4, the effect of dithering methods were focused on the output harmonics of PWM inverter. As an alternative PWM topology, dithered $\Sigma\Delta$M method was introduced. Its harmonic performance and the number of switching events were evaluated compared with those of dithered SPWM, carrier frequency randomized SPWM.

Continuing previous chapters, we validate the effect of dithered PWM methods on harmonics and interharmonics performing hardware experiments in this chapter. The experiments are performed for dithered PWM inverters to validated harmonic characteristics and extended to a scaled-down version of an ASD system to investigate interharmonics. In following sections, experimental setup, description for the PWM signal generation, and experimental results are represented.

5.2   Experimental setup

5.2.1   Three phase inverter module and PWM gating signals

As a three-phase IGBT inverter bridge, we utilized Fairchild's FSBB30 CH60F inverter module shown in Fig. 5.1(a). The inverter module is designed for high power density (size vs. power) up to 30 A/600 V and operates with input signals from 3.3 V to 5 V. The internal configuration of the inverter module is shown in Fig. 5.1(b), where six IGBT-diode pairs and drivers compose three-phase inverter bridge. The characters, 'U', 'V', and 'W' correspond to conventional three phase indices 'a', 'b', and 'c'. Through the input ports 'IN$_{(\cdot\text{H})}$' and 'IN$_{(\cdot\text{L})}$', PWM signals controlling the upper and lower parts of the inverter bridge are injected. The injected PWM signals are regulated at 3.3 V

by the drivers before being connected to the gates of the internal IGBTs whose threshold voltages to be turned on and off are 2.8 V and 0.8 V, respectively. Controlled by the regulated signals, the DC voltage connected to 'P' and 'N$_{(\cdot)}$' is converted into three-phase PWM voltages at 'U', 'V', and 'W' ports. The input and output ports described above are connected to external signal and power sources through the application board shown in Fig. 5.2.

PWM signals to drive the inverter module are generated in a LabVIEW platform. In principle, an SPWM signal is produced from the comparison of a sinusoidal reference signal and a triangular waveform. Based on the results in Chapter 4, we implement the dithered SPWM to mitigate harmonic tones associated with the fundamental frequency, and carrier frequency randomized SPWM to spread carrier-frequency harmonics over a wide range of frequency. The SPWM configuration for both randomization methods and the corresponding LabVIEW diagram are illustrated in Figs. 5.3 and 5.4, respectively.

Unlike PWM signals implemented in a simulation model, the complementary set of PWM gating signals, S_H and S_L in Fig. 5.3, has to be separated by dead time. Otherwise, S_H and S_L can overlap during each transition, which can cause shoot-through or short-circuit faults [39]. In our experiment, we employ an up-sampling and threshold method to isolate S_H and S_L by dead time as shown in Fig. 5.5(a). A transition of S_H and S_L is illustrated as solid line, where each dot on the line represents a sample generated in the discrete-time simulation. The samples corresponding to S_H and S_L do not overlap in the discrete time. However, when the waveform is interpolated for the continuous-time interface, the solid lines indicating S_H and S_L overlap during each transition. To isolate these two waveforms, we perform up-sampling to
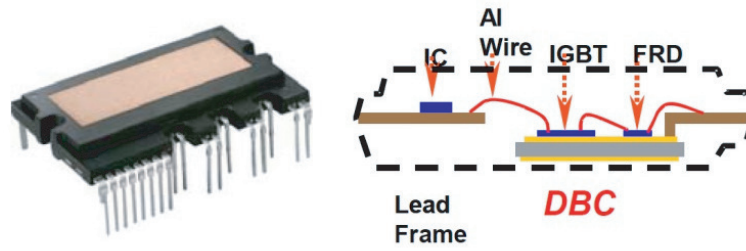
(a)
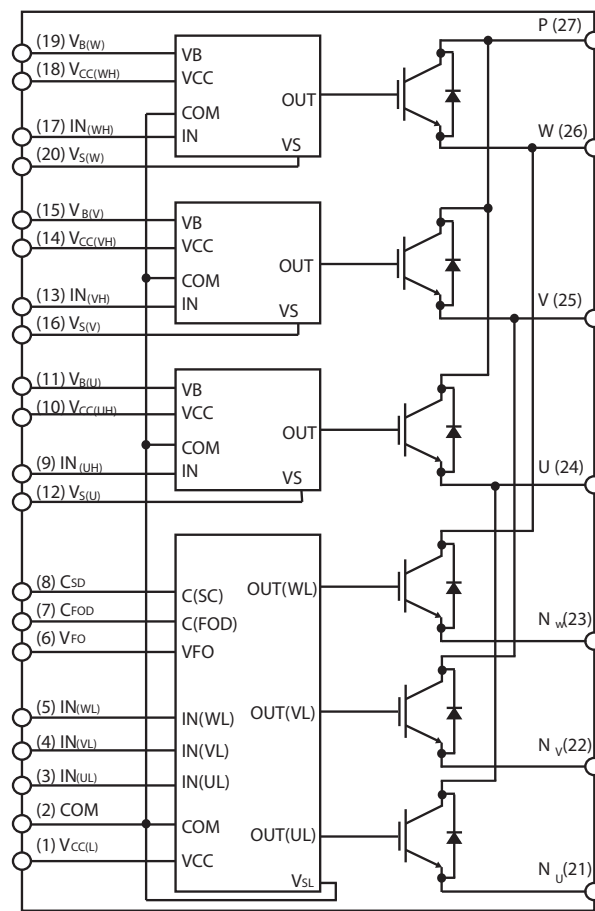
(b)

Figure 5.1: Fairchild FSBB30CH60F inverter module (a) physical feature (b) internal structure

71
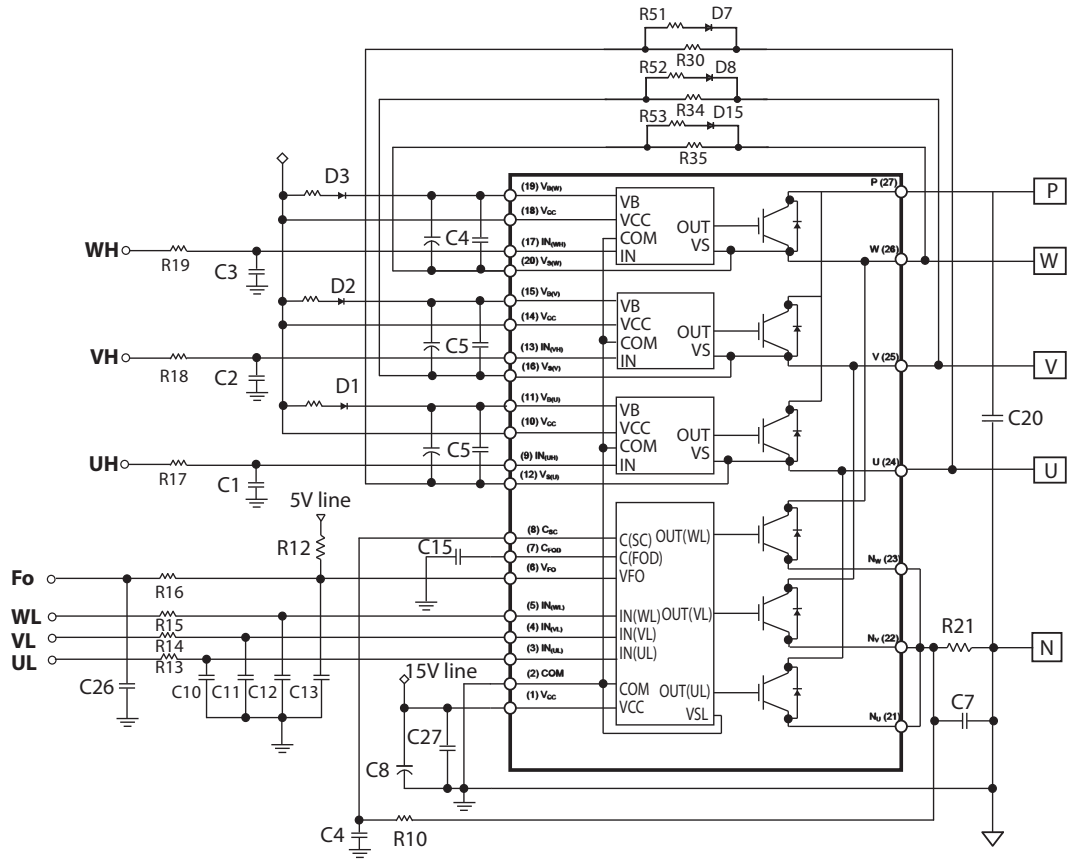
(a)
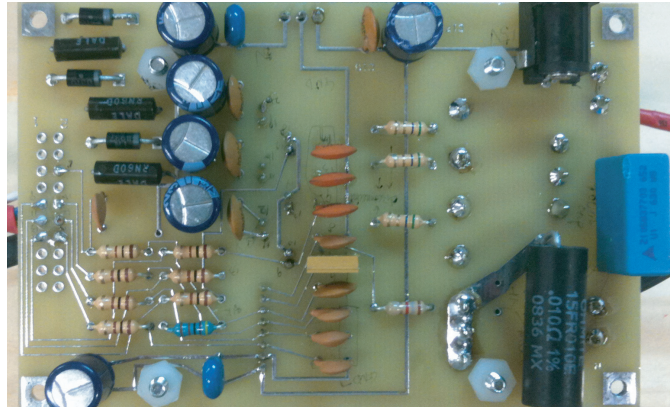
(b)

Figure 5.2: Application board for FSBB30CH60F (a) schematic diagram [3](b) hardware implemetation
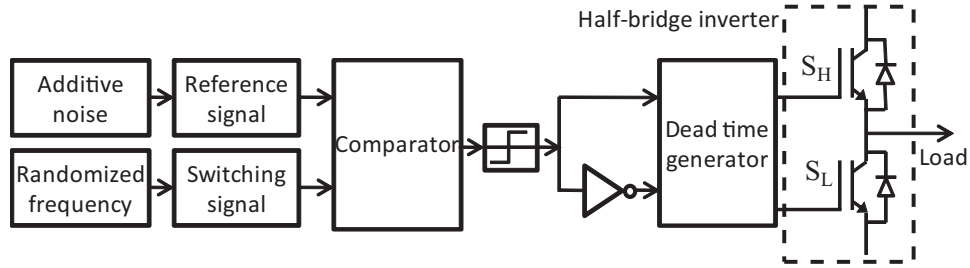
Figure 5.3: SPWM configuration for LabVIEW implementation
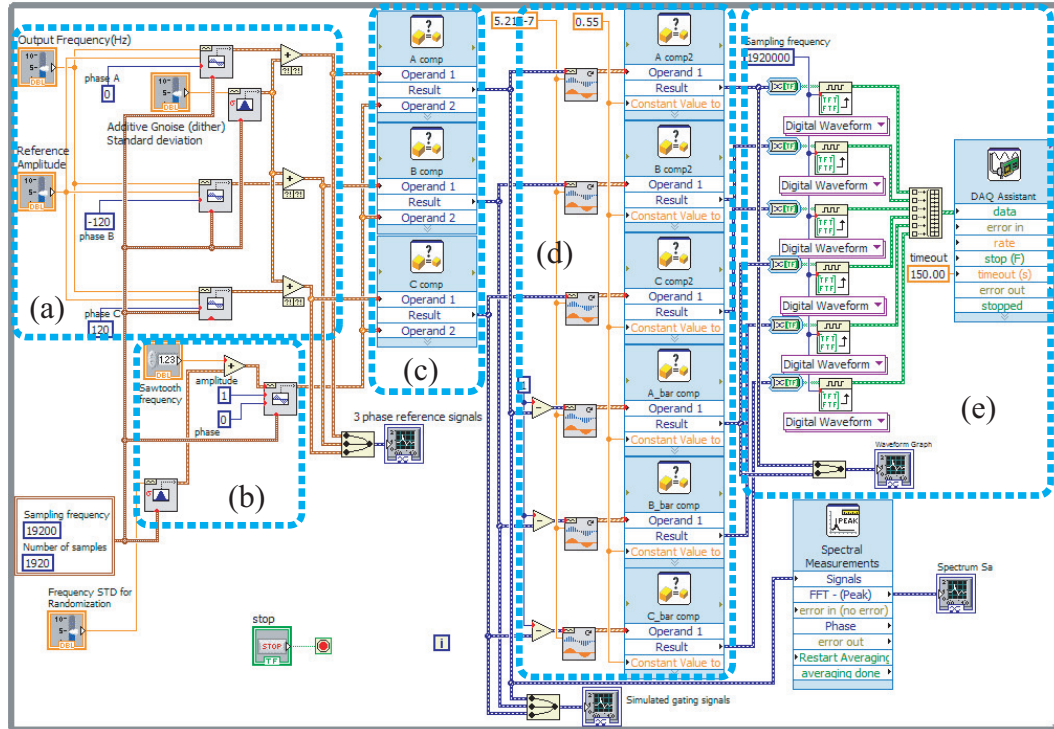
Figure 5.4: SPWM signal generating model in LabVIEW: (a) reference signal and dithering part (b) switching signal and frequency randomization part (c) comparator (d) dead time generator (e) signal exporting part.
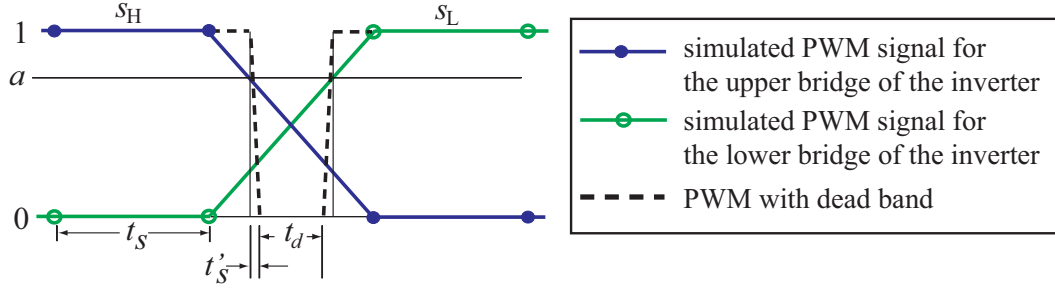
(a)
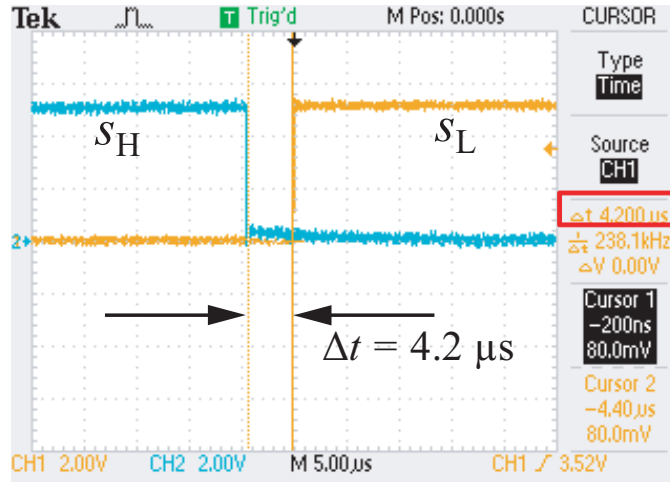
(b)

Figure 5.5: Dead band generation for PWM signals in a LabVIEW platform: (a) configuration (b) generated dead band

the sampled waveforms of S_H and S_L in first. Then, the resolution of each transition of S_H and S_L are increased. Next, we compare up-sampled signals to the threshold value, a. Compared with the threshold value, up-sampled signals are converted into either 'high' or 'low' values as represented dotted line in Fig. 5.5(a). Then, the up-sampled waveforms of S_H and S_L are separated during their transitions. The separate duration in each transition of S_H and S_L denotes dead time. The relationship between the dead time and

74

corresponding threshold value can be represented as follows:

$$t_d = (2a - 1)t_s - 2t'_s \tag{5.1}$$

$$a = \frac{t_d + 2t'_s}{2t_s} + 0.5 \tag{5.2}$$

where t_d is dead time, t_s, and t'_s are sampling periods before and after up-sampling, and a is the threshold level. In this experiment, the sampling periods, t_s, t'_s and the desired dead time, t_d, are 52.083 μs, 0.521 μs, and 4 μs, respectively. From (5.2), the corresponding value of a is 0.5484. However, the sampling period is reduced by 0.01 from 52.083 μs to 0.521 μs, 100 samples are generated between each pair of existing samples, which denotes that the minimum resolution of the threshold value, a, is 0.01. Thus, we adjust the threshold value, a, to 0.55, which corresponds to t_d of 4.16 μs in (5.2). In the actual implementation, the dead time for the threshold of 0.55 is 4.2 μs, as shown in Fig. 5.5(b).

Figs. 5.6 and 5.7 illustrate $\Sigma\Delta$M configuration for hardware experiment and the corresponding block diagram in LabVIEW simulation. Initially, we generate $\Sigma\Delta$M bitstream using Matlab at the desired sampling frequency, f_s. Then, each bitstream is interpolated by the zero-order holding block. Corresponding sampling frequency after zero-order holding is multiplied by the number of samples inserted between each pair of initial bits. The interpolated bitstream is exported to the buffers in LabVIEW simulation model. The buffered values composes a unit frame of a waveform. Then, each waveform is decomposed into upper and lower gating signals. Both upper and lower gating signals are separated by dead time. To generate dead time in $\Sigma\Delta$M signals, we also apply the up-sampling and threshold method used for SPWM signal generation.

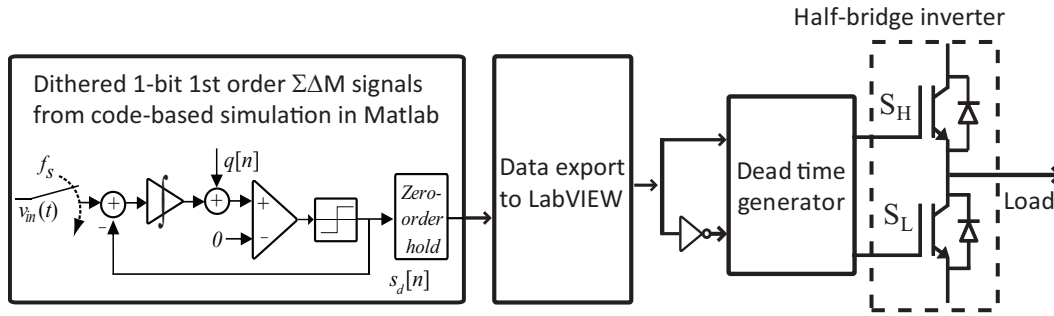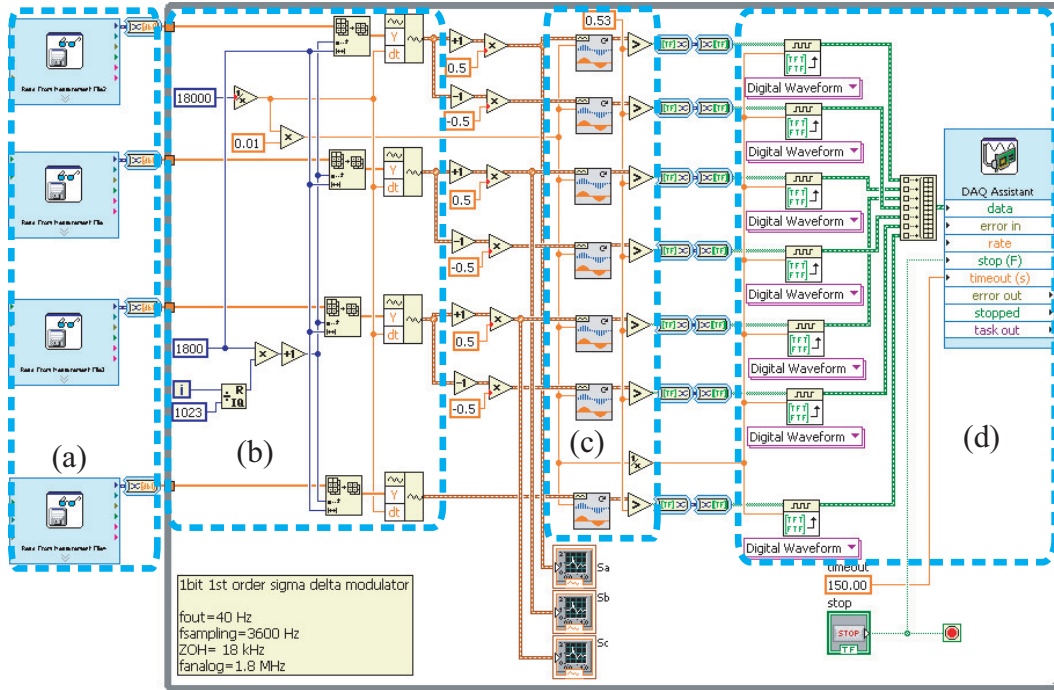Figure 5.6: $\Sigma\Delta$M configuration for hardware experiment

Figure 5.7: $\Sigma\Delta$M signal generating model in LabVIEW: (a) blocks for importing data from Matlab simulation (b) buffer assignment blocks(c) dead time generator (e) signal exporting part

The PWM signals generated from LabVIEW simulation are displayed on LabVIEW front panel illustrated in Fig. 5.8. Once the PWM signals are verified on the front panel, they are exported as voltage signals through data acquisition modules, NI PCI-6115 and NI BNC-2110, shown in Figs. 5.9(a) and (b). NI PCI-6115 data acquisition board can export simulated samples up to 10 MSa/s ratio. In our PWM simulations, the maximum sampling frequency is less than 2 MHz even if up-sampling and threshold method is applied for dead time generation. Thus, NI PCI-6115 provides sufficient resolution to represent the simulated PWM signals in voltage waveforms. NI BNC-2110 connector provides ten output ports: two analog and eight digital ports. Because six gating waveforms are required to drive the three-phase inverter, we export PWM signals through the digital ports. The digital output ports of NI BNC-2110 provide 0 V and 5 V waveforms to represent digitally 'low' and 'high' bits, respectively. Because FSBB60CH30F inverter module can be driven by either 3.3 V or 5 V turn-on signals, the output signals from the digital ports of NI BNC-2110 are adequate to drive in FSBB60CH30F.

5.2.2 Hardware configuration to investigate harmonics and inter-harmonics

To investigate PWM-associated harmonics at the output of a PWM inverter, we connected DC voltage source at the inverter input. The overall experimental configuration of PWM inverter is demonstrated in Fig.5.10. As a three phase inverter bridge, FSBB30CH60F module described in the previous section is utilized where gating signals are generated in LabVIEW platform and exported through a data acquisition device. The DC voltage source provides 15 V_{dc} to the input of the inverter to supply 40 Hz three-phase AC power to

77
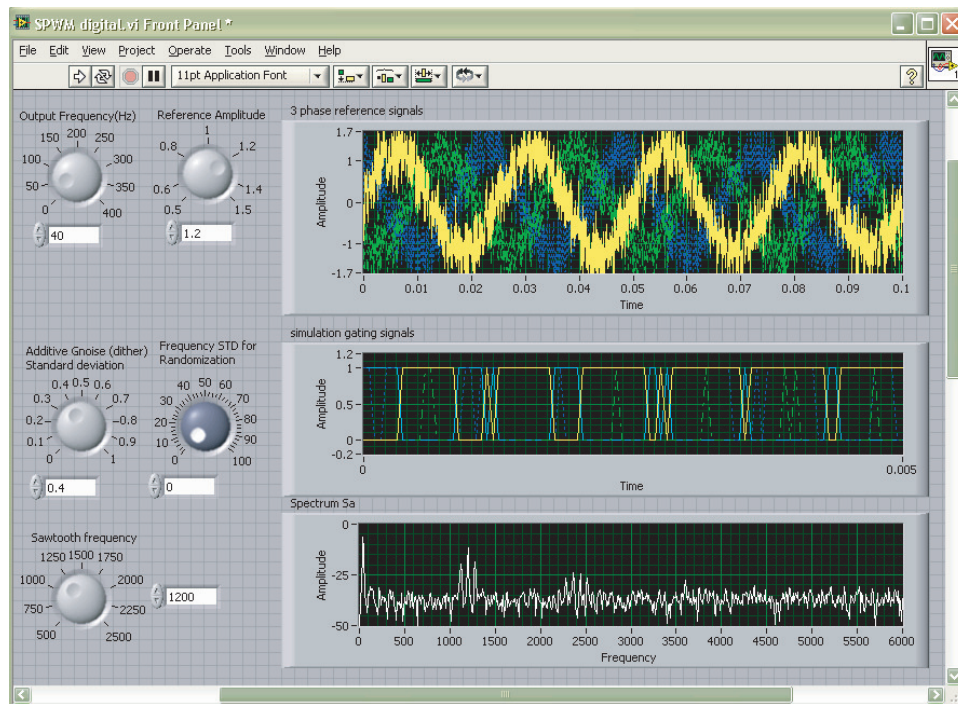
Figure 5.8: A snapshot of LabVIEW front panel for PWM signal generation
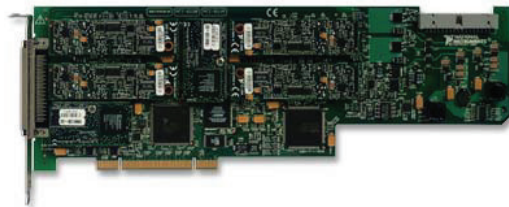
(a)

(b)

Figure 5.9: Devices for data acquisition system (a) NI PCI-6115 data acquisition board (b) NI BNC-2110 data acquisition I/O connector

78
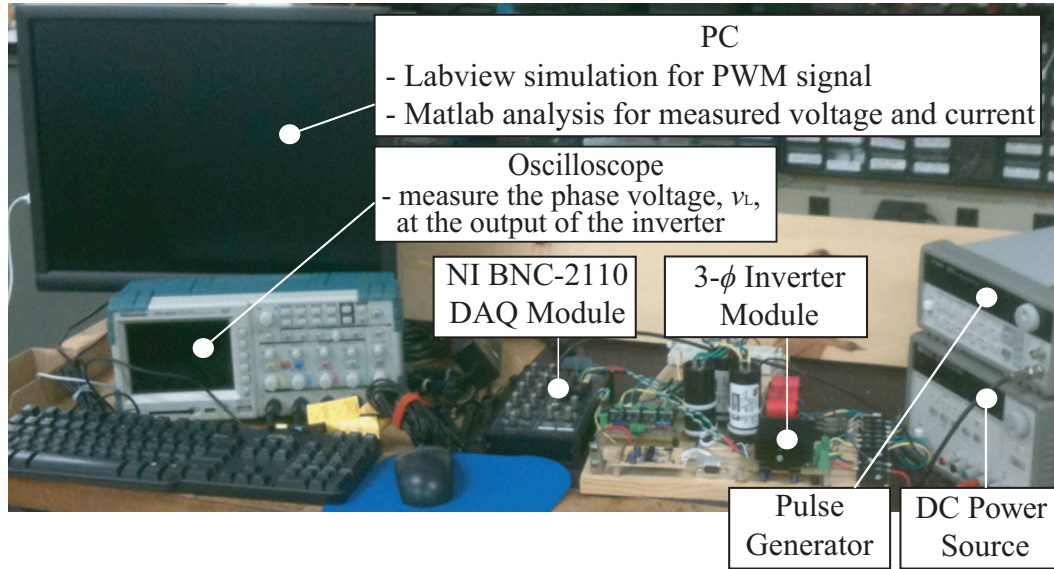
Figure 5.10: Experimental configuration for inverter harmonics

a grounded-wye resistive load. The resistance of the load is 25 Ω/phase and power rating value is 75 W. The phase voltage is measured at the resistive load and analyzed using Matlab program.

To investigate PWM-associated interharmonics at the source-side of a ASD system, we connected the inverter to the AC supply system. The experimental configuration is illustrated in Fig. 5.11. In the experiment, a 60 Hz/240 V three-phase voltage is scaled down by a transformer converted into ~30 V_{dc} through a six-pulse rectifier. The three-phase inverter module, FSBB30CH60F, is driven by PWM signals generated in LabVIEW platform and converts the rectified DC voltage into three-phase PWM voltages whose fundamental frequency is 13 Hz. When the inverter switch is turned on, current flows from the DC link to output load through the inverter. Because turn-on and -off timing of the switches are determined by the PWM gating signals, the current waveform at DC link is affected by PWM signal so that PWM-

associated harmonics appear at the DC link. The harmonic waveforms at the DC link can flow to the source-side when the diodes in the six-pulse rectifier are turned on. Consequently, the power supply is also affected by the PWM harmonics which appear as interharmonics coupled with source-side frequency components [21]. To investigate the current interharmonics at the source-side, we measure current flow using a current sensor module and display frequency response using Matlab program.

For a balanced three phase power source, harmonics associated with a six-pulse rectifier can be evaluated using the Fourier series representation [43]. Generally, a six-pulse rectifier produces 6th harmonics to the DC-side and $(6n \pm 1)$th harmonics of f_s (=60 Hz) at the AC-side. However, in practical experiment, the unbalanced three-phase source can causes harmonics other than the 6th order as well. Fig 5.12 illustrates three phase voltage waveform used in our experiment and corresponding DC voltages. As shown in the voltage waveforms, each voltage is equally distributed in phase but not in amplitude. The difference of amplitudes between the phase voltages causes different magnitude of ripples in the DC voltage, thus harmonic frequencies except multiples of the 6th order can appear at the DC link. Furthermore, the positive and negative dc voltages, V_{dc}^+ and V_{dc}^-, have ripples whose frequencies are triple of the f_s. Because those two voltages, V_{dc}^+ and V_{dc}^-, are separated by grounded node, as shown in Fig. 5.11, the inverter output voltage can be affected by the 3rd order harmonic of f_s, unless the operation of the inverter is perfectly symmetrical.

The spectrum of DC-side ripple is shown in Fig 5.13, where the spectrum is normalized with respect to the 6th order component (360 Hz) and plotted in dBFS. The 2nd and 4th order harmonics appear as a result of un-
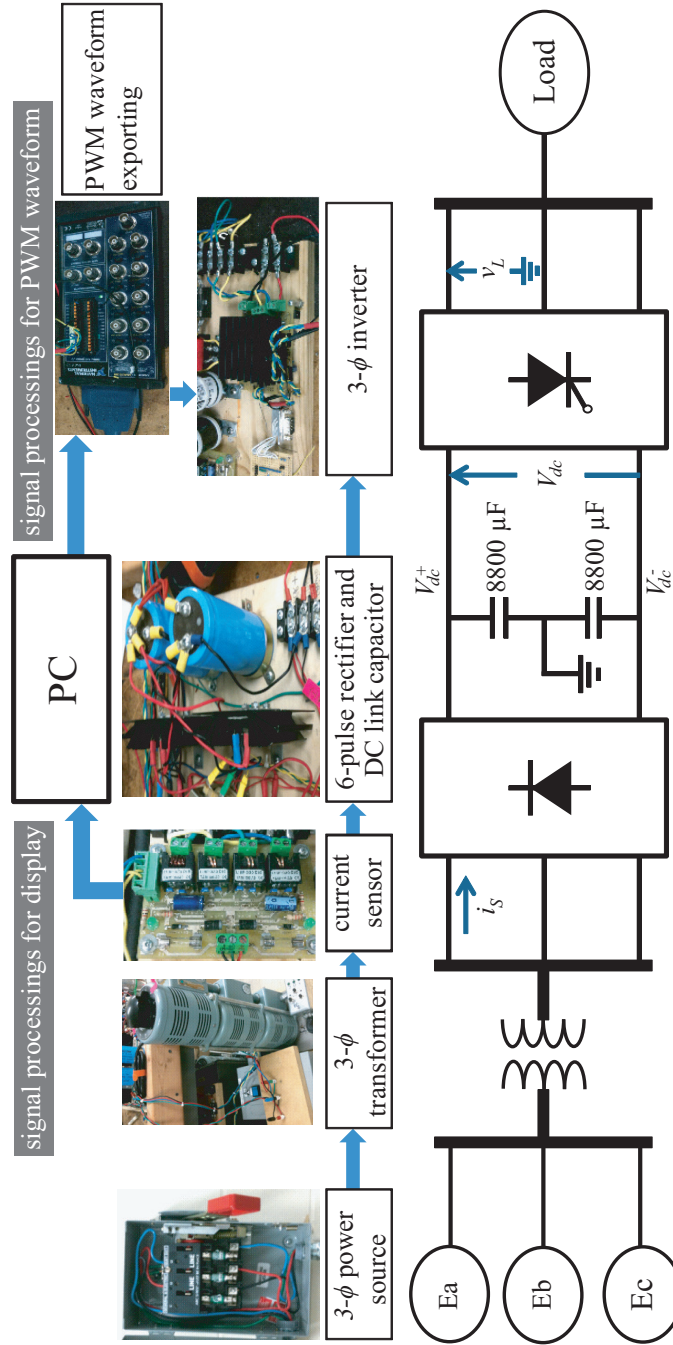
80

Figure 5.11: Experimental set up for ASD interharmonics
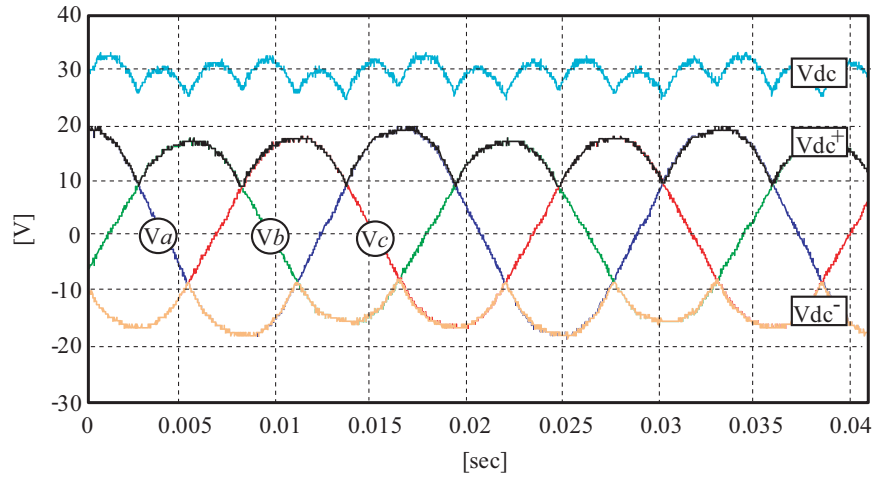
Figure 5.12: Three phase voltage source and rectified DC voltages
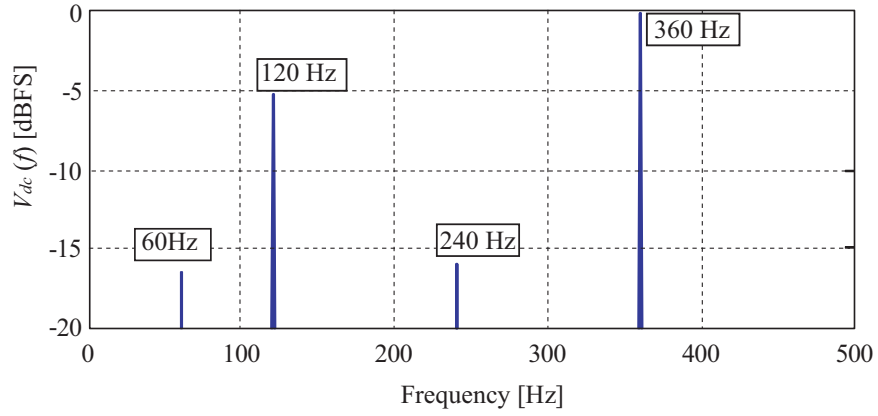
Figure 5.13: Three phase source and rectified voltages

balanced three phase source. These unexpected harmonics also affect source side harmonics so that harmonic frequencies other than $(6n \pm 1) \cdot f_s$ can appear at the source side.

5.3 Analysis of experimental result

5.3.1 Investigation on harmonics associated with PWM

This section describes voltage harmonics of the PWM inverter whose experimental configuration is illustrated in Fig. 5.10. Frequency responses of the phase voltage, v_L, at the load are illustrated in Figs. 5.14-5.17 for conventional SPWM, dithered SPWM, carrier frequency randomized SPWM, and dithered $\Sigma\Delta$M inverters. The frequency responses are plotted over the frequency range from 0 to 4 kHz to display harmonics associated with both fundamental and carrier frequencies where the output fundamental frequency, f_L, is 40 Hz and SPWM carrier frequency is 1.2 kHz. The sampling frequency, f_s, of $\Sigma\Delta$M is 3.6 kHz. The vertical axis denotes dB full scale (dBFS), normalized with respect to the fundamental frequency of 40 Hz.

Fig. 5.14 illustrates frequency response of v_L for the conventional SPWM inverter. Recalling (2.15) in Chapter 2, the feasible harmonic frequencies at the output side of a PWM inverter can be represented as follows:

$$
\begin{aligned}
f_L^h &= |l \cdot m_f \pm k| \cdot f_L \\
&= |l \cdot 30 \pm k| \cdot 40
\end{aligned}
\tag{5.3}
$$

where f_L^h and f_L denote harmonic and fundamental frequencies at the output of a PWM inverter, and parameters l and k are integers. Harmonic frequencies shown in Fig. 5.14 are coincident with (5.3), which indicates that integer set of (l, k) can represent practical harmonic frequencies.

When the dithering is applied to the reference signal of the SPWM inverter, harmonic characteristics of v_L are as shown in Fig. 5.15. Compared with Fig. 5.14, harmonic tones associated with k in (5.3) are reduced by the dithering except when k is 3. However, the switching frequency 1.2 kHz and its

Figure 5.14: Frequency response of v_L for the conventional SPWM inverter
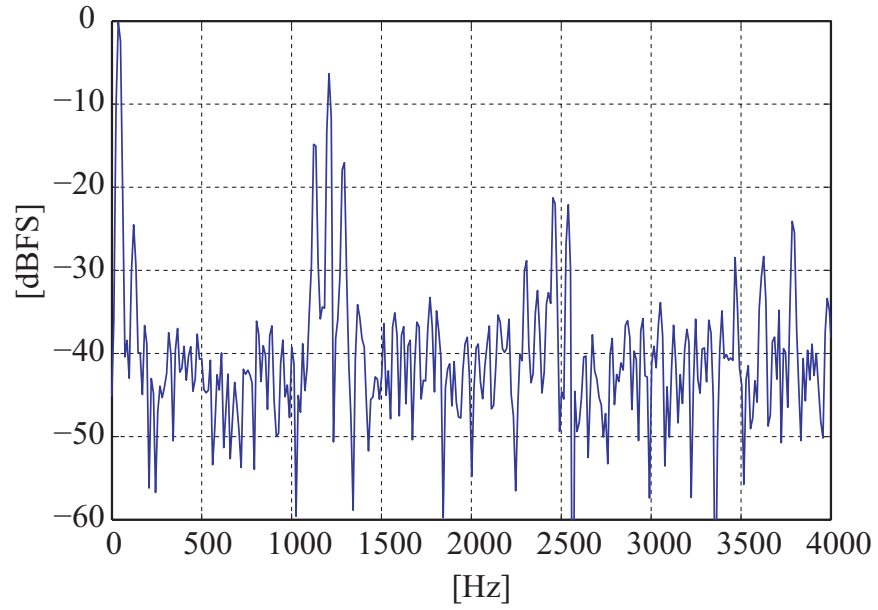
Figure 5.15: Frequency response of v_L for the dithered SPWM inverter
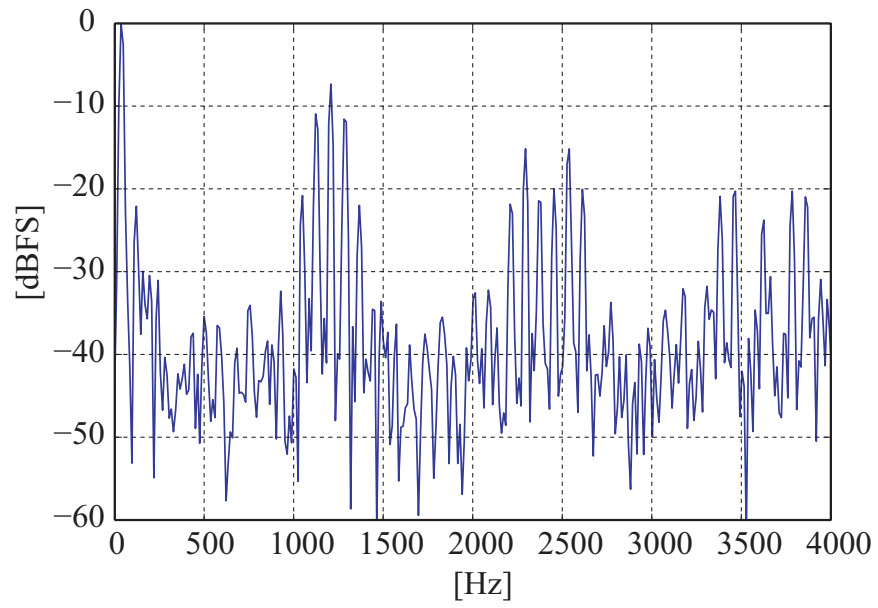
84

harmonics are not noticeably affected by the dithering but they still appear as distinct tones. Since the index, k, indicates the order of harmonics associated with the fundamental frequency, the dithering reduces harmonics at multiples of 40 Hz from the 0 Hz, 1.2 kHz, and 2.4 kHz.

Fig. 5.16 demonstrates frequency response of v_L when the switching frequency is randomized with dithering on the reference signal. Compared with Fig. 5.14, harmonic tones below 500 Hz are not affected by the switching frequency randomization while the switching frequency is reduced approximately 10dB. Harmonics of switching frequencies around 2.4 kHz and 3.6 kHz are also decreased approximately by 10dB. Meanwhile, frequency responses around the switching frequency and its harmonics, distinct tones are spread out to fill the intermediate frequency region, which appears broad-bandwidth tones. Compared with Figs. 5.14 and 5.15, the switching frequency randomization method does not affect the fundamental frequency harmonics but effectively mitigates the level of switching tones at the expense of increased bandwidth around switching frequency and its harmonics.

Fig. 5.17 represents frequency response of v_L when the dithered $\Sigma\Delta$M is applied to the inverter. The advantageous noise shaping property of $\Sigma\Delta$M is also observed in the result of this practical experiment. As frequency is close to the fundamental frequency, the noise floor caused by the dithering is decreased. Unlike conventional $\Sigma\Delta$M spectrum which shows higher noise floor in higher frequency [42], our result demonstrates decreasing noise floor as frequency is close to the sampling frequency, 3600 Hz. Because we interpolate the $\Sigma\Delta$M signal by the zero-order holding method, the noise shaping property near the fundamental frequency repeats at every multiples of the sampling frequency. This observation is also coincident with the simulation result in Chapter 4.
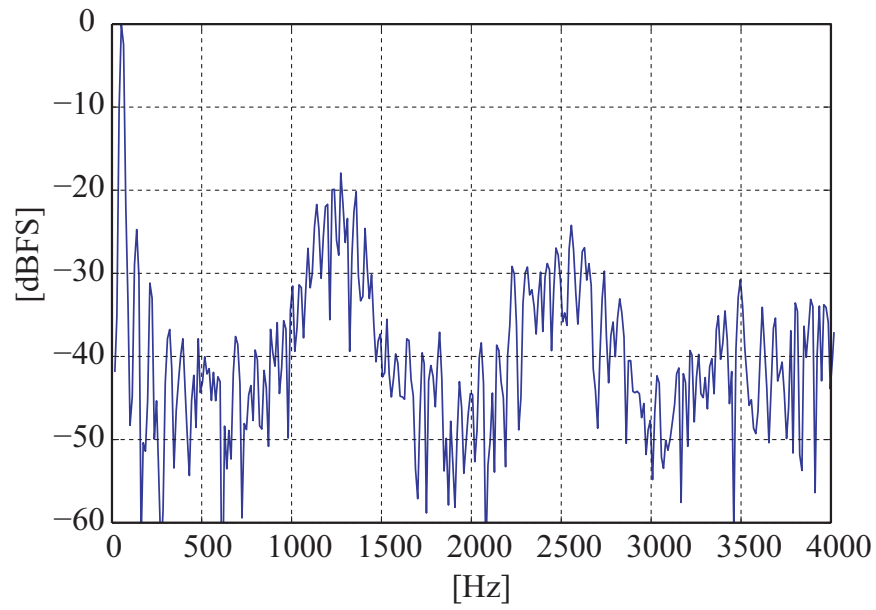
Figure 5.16: Frequency response of v_L for the carrier frequency randomized SPWM inverter
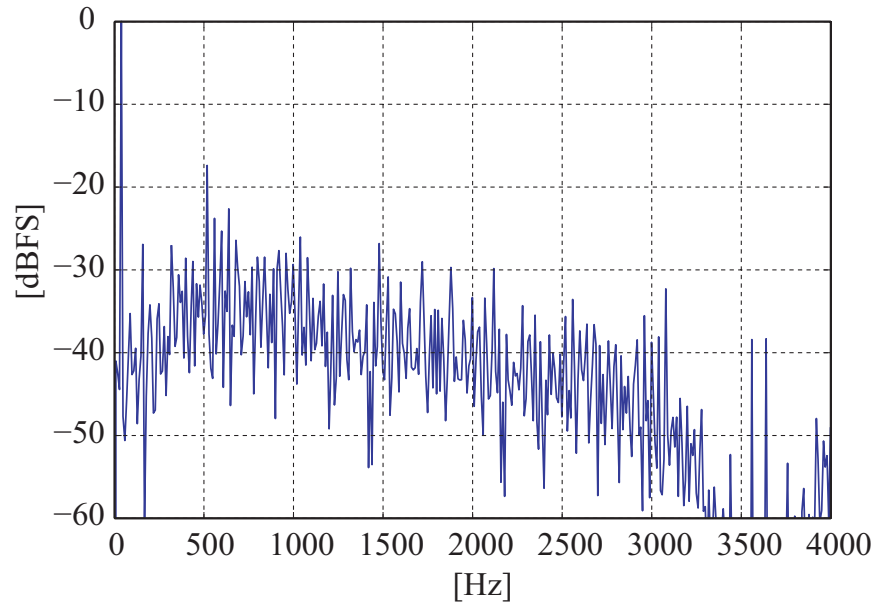
Figure 5.17: Frequency response of v_L for the dithered $\Sigma\Delta$M inverter

Meanwhile, the magnitude of harmonic tones are increased compared with the simulation result especially at 520 Hz. However, the magnitude at 520 Hz is -17.4 dB, which is less than the maximum harmonic component in Fig. 5.14 approximately by 10 dB.

5.3.2 Investigation on interharmonics associated with PWM

For described PWM methods in the previous section, frequency responses of the phase current, i_s (see Fig. 5.11), at the source-side of the ASD experiment are shown in Figs. 5.18-5.21. The frequency responses are displayed over the frequency range from 0 to 100 Hz for interharmonic investigation around the source-side fundamental frequency, f_s. The vertical axis denotes dBFS normalized with respect to the source-side fundamental frequency of 60 Hz. The fundamental frequency, f_L, at the load-side is 13 Hz.

Fig. 5.18 illustrates the frequency response of i_s when the conventional SPWM is connected to the three-phase power source, f_L and its 3rd order harmonic frequency appear as interharmonics at the source side at 21 Hz, 47 Hz, 73 Hz, and 99 Hz. The corresponding magnitudes of interharmonics are -45.9 dB, -30.8 dB, -32.3 dB, and -44.5 dB of the fundamental component, respectively.

When the dithering method is applied to the reference signal of the PWM inverter, the current spectrum at the source side is illustrated in Fig. 5.19. Compared with the current spectrum in Fig. 5.18, the interharmonics close to the fundamental frequency are effectively reduced by the dithering. The amounts of mitigation from Fig. 5.18 are 4.6 dB, 7.1 dB, 6.6 dB, and 5.0 dB at 21 Hz, 47 Hz, 73 Hz, and 99 Hz, respectively.

87
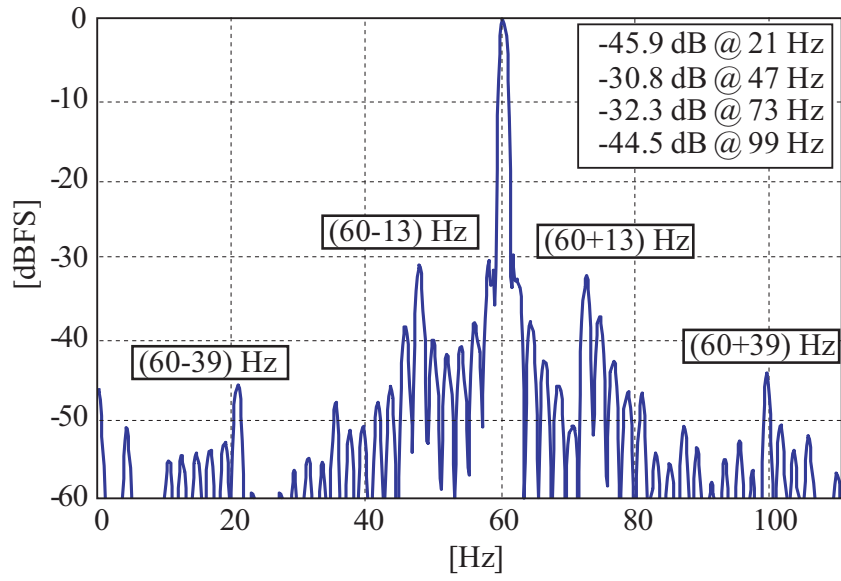
Figure 5.18: Frequency response of source-side current, i_S, for the conventional SPWM
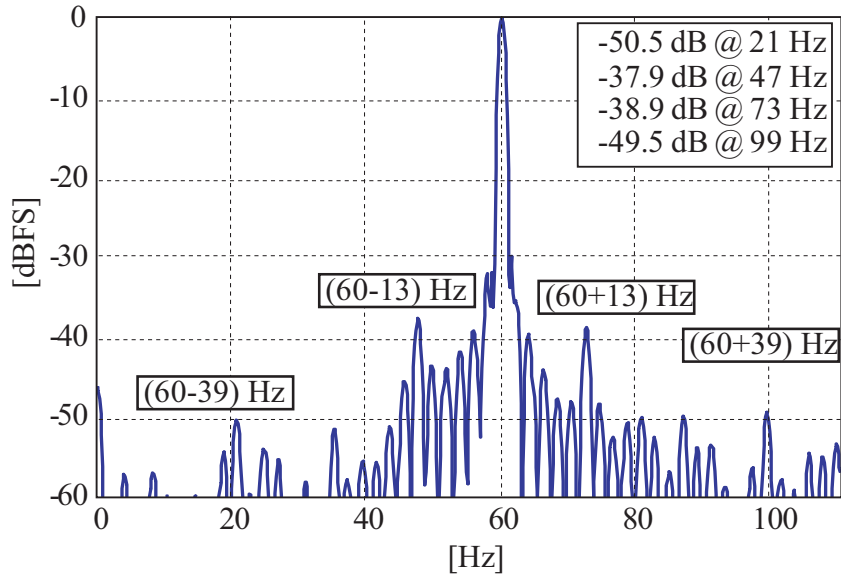
Figure 5.19: Frequency response of source-side current, i_S, for the dithered SPWM
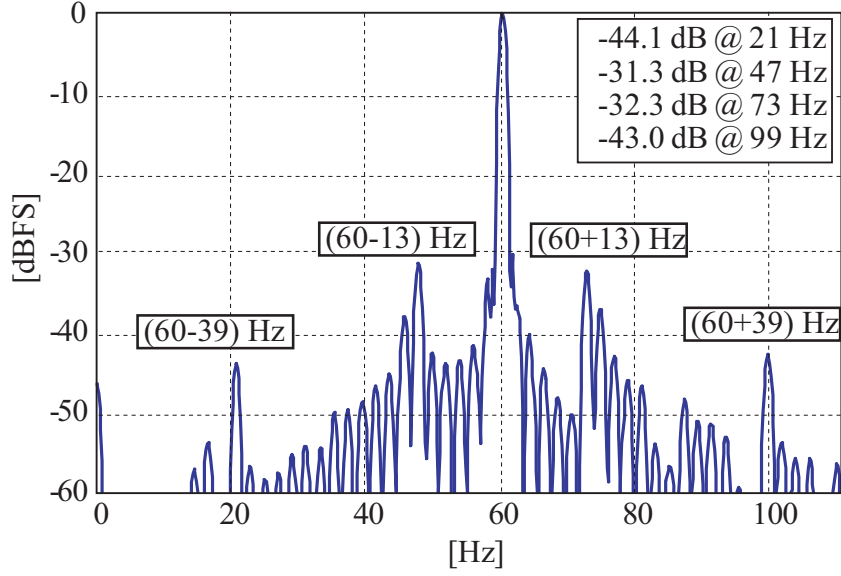
Figure 5.20: Frequency response of source-side current, i_S, for the carrier frequency randomized SPWM

Meanwhile, the spectrum of i_s for the carrier frequency randomized PWM inverter does not improve near the fundamental frequency, f_s, as shown in Fig. 5.20. Recalling the effects of dithering and the carrier frequency randomizing methods on the harmonics at the load side, the dithering method mitigates low frequency harmonics associated with the fundamental frequency, f_L, while the carrier frequency reduces high frequency harmonics associated with the switching frequency.

Fig. 5.21 illustrates the spectrum of i_s when $\Sigma\Delta$M inverter is applied to the ASD model. All interharmonics associated with output frequencies are reduced to below -40 dB with respect to the fundamental frequency. Compared with Fig. 5.18, interharmonics at (60 ± 13) Hz are noticeably reduced by more than 10 dB. Furthermore, magnitudes of frequency components at (60 ± 39) Hz are -57 dB of the fundamental frequency, which is less than the noise floor

89

-57.3 dB @ 21 Hz
-44.9 dB @ 47 Hz
-42.4 dB @ 73 Hz
-57.0 dB @ 99 Hz

(60-13) Hz

(60+13) Hz

(60-39) Hz

(60+39) Hz
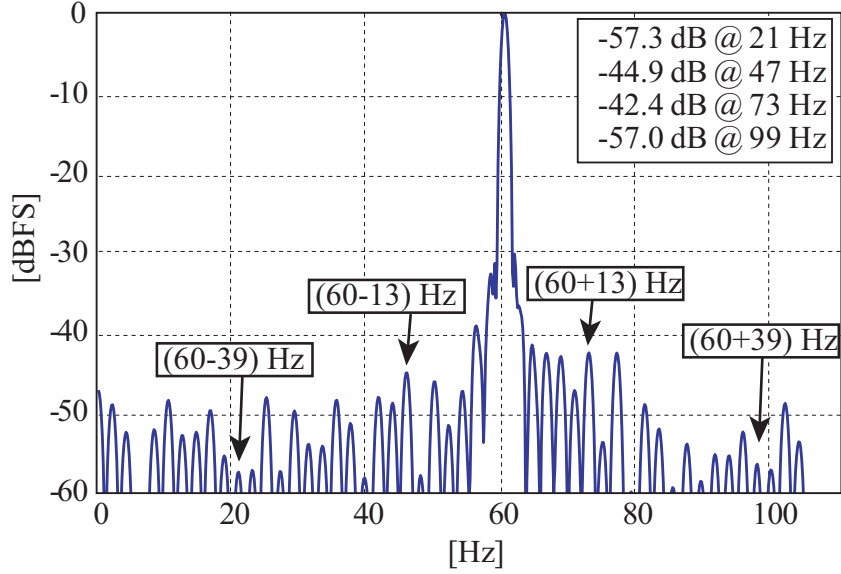
Figure 5.21: Frequency response of source-side current, i_S, for the dithered $\Sigma\Delta M$

formed around -50 dB.

5.4 Conclusion

In this chapter, harmonic/interharmonic characteristics of the conventional, dithered, carrier frequency randomized SPWMs, and dithered $\Sigma\Delta M$ inverters have been investigated by performing hardware experiments. In the experimental results, we observed the consistent spectral characteristics of the PWM inverters with those in the simulation results. Recalling the result in the previous chapters, frequency responses of conventional SPWMs in the simulation and the hardware experiments were satisfied with (5.3), which indicates every linear combination of the fundamental and switching frequencies are feasible harmonic frequencies. The dithered SPWMs mitigated fundamental-

frequency harmonics and the carrier frequency randomization SPWMs reduced harmonic tones associated with the carrier frequencies in both simulation and experimental results. Noise shaping and harmonic mitigating properties of dithered $\Sigma\Delta M$ were also validated by the hardware experiment.

Over the frequency range from 0 Hz to 100 Hz, interharmonics associated with the fundamental frequency of supply power and the PWM harmonic frequencies were investigated. Only dithered SPWM and $\Sigma\Delta M$, which reduced low-order harmonics of PWM, demonstrated mitigated interharmonics in the observed frequency range. These observations are coincident with the confirmed relationship between mitigated harmonics and interharmonics in Chapter 3.

Chapter 6

Conclusion

This dissertation describes dithered PWM methods to mitigate harmonic and interharmonic distortions produced by electric power converters. The fundamental purpose of the dithered PWM is to reduce harmonic generations of the inverter by randomizing switching events of gating signals. The output voltage of a PWM inverter reflects corresponding gating signals as long as the pulse width is longer than the minimum response time of the inverter. Hence, the dithered gating signals induce mitigated harmonics in the output voltage of the inverter. In this dissertation, the effects of proposed dithering methodologies were evaluated on voltage harmonics of PWM inverters and associated current interharmonics at the source side of a VSI-ASD.

In Chapter 2, we described principles of harmonic and interharmonic distortions produced by general AC-DC-AC power converters. Harmonic frequencies produced by the most popular converter topologies, a six-pulse rectifier/inverter and a PWM inverter, were numerically expressed. Using these expressions of harmonic frequencies, we derived interharmonic frequencies at the source-, DC-, and load-sides of two topologies of ASDs, an LCI-ASD and a VSI-ASD. The numerically derived harmonic and interharmonic frequencies were referred to the other chapters to provide feasible frequencies of harmonics and interharmonics generated by simulation models or experiments.

In Chapter 3, we proposed the dithered SPWM configuration to mit-

igate both harmonics at the load side and interharmonics at the source-side of the simulated VSI-ASD model. We empirically evaluated the effects of the dithered SPWM by applying various intensities of the dither. When the dithering was applied to SPWM inverter, the harmonics associated with SPWM were reduced at the load side of the ASD. However, the higher noise floor was observed as the intensity of the dithering was increased. When the standard deviation of the dither was 40% of the rms value of the SPWM reference signal, harmonics were disappeared into noise floor. Likewise the load-side harmonics, the dithered SPWM also mitigated interharmonics at the source side of the ASD at the cost of an increased noise floor. The frequencies of these interharmonics could be interpreted as linear combinations of the source-side fundamental/harmonic frequencies and harmonic frequencies associated with the SPWM. The interpreted linear combinations in interharmonic frequencies were confirmed via cross bicoherence analysis which assesses the nonlinear relationship between two frequency components. Consequently, mitigation of harmonics by means of the dithered SPWM induces decreased interharmonics associated with the PWM harmonics while the noise floor increases. Thus, an optimized level of dithering can be provided for specific limitations for harmonics/interharmonics and noise level.

In Chapter 4, we only focused on the mitigation of PWM harmonics at the load side of an inverter because the nonlinear relationship between mitigated harmonics and interharmonics was assessed in Chapter 3. As an alternative dithering method, we proposed the use of dithered $\Sigma\Delta M$. The desired noise-shaping property of $\Sigma\Delta M$, which suppresses noise density at lower frequencies, was repeated at every sampling frequency of $\Sigma\Delta M$ by zero-order interpolation. It resulted in the mitigated harmonics in low and high frequency

regions. The harmonic-mitigating performance of the dithered $\Sigma\Delta$M was evaluated by comparisons with those of conventional SPWM, dithered SPWM, carrier frequency randomized SPWM, and dithered carrier frequency randomized SPWM. Over a wide range of frequency, the dithered $\Sigma\Delta$M bounded harmonic distortions below -30dB without such prominent tones as carrier frequency and harmonics of SPWM. Furthermore, the number of switching events was not increased from that of conventional SPWM. Thus, the dithered $\Sigma\Delta$M can adequately be used as harmonic mitigation method of PWM inverter.

In Chapter 5, we validated the effects of dithered PWMs in mitigating harmonics and interharmonics by performing hardware experiments. In the experimental description, hardware configurations of the actual three-phase inverter and the scale-down version of VSI-ASD were explained with implemental procedure of PWM gating signals. In the analysis of the experimental result, the harmonic characteristics of conventional SPWM were validated for the feasible harmonic frequencies. Compared with the conventional SPWM harmonics, spectral characteristics of dithered SPWM, carrier frequency SPWM, and the dithered $\Sigma\Delta$M were assessed, which demonstrated coincident properties in mitigating harmonics described in Chapter 4. Proposed dithering methods also mitigated interharmonics at the source side of the VSI-ASD where the interharmonic frequencies are associated with the frequencies of mitigated PWM harmonics. The analysis on the mitigated interharmonics provided the coincident relationship between mitigated harmonics and interharmonics, which is described in Chapter 3.

In this dissertation, the dithering methods on PWM inverters and their effects in mitigating harmonics and interharmonics were discussed. Every power electronic device based on switching operation has inherent nonlinearity

and inevitably produces harmonic distortions. Although L-C harmonic filters mitigate harmonics and interharmonics, limitations still exist such as a moderate slope of transition band, pass-band range, and the limited order. Dithering methods are based on the randomized switching events, which spread out harmonic tones over a wide range of frequency. In addition, dithering methods are implemented in the signal stage, which can save additional cost of hardware in mitigating harmonics and interharmonics.

The dithering methods also have limitations such as increased noise floor, increased number of switching events in dithered SPWM, and increased intermediate harmonics in dithered $\Sigma\Delta$M. In the case of dithered SPWM, excessive intensity of the dithering can reduce the minimum switching period below the response time of the switching device. However, the dithering methods can mitigate harmonics and interharmonics which cannot be totally mitigated by harmonic filters. Thus, the proposed dithering methods can be more valuable when combined with harmonic filters.

As potential future works related with the dithering method, we offer the following comments.

- The effects of the dithered SPWM in mitigating harmonics and interharmonics were empirically assessed by applying various intensities of dithering. To further refine the evaluation of dithering, numerical analysis for the dithered SPWM is needed. With numerical analysis, the optimal intensity of the dithering can be defined.

- The dithered SPWM randomized the switching edges of the PWM gating signals. Because the zero-mean Gaussian noise was excited as dither, the sinusoidal reference signal and the carrier waveform were synchronized

in average. However, each period of sinusoidal signal may not integer multiples of the period of the carrier signal even if the difference is small. This unsynchronized period can cause spectral leakage which increase the noise floor. Thus, the dither needs to be injected at fixed frequency which does not disturb the synchronous conversion.

- In the experiment to validate the effect of dithering on interharmonics, the frequency range of investigation was limited below the second order harmonic of the source-side fundamental frequency due to unbalanced three-phase source. To investigate interharmonics associated with the carrier frequency harmonics, the three-phase source should be refined.

Appendices

Appendix A

Detection of Time-Varying Waveform Distortion in a Variable Speed Wind Power Converting System

In this appendix, we provide an example of harmonic distortions by investigating the grid power quality of a variable speed wind turbine (VSWT) system. To analyze voltage and current spectra with respect to wind penetration time, we use a joint time-frequency analysis. The VSWT is composed of a mechanical part and an AC-DC-AC converter, thus the contents associated with electric power distortion provide an evidence of harmonics in AC-DC-AC converter. Through simulation experiments based on PSCAD/EMTDC program, frequency-varying characteristics of the currents are demonstrated and compared with the wind speed. The fundamental idea of this appdendix is frequency analysis, with respect to time, at the power grid side to monitor harmonics and additional extraneous non-harmonic frequencies which appear when the wind speed drops below a certain critical value. As a result of the appearance of the extraneous frequencies, power quality at the grid side can further degrade. Thus, we also provide another guideline for cut-in wind speed to avoid power quality degradation.

A.1 Introduction

Wind energy has been recognized as one of abundant renewable energy sources. As a result, wind turbines have evolved over the past few decades. Among the many wind turbine concepts, a three-bladed horizontal-axis structure has turned out to be the most efficient model [44], and fixed-speed wind turbines, which are a combination of the horizontal axis blade and an induction generator, have been widely used due to the ease of connection to the power grid. On the other hand, variable speed wind turbines (VSWTs) based on synchronous generators have been adopted as a topology by the major manufacturers [45]. This topology yields up to 30 percent more energy than fixed speed operation, and it reduces power fluctuations and reactive power supplied to the grid [2]. Furthermore, the decreasing price of power electronic devices is favorable to the development of VSWTs. Modeling of VSWTs has been focused on power for the operational range between cut-in and cut-off wind speed. The cut-in and cut-off wind speeds are determined by power efficiency and mechanical safety, respectively. Although power quality issues and other effects in VSWTs have been considered [46, 47], they mainly focus on frequency analysis which can be acquired from conventional Fourier transform analysis over a specific time duration. Since the Fourier frequency response during a measured time period depends on the "average" of the wind speed, even if the wind speed is lower than the rated wind speed part of the time, a time-localized frequency response is difficult to determine using conventional Fourier-transform spectral analysis. Therefore, we utilize a joint time-frequency analysis method in this appendix to provide time-localized spectral information for the current produced by a VSWT system. The remainder of this appendix is organized as follows. The time-frequency theories are reviewed in Section A.2. Section A.3

demonstrates the simulation environments and the results. The conclusion is presented in Section A.4.

A.2   Time-Frequency Analysis: Cohen's Class

Time-frequency analysis was initiated by time-localization for Fourier analysis, which is called the short-time Fourier transform (STFT), or spectrogram [48]. Since the STFT does not guarantee the desirable properties of the time-frequency distribution such as the time and frequency marginal properties, the finite support property, and the uncertainty principle [49], the joint time-frequency distribution was proposed. The first proposal of a joint time-frequency distribution is the Wigner-Ville distribution [1], which is based on an instantaneous auto-correlation and a characteristic function. The definition of the Wigner-Ville distribution is as follows [1]:

$$WV(t, \omega) = \frac{1}{2\pi} \int s^*(u - \frac{\tau}{2})s(u + \frac{\tau}{2})e^{-j\tau\omega}d\tau \qquad (A.1)$$

where $s(t)$ is the analytic signal representation of the experimentally observed real signal and is assumed to be normalized to unit energy.

Cohen's class is a generalized joint time-frequency distribution based on the Wigner-Ville distribution and is characterized by an auxiliary function called the kernel function. The definition of Cohen's class is as follows [1]:

$$C(t, \omega) = \frac{1}{4\pi^2} \iiint s^*(u - \frac{\tau}{2})s(u + \frac{\tau}{2})\phi(\theta, \tau)e^{-j\theta t - j\tau\omega + j\theta u}dud\tau d\theta \qquad (A.2)$$

where $\phi(\theta, \tau)$ is a two dimensional function called the kernel. $s(t)$ is the analytic signal representation of the experimentally observed real signal. Fur-

Table A.1: Properties of time frequency distributions and corresponding kernel requirements [1]

Properties of time frequency distributions	Requirements of kernel
Time marginal $$\int C(t,\omega)d\omega = |s(t)|^2$$	$\phi(\theta, 0) = 1$
Frequency marginal $$\int C(t,\omega)d\omega = |S(\omega)|^2$$	$\phi(0, \tau) = 1$
Total energy $$\iint C(t,\omega)d\omega dt = 1$$	$\phi(0, 0) = 1$
Realness $$C(t,\omega) \in \mathbf{R}$$	$\phi(\theta, \tau) = \phi^*(-\theta, -\tau)$
Time shift $$y(t) = x(t - t_0) \rightarrow C_y(t,\omega) = C_y(t - t_0, \omega)$$	$\phi(\theta, \tau)$ is independent of τ
Frequency modulation $$y(t) = x(t)e^{j\omega_0 t} \rightarrow C_y(t,\omega) = C_y(t, \omega - \omega_0)$$	$\phi(\theta, \tau)$ is independent of θ
Scaling invariance $$y(t) = \sqrt{a}x(at) \rightarrow C_y(t,\omega) = C_x(at, \omega/a)$$	$\phi(\theta, \tau) = \phi(\theta\tau)$
Cross term minimization	$\phi(\theta, \tau) << 1$ for $\theta\tau >> 0$

thermore, $s(t)$ is assumed to be normalized to unit energy. The Wigner-Ville distribution corresponds to (A.2) with $\phi(\theta, \tau) = 1$. The desirable properties of the time-frequency distribution such as marginals, total energy, realness, time shift, frequency modulation, scaling invariance, and cross term minimization are closely connected to the kernel function. Table A.1 summarizes the kernel requirements for the desirable properties of the distributions [1].

Among the kernel-based time-frequency distributions, the Choi-Williams distribution [50] was suggested to reduce interference effects in distribution.

The definition of the Choi-Williams distribution is as follows:

$$CW(t, \omega) = \frac{1}{4\pi^{3/2}} \iint \frac{1}{\sqrt{\tau^2/\sigma}} e^{-\frac{(u-t)^2}{4\tau^2/\sigma} - j\tau\omega} s^*(u - \frac{\tau}{2}) s(u + \frac{\tau}{2}) e^{-j\tau\omega} du d\tau$$

(A.3)

The corresponding kernel is

$$\phi(\theta, \tau) = e^{-\theta^2 \tau^2 / \sigma}$$

(A.4)

where $\sigma(\sigma > 0)$ is a scaling factor, which controls the strength of the cross term suppression discussed in the next paragraph. The Choi-Williams kernel in (A.4) follows the desirable properties in Table A.1: (i) time and frequency marginal properties, (ii) normalized total energy, (iii) realness of distribution, (iv) scaling invariance, and (v) cross term minimization with scaling factor.

The joint time frequency distribution density, $C(t, \omega)$, depends on the product of $s(\cdot)$ and $s^*(\cdot)$. Hence, for multi-component signal, there will be cross product terms in the joint time frequency distribution density. In the case where the signal has multiple frequency components, such as an electrical signal generated from wind power system, the cross term minimization property in Table A.1 enables one to suppress the interference distributions. Among the well known kernels, the Choi-Williams kernel is utilized in section A.3 due to the strong property of cross term minimization, where the scaling factor, σ, is empirically determined to be 0.5.

A.3   Simulation Experiment

As an example of a time-invariant nonlinear system with a time-varying non-stationary excitation, we simulated a VSWT system in PSCAD, and an-
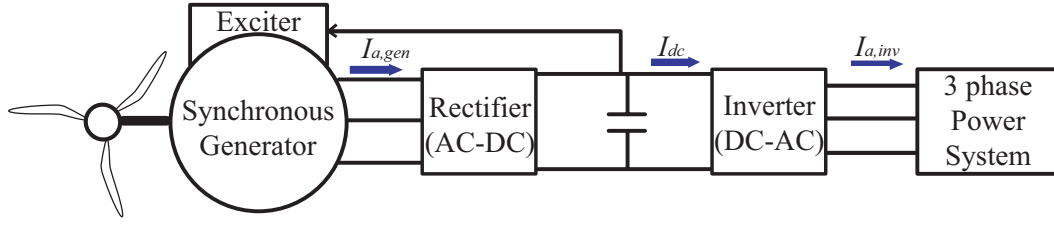
Figure A.1: Simulation experiment configuration of the VWST implemented using PSCAD

Table A.2: Synchronous generator ratings [2]

Power	1.0 MVA
Voltage	1.1 kV
Current	0.32 KA
Frequency	18.77 Hz
Number of pole	84

Table A.3: Parameters for wind turbine [2]

Power rating	1.0 MW
Blade radius	32 m
Air density	0.55 kg/m^3
Rated wind speed	12.5 m/s
Cut-in wind speed	5 m/s
Cut-off wind speed	25 m/s
Blade pitch angle	0°

alyzed the system using MATLAB-based programs. In the model, a multipolar synchronous generator is directly connected to the wind turbine without a gearbox and a fixed pitch angle of 0° is applied to the blade configuration, which is the applied concept of VSWTs by one of the world's leading manufacturers [45]. Fig. A.1 illustrates the configuration of the simulated system and Table A.2 and A.3 summarize the wind turbine parameters and synchronous generator ratings, respectively [2].

The system can be divided into 3 parts with respect to the operational frequency: a) generator side whose electrical frequency is rated at 18.77 Hz, b) DC link side with a capacitor, and c) a power grid part whose electrical frequency is rated at 60 Hz. A 6-pulse rectifier is located between parts a) and b), and a pulse width modulation (PWM) inverter between parts b) and c). In this configuration, a time-varying wind speed produces frequency-varying AC power at the generator output, which is converted into DC power and the DC power is subsequently converted into 60 Hz to supply AC power to the grid. A 6-pulse rectifier is modeled to convert AC power into DC, and a voltage source pulse width modulation (PWM) inverter is modeled to convert DC into AC again. To control the reactive power supplied to the grid, constant power factor and voltage regulation have been implemented [2]. Assuming a balanced three phase system, we carry out a time-frequency analysis of the currents, $I_{a,inv}$, I_{dc}, and $I_{a,gen}$, which are indicated in Fig. A.1.

One of the major considerations in wind turbine modeling is power efficiency, and the system is designed to produce maximum mechanical power described in (A.5).

$$P_M = 0.5 \rho \pi R^5 C_P \frac{\omega_M^3}{\lambda^3} \tag{A.5}$$

where

λ: tip speed ratio defined by (A.6)

ω_M: blade angular speed [rad/s]

R: blade radius [m]

V_{WIND}: wind speed [m]

P_M: mechanical power [kW]

ρ: air density [kg/m^3]

C_P: power coefficient expressed as (A.7) [51].

$$\lambda = \frac{\omega_M R}{V_{WIND}} \tag{A.6}$$

$$C_P = (0.44 - 0.0167\beta)\sin\frac{\pi(\lambda - 2)}{13 - 0.3\beta} - 0.00184(\lambda - 2)\beta \tag{A.7}$$

where β is the blade pitch angle. Since the available mechanical power depends on the tip speed ratio, the maximum power for given wind speed can be achieved at optimal tip speed ratio by adjusting the mechanical angular velocity as shown in Fig. A.2, and can be maximally converted into electric power by inverter control techniques. By applying the achievable maximum power and zero value of reactive power as the reference powers to the inverter firing control, the inverter output power traces the maximum power with constant power factor [2].

A four-component wind model [52] is selected for the simulation, which is described by

$$V_{WIND} = V_{BASE} + V_{GUST} + V_{RAMP} + V_{NOISE} \tag{A.8}$$

where $V_{BASE}, V_{GUST}, V_{RAMP}$, and V_{NOISE} are modeled by constant, sinusoidal, ramp, and triangle wave functions, respectively [2]. Fig. A.3 illustrates the modeled wind speed. The currents $I_{a,inv}$, I_{dc}, and $I_{a,gen}$ are analyzed by using the Choi-Williams distribution for levels below and above the rated wind speed as shown by the dashed lines (1) and (2) in Fig. A.3, respectively.

We initiated our study with a generator-side and DC link harmonic frequency analysis. As described in (2.2) and (2.4) in Chapter 2, the 6-pulse
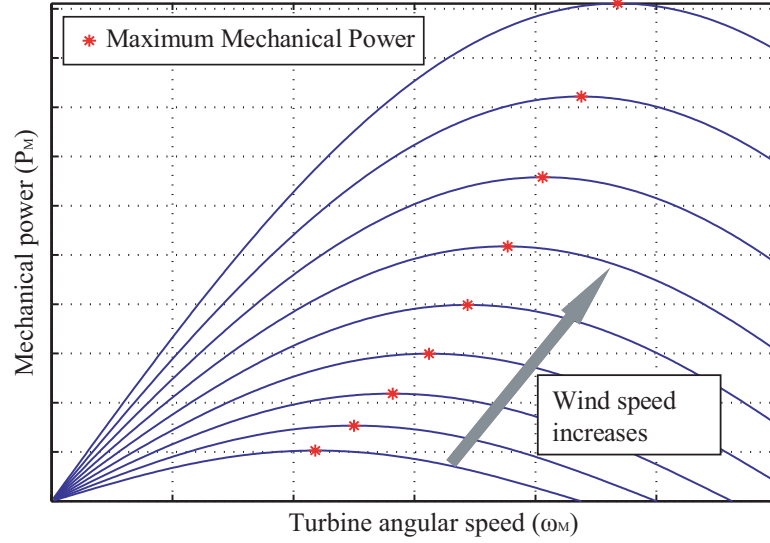
Figure A.2: Mechanical power with respect to turbine angular velocity
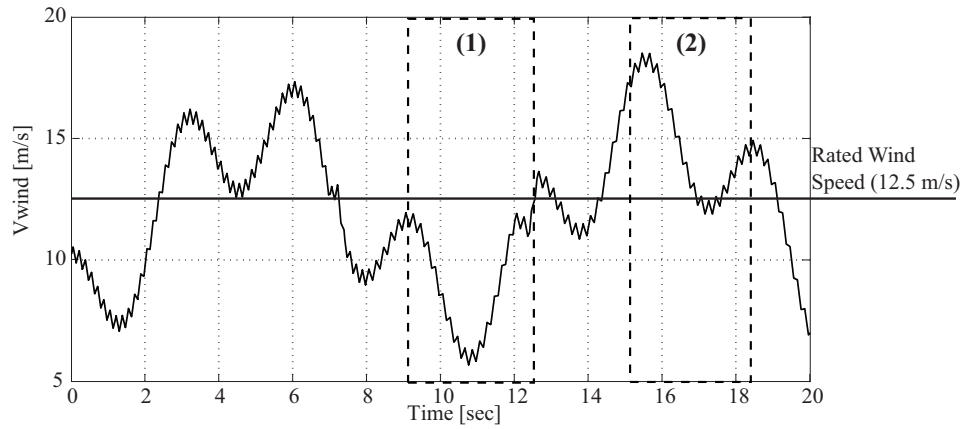

Figure A.3: Wind speed vs. time. Case (1) wind speed below rated value, 12.5 m/s, Case (2) wind speed above rated value

rectifier converts AC to DC, transmitting $(6n)th$ harmonics to the DC link and reflecting $(6n\pm1)th$ harmonics to the generator side, where $n = 1, 2, ...$ In the case where the AC frequency at the generator side varies in time, the harmonic variations are multiplied by the order of harmonics. Fig. A.4(a), (b) and (c) represent the time-frequency distribution of the current at the generator-side, at the DC link, and corresponding wind speed, respectively, where the wind speed is above the rated wind speed of 12.5 m/s.

The energy spectral density and the time-frequency distribution are plotted in dB full scale (dBFS) in which the density at the fundamental frequency is represented as 0 dB. In Fig. A.4(a) and (b), the threshold of -30 dB is the truncation level for clear plotting, and a sigma of 0.5 is the parameter of the Choi-Williams distribution. The thin vertical lines which appear in the time-frequency distribution are artifacts associated with the window function used to plot the frequency response clearly, and do not represent physical phenomena of interest. Energy spectral densities which are located at the left side of the time-frequency distribution plots in Fig. A.4(a) and (b) are accumulations of each instantaneous spectral density during the time span shown (15 s∼18.5 s). In Fig. A.4(a), the time-frequency distribution of the generator current demonstrates instantaneous fundamental, 5th, and 7th harmonic frequency characteristics indicating the generator and the rectifier are in normal operating condition. However, the instantaneous frequencies of the 5th and 7th harmonics are shown as the broader bandwidth in the energy spectral density plot located at the left side of Fig. A.4(a), which makes it difficult to interpret the exact location of the harmonic frequencies and to determine whether the system is operating in a normal condition. In Fig. A.4(b), the dominant harmonic terms at the DC link side when the wind speed is above
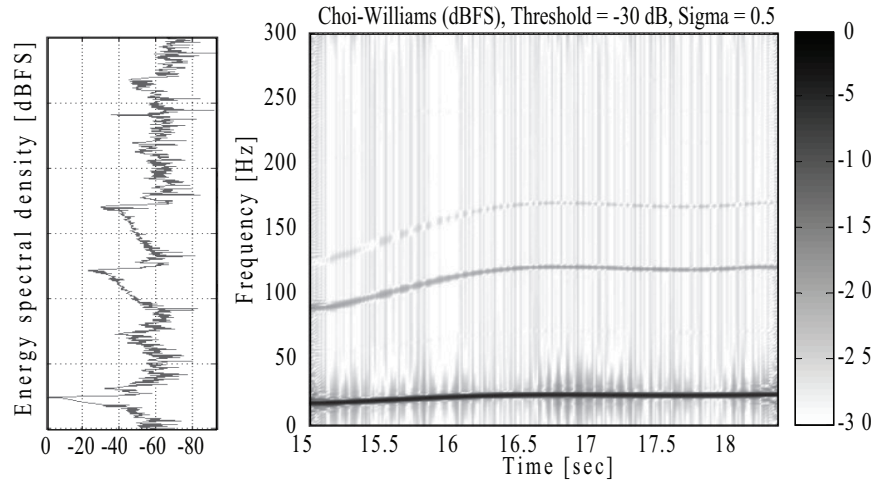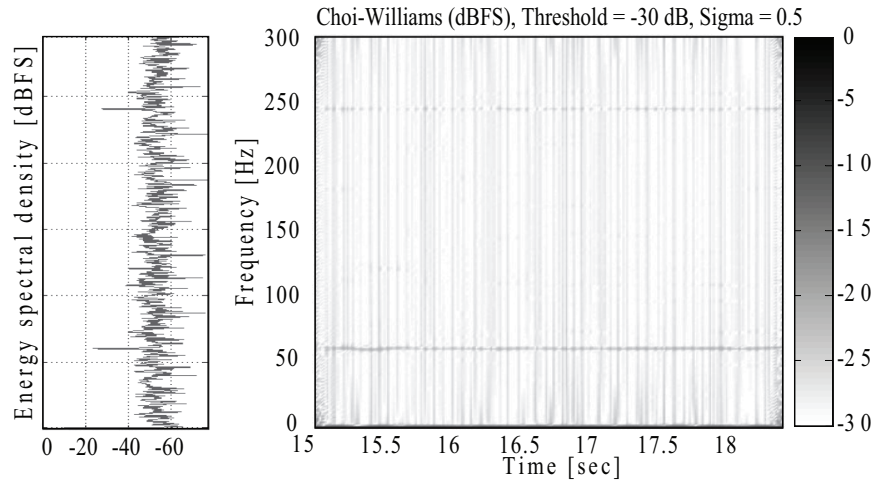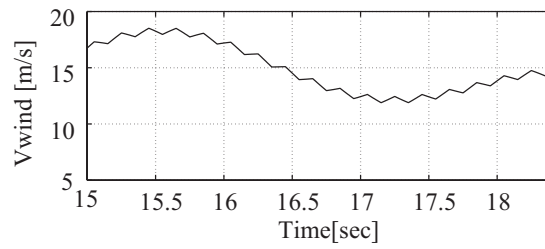
Figure A.4: Time-frequency distribution of the current (a) at the generator side and (b) at the DC link for the wind speed above the rated value. (c) corresponding wind speed.

the rated wind speed are 60 Hz and 240 Hz, which are the fundamental and 4th harmonic of 60 Hz. The switching frequency of the PWM inverter is 600 Hz, and the modulation ratio is 10, where the modulation ratio is defined by the ratio of switching frequency to the reference frequency, the latter of which is identical to the 60 Hz inverter output frequency. For non-triple and even number of modulation ratios, every integer multiple of the inverter fundamental frequency of 60 Hz may appear in the DC link [21].

Figs. A.5(a), (b) and (c) represent the time-frequency distribution of the current at the generator-side, at the DC link, and corresponding wind speed, respectively, where the wind speed is below the rated wind speed of 12.5 m/s. The threshold level and the value of sigma are same as those in Fig. A.5(a) and (b). In Fig. A.5(a), the fundamental, the 5th, and the 7th harmonic frequencies of the generator current decrease after approximately 1.2 s system latency as the wind speed declines. In the time period between 9 s and 12.5 s, the 5th and the 7th harmonics are overlapped in the energy spectral density plot located at the left side in Fig. A.5(a) and appear as broad-band energy spectral density between 75 Hz and 140 HZ, approximately. Those harmonics, however, clearly appear at the expected locations, which are 5 and 7 times the fundamental frequency, in the joint time-frequency distribution plot of Fig. A.5(a). At the DC link as shown in Fig. A.5(b), DC, 60 Hz, and 240 Hz frequencies appear until approximately 10.8 s, and an extraneous frequency component of the current appears near 30 Hz from approximately 11 s onward. During this period, the fundamental and the harmonic frequencies of the generator current have their lowest values as shown in Fig. A.5(a), which corresponds to the lowest wind speed in this simulation. The observation that DC current has extraneous frequency components during this period serves as

evidence of the wind speed effects on the DC link and possibly on the power grid.

Fig. A.6(a) and (b) represent the energy spectral density and time-frequency distribution of the current at the power grid side of the VSWT where the wind speed is above the rated speed. When the wind speed is above the rated wind speed, most of the energy is distributed at the 60 Hz fundamental frequency and the harmonic frequencies of 120 Hz and 240 Hz as indicated in Fig. A.6(a).

Meanwhile, when the wind speed drops to slightly above the cut-in value, 5 m/s, extraneous frequencies appear as shown in Fig. A.7(a). Comparing Fig. A.6(a) and Fig. A.7(a), we note that the extraneous frequencies appear to be abnormal components. The time-frequency distribution in Fig. A.7(a) illustrates how the spectral densities change with time and when the abnormality exists. From 9.0 s to 10.8 s, the grid current has a strong fundamental frequency at 60 Hz and a small amount of 2nd and 4th harmonics at 120 Hz and 240 Hz, which are expected as normal frequency components of a PWM inverter. However, above 10.8 s, extraneous frequencies of approximately 90 Hz, 30 Hz, and 10 Hz appear, which may potentially degrade the quality of power supplied to the grid. The appearance of the extraneous frequencies at the grid side is coincident with the onset of the approximately 30 Hz frequency term at DC link (see Fig. A.5(b)) and also corresponding the lowest wind speed. Energy spectral densities which is displayed at left side of joint-time frequency graphs show time-accumulation of frequency responses. Thus, the extraneous frequency components inaccurately appear in the energy spectral density, since they temporally exist.

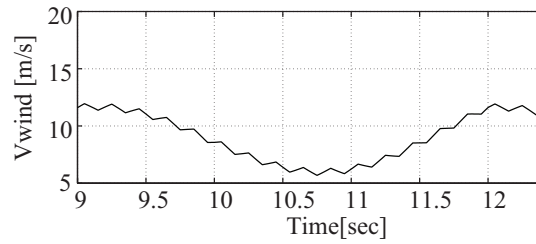The joint-time frequency distribution of the fundamental current at the
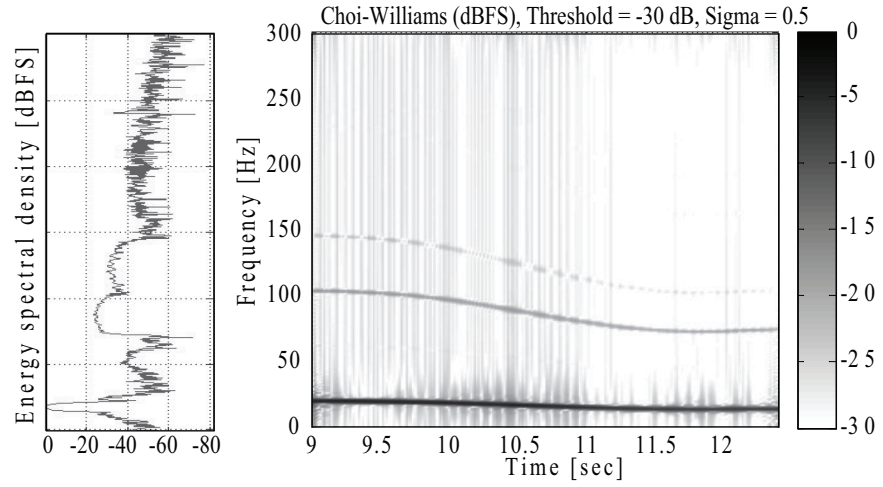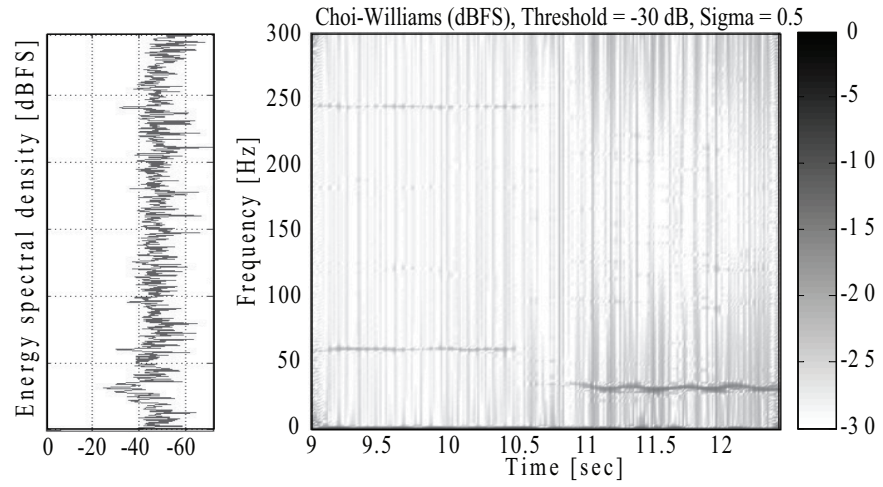
Figure A.5: Time-frequency distribution of the current (a) at the generator-side and (b) at the DC link for the wind speed below the rated value. (c) corresponding wind speed.

111

Figure A.6: Time-frequency distribution at power grid for the wind speed above rated value. (a) time-frequency distribution (b) corresponding wind speed.

grid side is illustrated in Fig. A.8. As the wind speed decreases close to the cut-in speed, the amplitude varies in a way similar to the wind speed. By comparing the variation of the fundamental current with wind speed, the system latency can be inferred. Since the lowest wind speed and the fundamental amplitude appear at approximately 10.8 s and 11.8 s, respectively, the system latency of the VSWT model is about 1.0 s. Thus, the extraneous frequency near 90 Hz which appears 10.8 s onward in Fig. A.6(a) may be affected by an
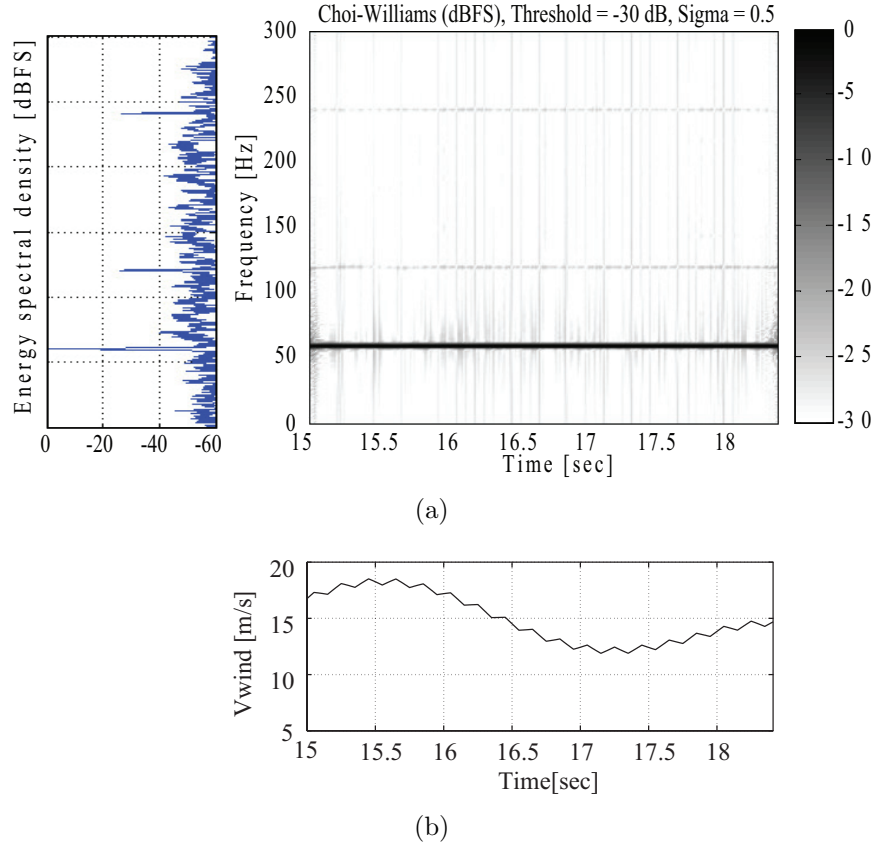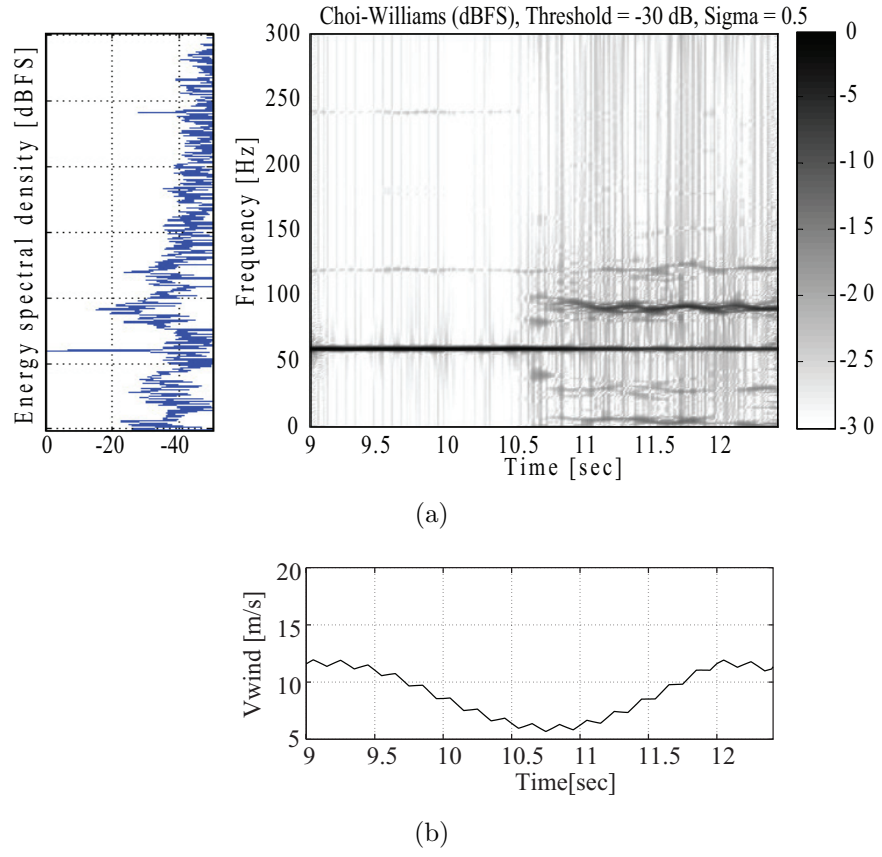
Figure A.7: Time-frequency distribution at power grid for the wind speed below the rated value. (a) time-frequency distribution (b) corresponding wind speed.

onset wind speed at 9.8 s. The corresponding wind speed at 9.8 s is about 9.5 m/s, which may have affected the onset of the extraneous frequencies at the grid connection.
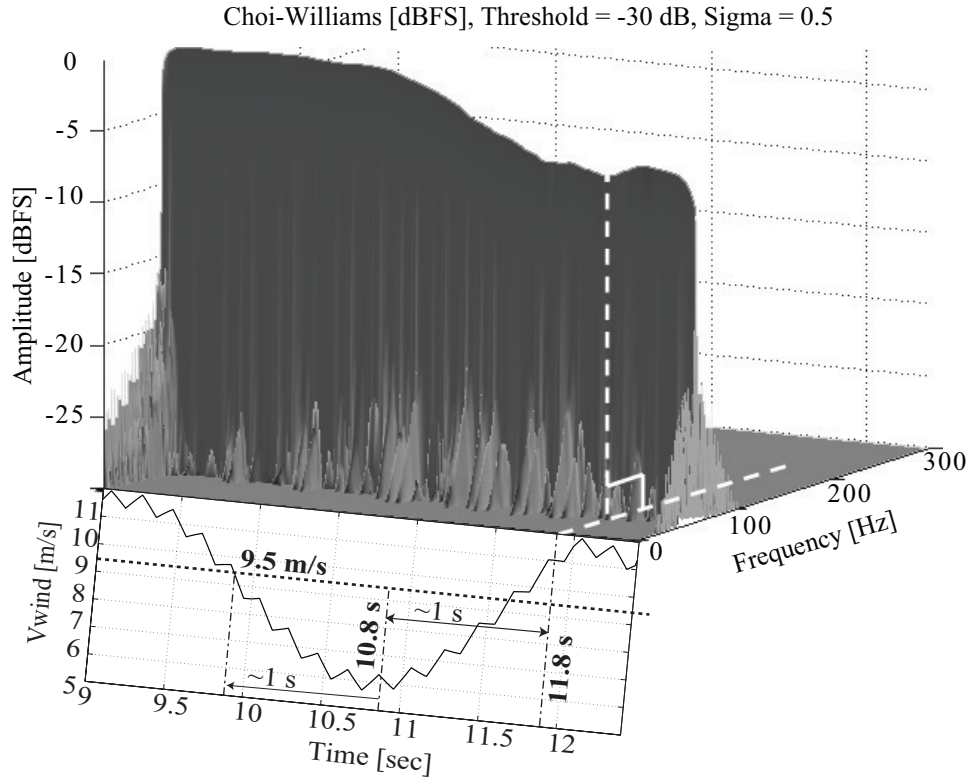
Figure A.8: Fundamental frequency distortion of the grid side current and corresponding wind speed

A.4 Conclusion

We demonstrated investigation methods for the power quality issues associated with VSWTs using the joint time-frequency distribution. As a first step of this proposal, we implemented a PSCAD model of VSWT and measured the currents at the generator side, the DC link, and the power grid connection. Utilizing MATLAB implementation of the joint time-frequency distribution, we investigated the effect of the time-varying wind speed on the frequency characteristics of each measured current at the generator, DC-link, and grid side. From the result, we observed that extraneous frequencies at 10

Hz, 30 Hz, and 90 Hz appear on the power grid side when wind speed drops to a little above the cut-in value.

Bibliography

[1] L. Cohen, *Time-Frequency Analysis.* Prentice Hall, 1995.

[2] S.-K. Kim and E.-S. Kim, "PSCAD/EMTDC-based modeling and analysis of a gearless variable speed wind turbine," *Energy Conversion, IEEE Transactions on*, vol. 22, no. 2, pp. 421–430, Jun. 2007.

[3] http://www.fairchildsemi.com/an/AN/AN-9044.pdf.

[4] "IEEE recommended practice for monitoring electric power quality," *IEEE Std 1159-1995*, 1995.

[5] E. Owen, "A history of harmonics in power systems," *Industry Applications Magazine, IEEE*, vol. 4, no. 1, pp. 6 –12, Jan. 1998.

[6] "General guide on harmonics and interharmonics measurements," *IEC 61000-4-7*, 2000.

[7] http://www.leonardo-energy.org/webfm_send/215.

[8] R. Yacamini, "Power system harmonics. iv. interharmonics," *Power Engineering Journal [see also Power Engineer]*, vol. 10, no. 4, pp. 185–193, Aug. 1996.

[9] E. W. Gunther, "Interharmonics in power systems," in *Proceedings of IEEE Power Engineering Society Summer Meeting 2001*, vol. 2, Jul. 2001, pp. 813–817.

[10] D. Galo, R. Langella, and A. Testa, "On the processing of harmonics and interharmonics in electrical power systems," in *Proceedings of IEEE Power Engineering Society Winter Meeting 2000*, vol. 3, Jan. 2000, pp. 1581–1586.

[11] A. Testa and R. Langella, "Power system subharmonics," in *IEEE Power Engineering Society General Meeting*, Jun. 2005, pp. 1922–1927.

[12] http://www.leonardo-energy.org/webfm_send/115.

[13] D. Ismail, H. Syafruddin, A. Rosnazri, M. Samila, and A. Haziah, "The effects of harmonic components on transformer losses of sinusoidal source supplying non-linear loads," *American Journal of Applied Sciences*, vol. 3, no. 12, pp. 2131–2133, 2006.

[14] I. Group, "Iv, b. power line harmonic effects on communicaiton line interference," *Power Apparatus and Systems, IEEE Transactions on*, vol. PAS-104, no. 9, pp. 2578 –2587, Sep. 1985.

[15] V. Wagner, J. Balda, D. Griffith, A. McEachern, T. Barnes, D. Hartmann, D. Phileggi, A. Emannuel, W. Horton, W. Reid, R. Ferraro, and W. Jewell, "Effects of harmonics on equipment," *Power Delivery, IEEE Transactions on*, vol. 8, no. 2, pp. 672 –680, Apr. 1993.

[16] D. Gallo, C. Landi, R. Langella, and A. Testa, "IEC flickermeter response to interharmonic pollution," Sep. 2004, pp. 489 – 494.

[17] M. Hernes and B. Gustavsen, "Simulation of shaft vibrations due to interaction betwen turbine-generator train and power electronic converters at the visund oil platform," in *Proceedings of Power Conversion Conference*, vol. 3, Osaka, Japan, Apr. 2002, pp. 1381–1386.

[18] C. Bowler, "Proposed steaty-state limits for turbine-generator torsional response," in *invited paper at IEEE Summer Power Meeting 2002*, Jul. 2002.

[19] D. Gallo, R. Langella, A. Testa, and A. Emanuel, "On the effects of voltage subharmonics on power transformers: a preliminary study," Sep. 2004, pp. 501 – 506.

[20] J. de Abreu and A. Emanuel, "Induction motor thermal aging caused by voltage distortion and imbalance: loss of useful life and its estimated cost," *Industry Applications, IEEE Transactions on*, vol. 38, no. 1, pp. 12 –20, Jan./Feb. 2002.

[21] F. de Rosa, R. Langella, A. Sollazzo, and A. Testa, "On the interharmonic components generated by adjustable speed drives," *Power Delivery, IEEE Transactions on*, vol. 20, no. 4, pp. 2535–2543, Oct. 2005.

[22] L. Manz, "Applying adjustable-speed drives to three-phase induction NEMA frame motors," *Industry Applications, IEEE Transactions on*, vol. 33, no. 2, pp. 402–407, Mar./Apr. 1997.

[23] J. Zubek, A. Abbondanti, and C. J. Norby, "Pulsewidth modulated inverter motor drives with improved modulation," *Industry Applications, IEEE Transactions on*, vol. IA-11, no. 6, pp. 695–703, Nov. 1975.

[24] R. C. Dugan, M. F. McGranaghan, S. Santoso, and H. W. Beaty, *Electrical Power Systems Quality*. McGraw-Hill, 2002.

[25] Y. Cao, Y. Yang, and T. Xu, "A new method for interharmonic detection based on harmonic filtration," vol. 1, Dec. 2009, pp. 447 –450.

[26] T. Zhu, "Exact harmonics/interharmonics calculation using adaptive window width," *Power Delivery, IEEE Transactions on*, vol. 22, no. 4, pp. 2279 –2288, Oct. 2007.

[27] Z. Li, L. Kaipei, M. Bingwei, and T. Qian, "Interharmonic detection based on support vector machine," in *Industrial Electronics and Applications, 2006 1ST IEEE Conference on*, 24-26 2006, pp. 1 –4.

[28] T. Kim, W. Cho, E. Powers, W. Grady, and A. Arapostathis, "ASD system condition monitoring using cross bicoherence," in *Electric Ship Technologies Symposium, 2007. ESTS '07. IEEE* May 2007, pp. 378 –383.

[29] K. S. Lii and K. N. Helland, "Cross-bispectrum computation and variance estimation," *ACM Trans. Math. Softw.*, vol. 7, no. 3, pp. 284–294, 1981.

[30] J. Chen and T. Liang, "A novel algorithm in solving nonlinear equations for programmed PWM inverter to eliminate harmonics," in *Industrial Electronics, Control and Instrumentation, 1997. IECON 97. 23rd International Conference on*, vol. 2, Nov. 1997, pp. 698–703 vol.2.

[31] R. Villarreal-Ortiz, M. Hernandez-Angeles, C. Fuerte-Esquivel, and R. Villanueva-Chavez, "Centroid PWM technique for inverter harmonics elimination," *Power Delivery, IEEE Transactions on*, vol. 20, no. 2, pp. 1209–1210, Apr. 2005.

[32] Y.-S. Lai and S. Bowes, "A novel harmonic elimination pulse-width modulation technique for static converter and drives," in *Applied Power Electronics Conference and Exposition, 1998. APEC '98. Conference Proceedings 1998., Thirteenth Annual*, vol. 1, Feb. 1998, pp. 108–115 vol.1.

[33] T.-J. Liang, R. O'Connell, and R. Hoft, "Inverter harmonic reduction using Walsh function harmonic elimination method," *Power Electronics, IEEE Transactions on*, vol. 12, no. 6, pp. 971–982, Nov. 1997.

[34] S. Bowes and S. Grewal, "Novel harmonic elimination PWM control strategies for three-phase PWM inverters using space vector techniques," *Electric Power Applications, IEE Proceedings -*, vol. 146, no. 5, pp. 495–514, Sep. 1999.

[35] D. M. Brod and D. W. Novotny, "Current control of VSI-PWM inverters," *Industry Applications, IEEE Transactions on*, vol. IA-21, no. 3, pp. 562–570, May 1985.

[36] T. Habetler and D. Divan, "Acoustic noise reduction in sinusoidal PWM drives using a randomly modulated carrier," *Power Electronics, IEEE Transactions on*, vol. 6, no. 3, pp. 356–363, Jul. 1991.

[37] S. Johnson and R. Zane, "Custom spectral shaping for EMI reduction in high-frequency inverters and ballasts," *Power Electronics, IEEE Transactions on*, vol. 20, no. 6, pp. 1499–1505, Nov. 2005.

[38] A. Fardoun, A. Assi, and E. Ismail, "Reduction of EMI through switching frequency dithering," in *50th Midwest Symposium on Circuits and Systems*, Aug. 2007, pp. 538–541.

[39] B. K. Bose, *Power electronics and motor drives*. Academic Press, 2006.

[40] M. Kheraluwala and D. Divan, "Delta modulation strategies for resonant link inverters," *Power Electronics, IEEE Transactions on*, vol. 5, no. 2, pp. 220–228, Apr. 1990.

[41] A. Frazier and M. Kazimierczuk, "DC-AC power inversion using $\Sigma - \Delta$ modulation," *Circuits and Systems I: Fundamental Theory and Applications, IEEE Transactions on*, vol. 47, no. 1, pp. 79–82, Jan. 2000.

[42] P. Aziz, H. Sorensen, and J. Van der Spiegel, "An overview of sigma-delta converters," *Signal Processing Magazine, IEEE*, vol. 13, no. 1, pp. 61–84, Jan. 1996.

[43] R. Yacamini, "Power system harmonics. part 1. harmonic sources," *Power Engineering Journal*, vol. 8, no. 4, pp. 193 –198, Aug. 1994.

[44] J. F. Manwell and J. G. McGowan, *Wind Energy Explained: Theory, Design and Application.* Wiley, 2002.

[45] L. Hansen, P. Madsen, F. Blaabjerg, H. Christensen, U. Lindhard, and K. Eskildsen, "Generators and power electronics technology for wind turbines," *Industrial Electronics Society, 2001. IECON '01. The 27th Annual Conference of the IEEE*, vol. 3, pp. 2000–2005 vol.3, 2001.

[46] S. Tentzerakis, N. Paraskevopoulou, S. Papathanassiou, and P. Papadopoulos, "Measurement of wind farm harmonic emissions," *Power Electronics Specialists Conference, 2008. PESC 2008. IEEE*, pp. 1769–1775, Jun. 2008.

[47] J. Herrera, T. Reddoch, and J. Lawler, "Harmonics generated by two variable speed wind generating systems," *Energy Conversion, IEEE Transactions on*, vol. 3, no. 2, pp. 267–273, Jun. 1988.

[48] L. Cohen, "Time-frequency distributions-a review," *Proceedings of the IEEE*, vol. 77, no. 7, pp. 941–981, Jul. 1989.

[49] W. J. Williams, M. L. Brown, and A. O. Hero III, "Uncertainty, information, and time-frequency distributions," F. T. Luk, Ed., vol. 1566, no. 1. SPIE, 1991, pp. 144–156.

[50] H.-I. Choi and W. Williams, "Improved time-frequency representation of multicomponent signals using exponential kernels," *Acoustics, Speech and Signal Processing, IEEE Transactions on*, vol. 37, no. 6, pp. 862–871, Jun. 1989.

[51] A. Murdoch, J. Winkelman, S. Javid, and R. Barton, "Control design and performance analysis of a 6 mw wind turbine-generator," *Power Apparatus and Systems, IEEE Transactions on*, vol. PAS-102, no. 5, pp. 1340–1347, May 1983.

[52] P. Anderson and A. Bose, "Stability simulation of wind turbine systems," *Power Apparatus and Systems, IEEE transactions on*, vol. PAS-102, no. 12, pp. 3791–3795, Dec. 1983.

Vita

Wonjin Cho was born in Daegu, Korea in 1977 as the son of Chabong Cho and Okhee Chang. After completing his work at Hyubsung High School, Daegu, Korea in 1996, he enrolled in the Department of Electrical and Mechanical Engineering at Yonsei University, Seoul, Korea. From April 1998 to June 2000, he served as a personel administrator in Republic of Korea Army, Goesan, Korea. He earned his Bachelor of Science degree from the Department of Electrical and Electronics Engineering at Yonsei University, Seoul, Korea in March 2003. In August 2003, he entered the Departemnt of Electrical and Computer Engineering at the University of Texas at Austin, and finished his Masters of Science in Engineering in May 2005. He continued pursuing his Ph.D. from the Department of Electrical and Computer Engineering at The University of Texas at Austin, Austin, TX under supervision of Professor Edward J. Powers and Professor Surya Santoso and graduated in December 2010. His primary research interests are power quality improvement of pulsewidth modulated inverters, joint time-frequency signal processing, and higher-order statistical signal processing.

Permanent address: Taewang Yuseong Hivill Apt. Beomeo 1-dong,
                   Suseong-gu, Daegu, Rep of KOREA (706-023)

This dissertation was typeset with LaTeX† by the author.

---

†LaTeX is a document preparation system developed by Leslie Lamport as a special version of Donald Knuth's TeX Program.